Advanced Antenna Miniaturization Techniques for Low-Power, Broadband and Diversity Wireless Systems

by

Jungsuek Oh

A dissertation submitted in partial fulfillment
of the requirements for the degree of
Doctor of Philosophy
(Electrical Engineering)
in The University of Michigan
2012

Doctoral Committee:

Professor Kamal Sarabandi, Chair
Professor Christopher Ruf
Professor Amir Mortazawi
Professor Eric Michielssen

To God
To my father Sehoon and my mother Kwangja
To my wife Hyesook and my lovely son Yeonjun

ACKNOWLEDGEMENTS

First and foremost, I would like to thank and dedicate all my success to God, my parents and parents-in-law. Without their love and care, I would not be able to accomplish this dissertation.

I want to express my sincere gratitude and appreciation to my advisors Prof. Kamal Sarabandi for his warm heart, continuous support, encouragement and guidance throughout my studies. I could not have imagined having a better advisor and mentor for my Ph.D study. I would like to extend my sincere gratitude to my other committee members, Prof. Christopher Ruf, Prof. Amir Mortazawi and Prof. Eric Michielssen for devoting their time to review this thesis and advising me with valuable suggestions.

I am also grateful to Prof. Sangwook Nam at Seoul National University for his support and guidance during my master's program. I was able to have a solid background in applied electromagnetics and microwave engineering at his group.

This list will not be complete without acknowledging my wife Hyesook for her support during the past four years. If at all I am successful in life, it is not sheer luck or my brilliance; it is all my loving wife Hyesook's support and endless love. Presence of my lovely son Yeonjun, who was born in October 2010 and brought a great deal of joy into my life, was also a great motivation for me.

Jungsuek

Summer, 2012,

Ann Arbor.

TABLE OF CONTENTS

LIST OF FIGURES

x

xi

LIST OF TABLES

LIST OF APPENDICES

Appendix

ABSTRACT

Advanced Antenna Miniaturization Techniques for Low-Power, Broadband and Diversity Wireless Systems

by

Jungsuek Oh

Chair: Kamal Sarabandi

Nowadays miniaturized low-power electronics and wireless devices are ubiquitous in everyday life. However, there is still significant interest to further reduce size, lower the power and improve data rate required by such systems. For such goals, antennas still constitute a major bottleneck in terms of size, efficiency, polarization and radiation pattern. Also for many near ground applications, low profile small antennas with vertical polarization are needed to achieve much lower propagation path loss.

Conventional approaches to reduce the height of monopole antennas cause significant drop in efficiency and polarization purity. Two novel miniaturization techniques are presented for different levels of size reduction ($\lambda/300 < h < \lambda/45$ where h is antenna height). For $h \approx \lambda/45$, a novel inductively coupled capacitively loaded antenna topology is presented, which enables up to 9dB higher gain than the conventional

inverted-F antenna with a small ground plane. For extremely short monopole antennas with h ≈ λ/300, an in-phase two-element monopole antenna topology is demonstrated, which exhibits 16.5 dB higher gain than the conventional inverted-F antenna having the same dimensions. Also, radiation pattern deformation caused by low profile configurations on a small ground plane is addressed and, to solve this problem, novel designs using vertically and horizontally balanced architectures are introduced. For GPS or mobile platforms where the aforementioned miniaturized antennas with vertical polarization cannot provide reliable communication connectivity, a new miniaturization technique is presented to reduce the size of circularly polarized (CP) patch antennas. 75% size reduction is achieved compared to a conventional patch antenna and it is 25% smaller than the smallest CP patch antenna reported in the literature. Lastly, a novel approach to combine the miniaturized monopole and patch antenna elements into a compact common aperture diversity antenna is presented for MIMO applications. This achieves a compact size of 0.27λ X 0.27λ X 0.09λ and low envelop correlation (<-30dB) between radiation patterns of two antenna elements composing the diversity antenna.

Chapter 1

Introduction

1.1 Motivation

With the great evolution of wireless technologies, the range of wireless applications and communications standards continue to grow at an unprecedented pace [1], [2]. Fig 1.1 shows a significant increase in the number of the communication standards resulting from the increasing demand for data. This requires highly integrated and power efficient RF front-ends to achieve wireless connectivity in ever-smaller and battery sensitive mobile devices. In order to satisfy the demanding space constraints imposed by the wireless devices, the volume of active circuit elements has been amazingly reduced. Fig. 1.2 illustrates the size reduction over time of the "typical" state-of-the-art commercial voltage controlled oscillator (VCO) module [3]. For the most recent 10 years, the size is reduced by a factor of 10 with enhanced performance. On the other hand, although there have been significant efforts towards antenna miniaturization, the antennas integrated with such active elements are still bulky and have a low efficiency. Fig 1.3 shows antenna dimensions and locations on the Samsung Galaxy S [4]. This suggests that the antennas occupy almost the whole volume of RF modules. Furthermore, for recent low-frequency wireless applications such as ground and

biomedical sensor networks, design of efficient antennas with small form factor is getting more challenging [5]–[7]. In radio wave propagation, selecting operating frequencies of wireless systems as low as possible can mitigate signal attenuation and fading effects significantly because at lower frequency, the distance between a transmitter and receiver and the size of scatterers look effectively much smaller, which results in better wave penetration through obstacles. However, under the fixed physical volume, design of electrically smaller antennas using conventional approaches causes significant drops in bandwidth, radiation efficiency and polarization purity, and deformation in radiation pattern. Therefore, this dissertation focuses on the study of novel antenna miniaturization techniques considering the aforementioned performance parameters.
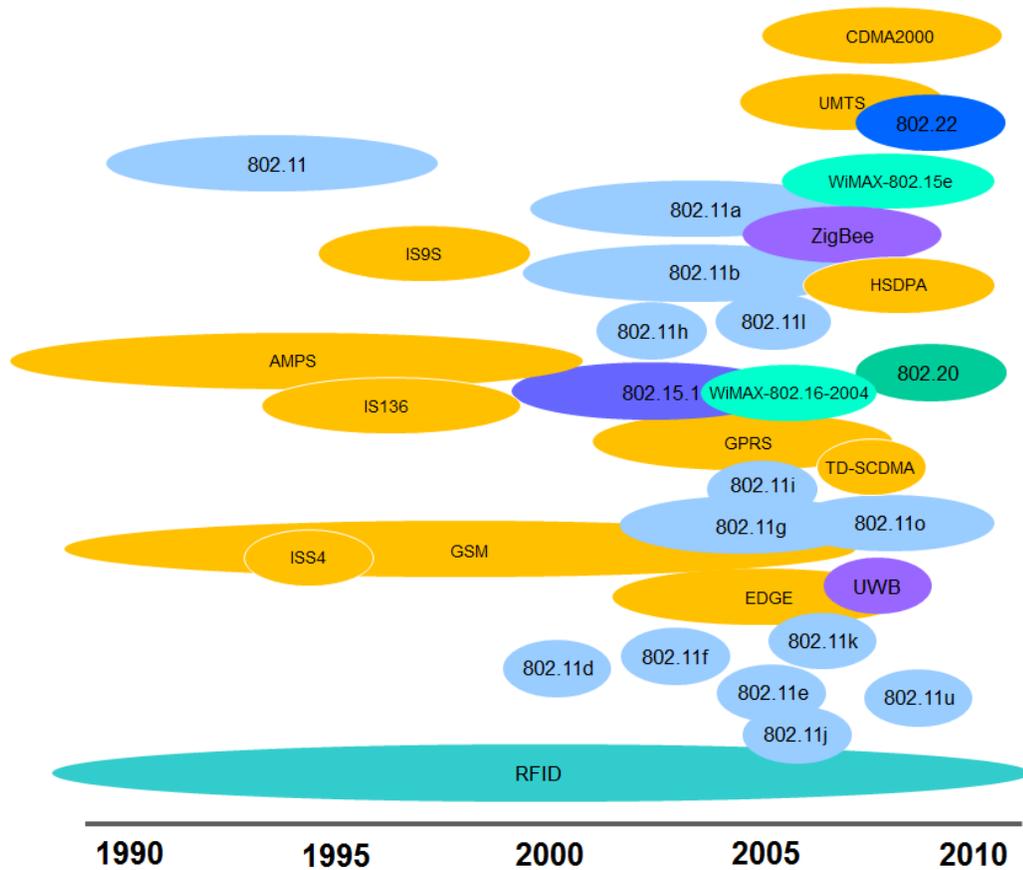
Figure 1.1: "Logjam" in communication standards due to the increasing demand for data [1].

2
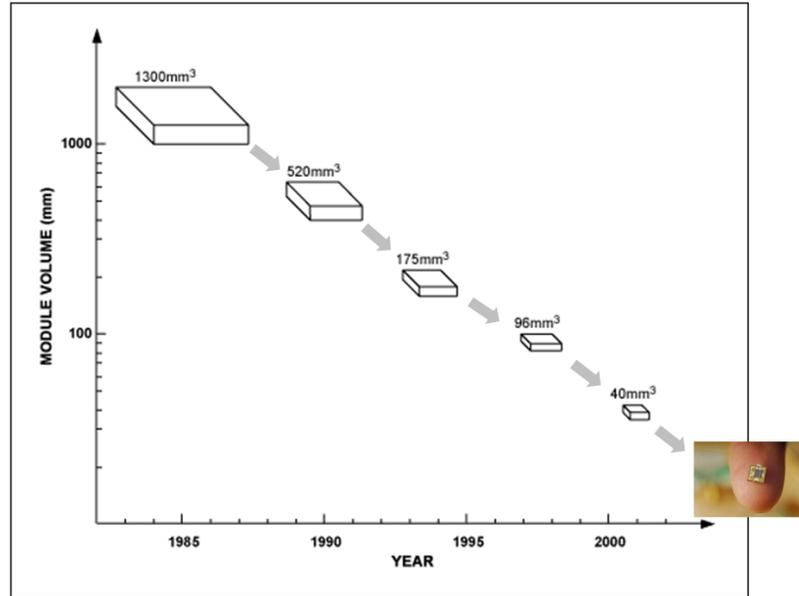
Figure 1.2: VCO module size scaling versus time [3].
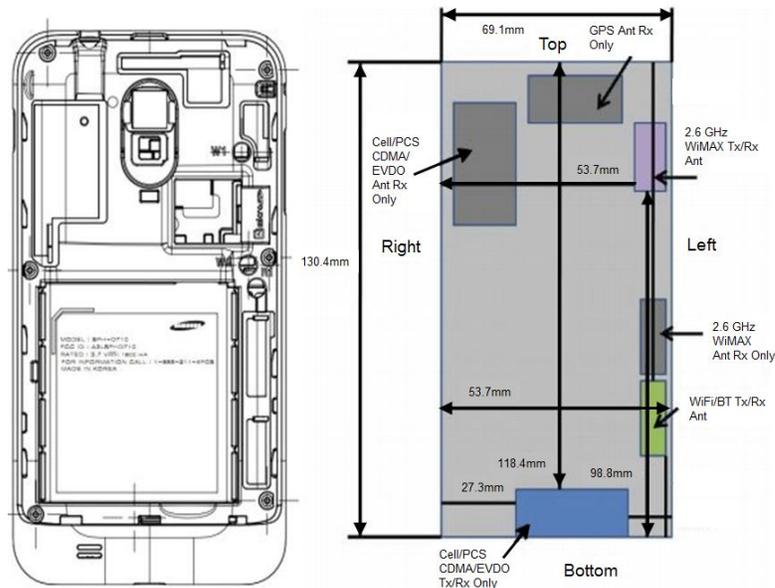
Figure 1.3: Antenna dimensions and locations on the Samsung Galaxy S [4].

For near-ground communications among ad-hoc nodes of wireless devices used in vehicles or unattended ground sensors operating at low frequencies, low profile antennas with vertical polarization and omnidirectional radiation pattern are highly desirable. The need for vertical polarization stems from the fact that near-ground propagation path loss between two near-ground antennas for vertically oriented antennas is by many orders of

magnitude lower than any other antenna orientation configurations [8]-[10]. The omnidirectional radiation characteristic is needed for wide coverage in all directions. For applications where the orientation of transmitting or receiving antennas may vary, such as mobile platforms and GPS, circularly polarized (CP) antennas are desirable because CP can maximize the polarization efficiency and improve the propagation link budget for such wireless platforms [11]. Considering that most miniaturization techniques are developed for linearly polarized antennas, a new approach to further reduce the size of the CP patch antennas is needed. Lastly, in the next generation of mobile communication systems there is a stringent demand for high speed and high quality data transmission of the mobile terminals. This makes Multiple-Input Multiple-Output (MIMO) technology attractive for its excellent performance in channel capacity without occupying extra spectrum and radiating power [12]. In the MIMO systems, antenna diversity is a well-known technique to enhance the performance of wireless communication systems by reducing the multipath fading and co-channel interference [13], [14]. Large volume that antennas in such diversity systems occupy remains a critical problem in implementing small wireless platforms.

1.2 Current State of the Art

In the studies regarding low profile monopole antennas with vertically polarization, the antennas are usually loaded with horizontal resonant structures. Inverted L and Inverted F antennas are the examples of the folded-type resonant loading structures that are commonly used [15], [16]. However, in most of such antenna topologies with a small ground plane, only a short vertical segment of the resonant structure contributes to

the vertically polarized radiation, while the much larger portion of the antenna structure generates higher radiation with undesired polarizations. This causes a low polarization purity and serious deformation in the desired omnidirectional radiation pattern [17]. Fig. 1.4 and 1.5 illustrates these problems. Fig 1.4 shows side views of 1. Straight $\lambda/4$ monopole antenna, 2. Inverted-F antenna and 3. Meandered inverted-F antenna on the small ground plane. When quarter-wave ($\lambda/4$) monopole antenna is folded to be a low profile shape, a main beam direction is changed, as shown in Fig. 1.4(b), leading to the decrease of antenna gain in the azimuthal (H) plane. It should be noted that with an infinite ground plane, this doesn't occur due to ideal images of electric currents on the horizontal resonant structures. In addition, a meandering shape used to reduce the lateral (horizontal) dimensions of the low profile antenna causes tailoring the electric current path, leading to serious deterioration in polarization purity, as shown Fig. 1.4 (c). Also, the meandered inverted-F antenna suffers from low efficiency due to high ohmic and proximity losses from thin metallic traces. Fig 1.5 shows 3D radiation patterns corresponding to vertical polarization (E_θ) of the straight $\lambda/4$ monopole antenna and meandered inverted-F antenna. This suggests that in the azimuthal plane (H-plane) the gain of the miniaturized antennas on the small ground plane can be 10dB lower than that of the original $\lambda/4$ monopole antenna. In [18]–[23], interesting capacitively loaded monopole antennas with different especial disk geometries are presented as means for reducing the antenna height and improving the bandwidth. The heights of these antennas are in the range of $\lambda/10$, presenting excellent operational bandwidth. However, their lateral dimensions are still large, comparable to the wavelength.
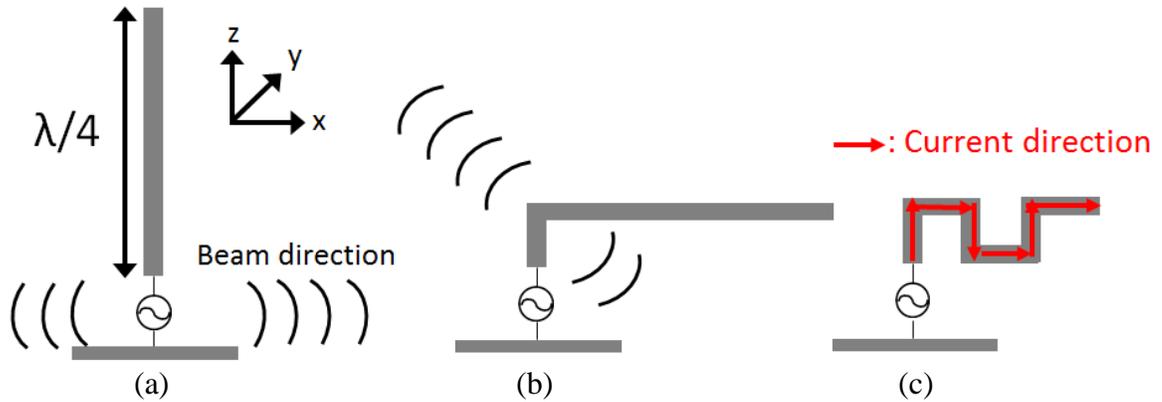
Figure 1.4: Side views of (a) straight λ/4 monopole antenna, (b) inverted-F antenna and (c) meandered inverted-F antenna on small ground plane.
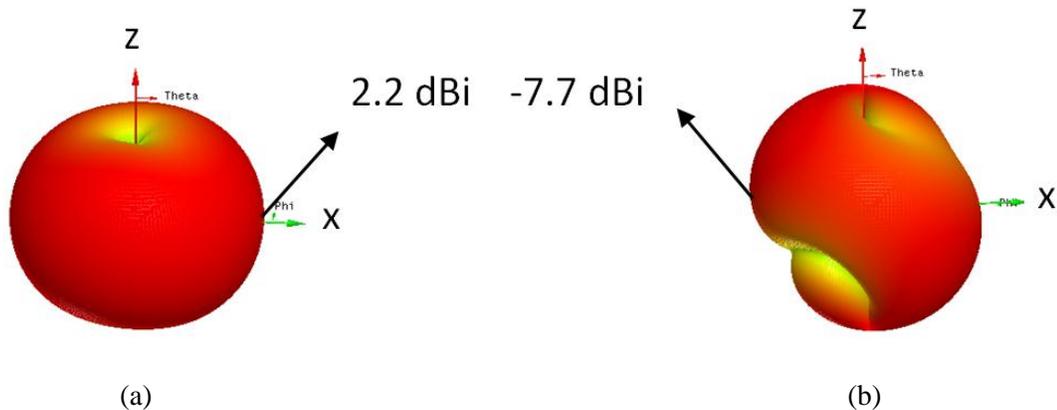
Figure 1.5: 3D radiation patterns corresponding to vertical polarization (E_θ) of (a) the straight λ/4 monopole antenna and (b) meandered inverted-F antenna.

For GPS or mobile platforms where the aforementioned low profile antennas with vertical polarization cannot provide reliable communication connectivity, a circularly polarized (CP) antenna with a low profile, small size and light weight is highly desirable. However, antennas with extremely small lateral dimensions have very low capability in internally generating the required conditions for CP operations: 1. Two orthogonal linearly polarized components of the radiated fields, 2. Equal amplitude and a 90° phase difference of the two components and 3. Impedance matching to a 50 ohm feed at the two degenerate orthogonal modes. Many compact CP patch antennas have been proposed and investigated [24]–[25]. These efforts have relied mainly on intuitive techniques such

6

as inserting several slots or slits in suitable locations on the patch itself. In such antenna designs, the splitting of two near-degenerate orthogonal modes with equal amplitudes and a 90° phase difference is achieved by slightly adjusting the embedded slots, such as a cross-slot in a patch or slits at the boundary of the patch. Theses inserted slots and slits force redirection of the excited fundamental mode surface current and also cause the resonant frequency to be shifted down to some extent. However, this approach has yielded somewhat limited miniaturization due to lack of ability to simultaneously control the surface current paths as well as create the required 90° phase difference. It is shown that these methods can provide size reductions of as low as 50%.

For MIMO applications requiring high data rate, compact diversity antennas composed of miniaturized low profile monopole and patch antenna elements are desirable. In [26]–[28], the reductions in antenna size have been achieved for individual antenna elements. However, compact diversity antennas have not been well studied. The current approach to achieve antenna diversity is based on placing two or more individual compact antennas in optimized positions that provide low envelope correlation (ρ_e) where the envelope correlation is defined by a correlation between radiation patterns of two individual antenna elements [26]. This approach is good but the overall volume that the antennas occupy increases directly with their number and becomes too large for compact wireless applications.

The focus of this thesis is to address the limitations of these current approaches by introducing new approaches with novel antenna topologies to achieve high radiation efficiency, high polarization purity, omnidirectional radiation pattern with small ground plane, low envelope correlation between two miniaturized antennas, maintaining a small

form factor. The novelties of the proposed antenna miniaturization techniques are demonstrated by comparing the performance of the proposed miniaturized antennas with that of the conventional miniaturized antennas. The proposed antenna miniaturization techniques in this dissertation contribute to designing novel antenna topologies and RF systems, which are introduced in *IEEE Antennas and Propagation Society* [17], [29]-[36].

1.3   Dissertation Overview
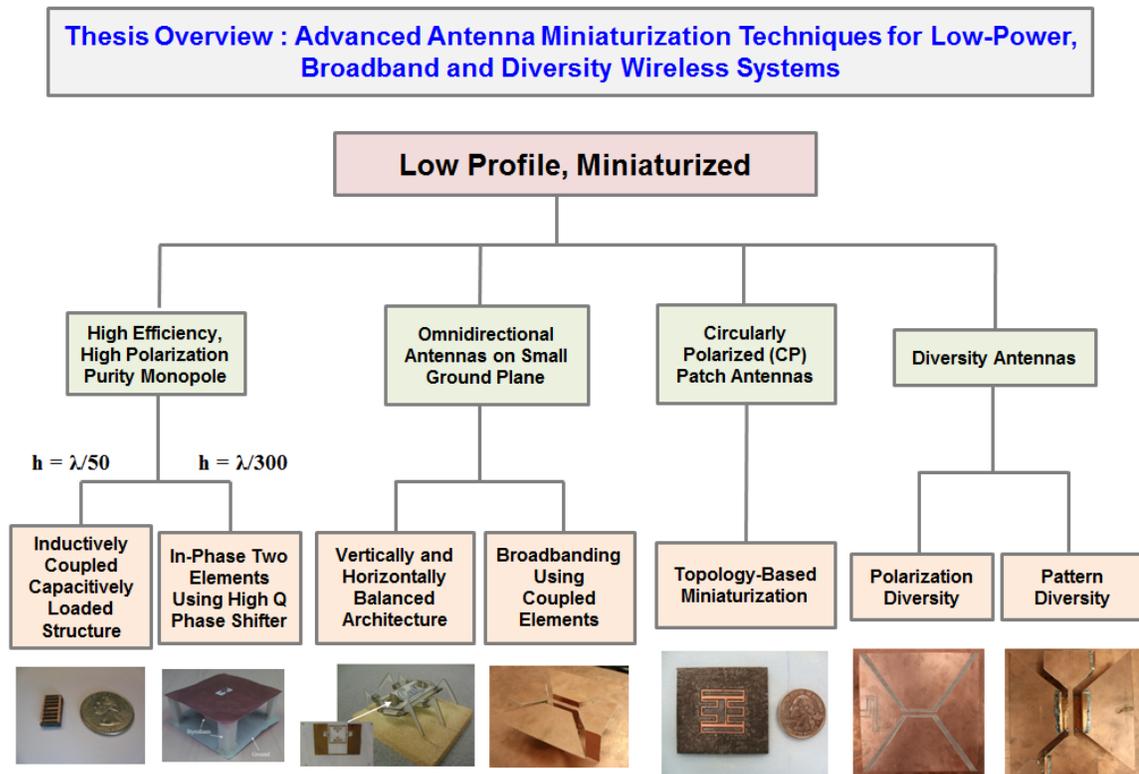
Figure 1.6: Dissertation overview.

1.3.1 Chapter 2: Design of Electrically Short Monopole Antenna with High Efficiency and High Polarization Purity

Techniques are introduced to improve radiation efficiency and polarization purity of electrically short monopole antennas. The first technique is to embed the additional

coupled structure into the conventional planar inverted F antennas (PIFA) to suppress the level of the electric surface currents with undesired polarizations. The first technique is successfully applied for the short monopole antennas with the height of $\lambda/45$ and lateral dimensions of $\lambda/16$ X $\lambda/8$. This antenna is called by "Low Profile Inductively Coupled Capacitively Loaded Antenna". However, it is found that for extremely small monopole antennas with the height of less than $\lambda/100$ the first technique is not available and thus a new technique utilizing two in-phase radiating elements and a low-loss phase shifter is proposed. In order to minimize the loss of the phase shifter, a novel use of air-core solenoids is introduced. The dimensions of the short monopole antenna designed based on the approach are extremely small as $\lambda/300$ X $\lambda/100$ X $\lambda/100$.

1.3.2 Chapter 3: Realization of Omnidirectional Radiation Pattern/Broad Bandwidth for Low Profile Antennas on a Small Ground Plane

Techniques are presented to realize omnidirectional radiation pattern for the low profile antenna on a small ground plane ($<<\lambda$). It is shown that the radiation pattern of conventional inverted F antenna on small ground plane is distorted and as a result, the radiated power along the azimuthal plane (H-plane) of the antenna is significantly decreased.

The first approach to solve this problem is to utilize a balanced architecture in the middle of which a null plane exists similar to the geometry of dipole antennas. The second approach is to cancel out the radiated fields with undesired polarization by manipulating the geometry of top plate of low profile antennas. In addition, a

broadbanding technique compatible with the aforementioned miniaturization techniques for realizing omnidirectional radiation pattern is presented.

1.3.3 Chapter 4: A Topology-Based Miniaturization of Circularly Polarized Patch Antennas

A novel approach for the miniaturization of circularly polarized patch antennas is presented. This enables a size reduction of as high as 75%, compared to a conventional corner-truncated circularly polarized patch antenna. The proposed design procedure consists of a number of intermediate steps, each of which produces antenna miniaturization as well as the desired polarization and impedance matching properties. This is very challenging in miniaturizing circularly polarized probe-fed patch antennas. At the initial design step, a patch antenna topology made of an anisotropic conductor that only supports the desired electric current distribution, is considered. The anisotropic conductivity is achieved by 1) replacing the metallic patch with a set of thin parallel wire grids aligned in the direction of the desired electric current and 2) connecting them with two perpendicular metallic strips at each end. Next, the straight metallic traces are meandered for size reduction, creating a miniaturized linearly polarized patch antenna. To achieve circular polarization, a second mode is excited by elongating the end strips so that they resonate at the same frequency. Also, the feed point is chosen so as to achieve impedance matching and a 90° phase shift. It is shown that two resonant frequencies can be tuned independently to produce a dual band antenna with two orthogonal polarizations. Finally, two circularly polarized miniaturized patch antennas with different miniaturization factors are fabricated, and their input impedances, radiation patterns and axial ratios are discussed.

1.3.4 Chapter 5: Design of Compact Co-Located Polarization/Pattern Diversity Antennas Using a New Class of Microstrip Antennas

Compact co-located planar polarization/pattern diversity antennas using a new class of microstrip antennas are presented. The proposed microstrip antenna has an open area in its middle, physically splitting a single body of the conventional microstrip antenna into two. The two bodies are magnetically coupled through two vertical shorting plates each of which is connected to each body. A great advantage of this antenna topology is that another antenna element can be placed in the open area, achieving the design of compact diversity antennas with low envelop correlation. Topologies of polarization and pattern diversity antennas incorporating the proposed microstrip antenna and another antenna placed in the open area are introduced. Although the proposed diversity antennas consists of two antenna elements with different polarizations or radiation patterns, their areas are just about 30% of the area of the conventional microstrip antenna with the dimension of $\lambda/2$ X $\lambda/2$. In addition, for both types of the proposed diversity antennas, the envelop correlations between radiation patterns of the two antenna elements composing each diversity antenna are lower than -30dB over the 10-dB return loss bandwidth of the proposed microstrip antenna.

Chapter 2

Design of Electrically Short Monopole Antenna with High Efficiency and High Polarization Purity

In this chapter, depending on desired levels of size reduction, two miniaturization techniques to achieve high efficiency and polarization purity are presented: 1. Inductively coupled capacitively loaded structure ($h \approx \lambda/45$ where h is antenna height) and 2. Two in-phase radiating elements realized by high-Q phase shifter ($h \approx \lambda/300$).

2.1 Low Profile, Miniaturized, Inductively Coupled Capacitively Loaded Monopole Antenna

2.1.1 Introduction

Vertically polarized antennas with omnidirectional radiation pattern are highly desirable for many applications including near-ground communications among ad-hoc nodes of wireless devices used in vehicles or unattended ground sensors operating at low frequencies. The need for vertical polarization stems from the fact that near-ground propagation path loss between two near-ground antennas for vertically oriented antennas is by many orders of magnitude lower than any other antenna orientation configurations [8], [9]. In fact, this is the main reason $\lambda_0/4$ monopole antennas with vertical

polarization and omnidirectional radiation pattern are prevalent in many communication devices working near the ground. However, as wireless communication devices continue to evolve, the large dimension of the antenna is frequently problematic. Therefore, it is imperative to further investigate methods of realizing extremely short monopole antennas with very small lateral dimensions, while maintaining high radiation efficiency. This will allow ease of integration of such antennas with the package or platform of small wireless devices that are emerging. Recently, different types of low-profile antennas with omnidirectional radiation pattern have been proposed. Among these, one approach is to excite radiation from short segments of loaded vertical wires, and the other one is based on exciting a cavity-backed small slot loop antenna [38], [39].

In the studies where short segments of vertical wires are utilized as the intended radiators, the antennas are usually loaded with horizontal resonant structures. Inverted L and Inverted F antennas are the examples of the folded-type resonant loading structures that are commonly used [15], [16]. One drawback of these structures is the energy radiation in the horizontal polarization that stems from relatively large lateral dimension of the loading structures. This, of course, leads to lower gain in the desired polarization channel. In [18]–[23], interesting capacitively loaded monopole antennas with different especial disk geometries are presented as means for reducing the antenna height and improving the bandwidth. The heights of these antennas are in the range of $\lambda_0/10$, presenting excellent operational bandwidth. However, their lateral dimensions are still comparable to the wavelength. For certain applications where the bandwidth can be compromised, it is found that by loading the planar inverted-F antenna (PIFA), the lateral dimension of the antenna can be reduced to $\lambda_0/8$ [40]-[42]. In [42], a via-patch is added

13

inside a conventional PIFA leading to an easier design and fabrication. By changing the height and location of the vias, different degree of size reduction could be obtained, providing more design freedom. Nevertheless, these antennas include a multilayer geometry that cannot be realized using simple PCB fabrication process.

Recently, an extremely short monopole antenna ($\lambda_0/60$- $\lambda_0/40$), known as LMMMA, with omnidirectional radiation pattern and vertical polarization was introduced [37]. The concept is based on superposition of multiple quarter-wave segments that are meandered and spiraled around to suppress the radiation from horizontal currents above the ground plane. In other words, the cancellation of the horizontal electric current is achieved by introducing another set of electric current that is in the opposite direction in the horizontal plane of the antenna with the original electric current at electromagnetic resonance. As a result, the antenna features a vertically polarized radiation in the horizontal plane. Although the antenna produces almost purely vertical polarization, it suffers from low gain due to high ohmic loss of the spiral metallic traces. Hence, it is obvious that more effort will be needed to come up with a design for increasing the gain of extremely short antennas with very small lateral dimensions. For most monopole low-profile antennas, the size of the ground plane is chosen to be large or moderately large compared with the wavelength [44]–[46]. The size of the ground plane affects the uniformity of the radiation pattern and the gain near the horizontal plane ($\theta = 90°$) due to the edge diffraction [47]. For very small platforms, the size of the ground plane must be comparable with the lateral dimensions of the antenna itself.

In this work, a novel low profile miniaturized antenna with omnidirectional radiation pattern and vertical polarization is presented. To suppress the radiated fields

14

from horizontal currents over a top load the horizontal currents are distributed uniformly over a large metallic top load. However, the use of this large top load in miniaturized antennas prohibits the use of thin shorting pins because impedance matching to 50 ohm cannot be obtained without the increase in the dimension of the shorting pins. In the proposed antenna, a new in-plane capacitive coupled structure is introduced for compensating inductive coupling between the thin pins. Finally, the use of the large top load, shorting pin and in-plane capacitive coupled structure achieve improved polarization purity and excellent impedance matching with antenna miniaturization. An equivalent circuit model of the proposed antenna is developed for the ease of design. The improved performance of the proposed antenna is compared to that of ordinary inverted F antennas and the more recent low profile vertically polarized antennas. A two-layer antenna is described first to explain the principle of operation. With the help of the equivalent circuit model, this design is then modified to achieve a single-layer counterpart of the same antenna for the ease of fabrication. Furthermore, the design procedure and tradeoff study to reduce the lateral dimension of ICCLMA at the cost of lowering the gain are presented. The proposed antennas are fabricated and measured to validate the design method. It is pointed out that an antenna with an electrically very small ground plane cannot be measured accurately using a common unbalanced coaxial feed. A new gain and pattern measurement method using a balanced version of the monopole (dipole type) antenna is presented.

2.1.2 Inductively Coupled Capacitively Loaded Monopole Antenna (ICCLMA)

2.1.2.1 Concept of ICCLMA

As mentioned before, one of the drawbacks of the very short miniaturized monopole antenna (LMMMA) is its low radiation efficiency resulted from the strong electric currents concentrated on the horizontal thin metallic traces. However, establishing this current is necessary to establish the required high current level on the short vertical pin which is the main radiating component of the antenna. As the height of the antenna decreases, higher level of current is required and thus the antenna radiation efficiency gets lower. In order to increase the gain, we need to suppress the radiated fields from horizontal currents over the resonating structure, while keeping the lateral dimensions small. This can be accomplished by using a large capacitive top-load as well as high Q lumped-type resonant structures built by separating the radiating structure (=the secondary circuit) from the feed structure (=the primary circuit) using a magnetic coupling and an additional capacitive coupling.

(a)   (b)
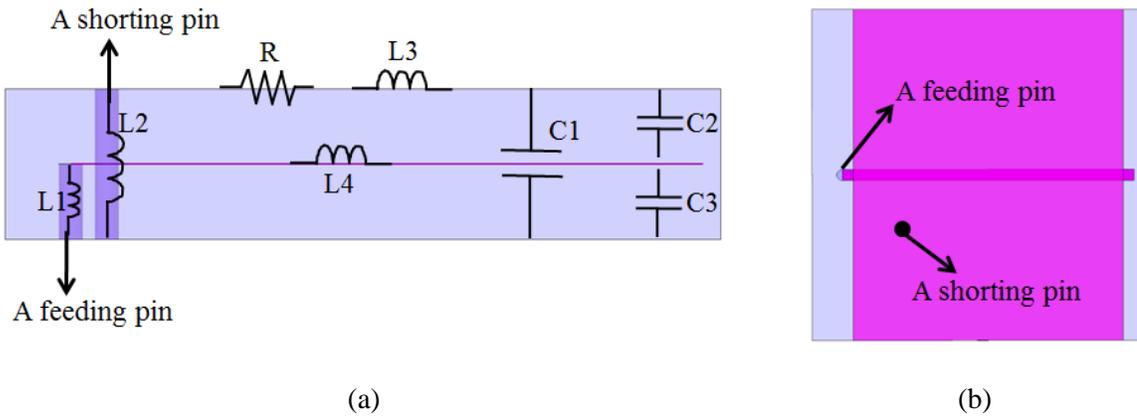
Figure 2.1: (a) Equivalent circuit model drawn in side view and (b) top view of a multilayer ICCLMA.

The high-Q resonant structure consists of magnetically-coupled two pins acting as a transformer, a relatively wide metallic patch acting as a capacitor and an additional capacitive coupling between the feed structure and the radiating structure. The desired

16

operation of the transformer can be realized by the proper placement of a feeding pin and the shoring pin in the resonator which is a vertical element responsible for vertically polarized radiation. The salient feature of the proposed antenna is the fact that the internal elements of the antenna structure are used for the desired functionality and impedance matching without the need for lumped elements or external matching network. Otherwise, the use of external lumped elements will render poor radiation efficiency. As will be shown, the transformer coupling, capacitance of the top load and other capacitances can be adjusted to achieve the impedance matching as well as obtaining the resonant condition at a proper frequency.

2.1.2.2 Multilayer ICCLMA and Equivalent Circuit Model

The topology of ICCLMA designed initially consists of three layers as shown in Fig. 1(a). This includes a ground plane, a thin metallic trace, and a wide metallic patch that are, respectively, placed in the bottom, the middle and the top layers. Fig. 2.1(a) also depicts an equivalent circuit model superimposed over the side view drawing of the proposed multilayer ICCLMA. This circuit model helps the arrangement of different structural components of the antenna. A vertical feeding pin and a shorting pin are inductively coupled. While the feeding pin is connected to a narrow metallic trace in the middle layer, the shorting pin is attached to a wide metallic plate in the top layer. The top view of the structure shown in Fig. 2.1(b) indicates the position of the shorting pin to be offset from the symmetry plane in the center and a short distance away from the feeding pin. In other words, the shorting pin does not touch the metallic trace in the middle layer and thus the radiating structure can be coupled to the feed magnetically.

17

The resistance (R) in the equivalent circuit represents the sum of the radiation resistance, ohmic loss in metals, dielectric loss and surface wave loss. The top wide metallic surface is represented by a shunt capacitor in the secondary circuit of the transformer in the circuit model. The uniform current distribution supported by the wide copper sheet on the top layer leads to significant reduction of the ohmic loss. Additional capacitances are introduced due to the placement of a narrow metallic trace in the middle layer. One very important feature of the new design is that the antenna input impedance can match to almost any desired value between 10 and 100 Ohm. Impedance matching can be achieved by adjusting the parameters of the transformer and the values of capacitors and inductors shown in the circuit model. The coupling coefficient of the transformer corresponds to the distance between a feeding pin and a shorting pin. The values of the inductance and capacitances are related to the diameter of two pins and the width, length and height of metal sheets, respectively.
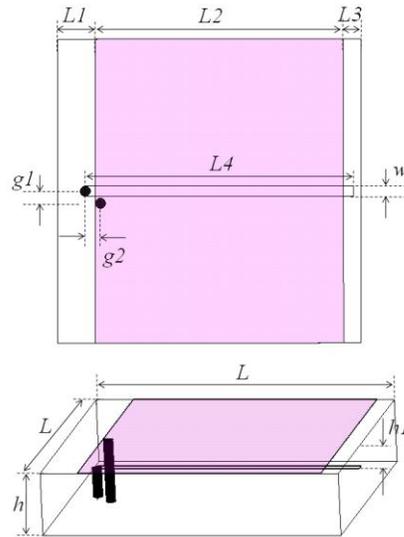
Figure 2.2: Design parameters of a multilayer ICCLMA.

Design parameters are shown in Fig. 2.2. Their value are given by $L = 15$ mm $= \lambda_0/8$, $h = 3.14$ mm $= \lambda_0/40$, $L1 = 1.875$ mm, $L2 = 12.25$ mm, $L3 = 0.875$mm, $L4 = 13.25$

mm, $h1 = 1.57$ mm, $w = 0.5$ mm, $g1 = 0.6$ mm and $g2 = 0.75$ mm where λ_0 is free-space wavelength at the resonant frequency. The diameters of the two pins are chosen to be 0.5 mm. The substrate used in this design has a dielectric constant of 2.2 and dielectric loss tangent of 0.0009. In order to consider ohmic loss, conductivity of copper is used in all metallic traces and vertical pins in the full-wave analysis.

It is interesting to examine whether the equivalent circuit model can predict the behavior for the proposed antenna structure. The values of the lumped elements in Fig. 2.3 are first derived from the design parameters in Fig. 2.2 and slightly adjusted, based on full wave simulation results. Fig. 2.4 shows the real and imaginary parts of input impedance which are derived from a circuit (Advanced Design System 2009) and full wave (Ansoft HFSS 12) simulator. It is shown that the two results are in very good agreement, meaning that the equivalent circuit model can predict the performance perfectly. Simulated S_{11} in Fig. 2.5 indicates good impedance matching and fractional 10-dB return loss bandwidth of 0.45% due to high quality factor.

The vertically (co-) and horizontally (cross-) polarized radiation pattern in the E-plane and H-plane are presented in Fig. 2.6(a) and (b). The co-polarized radiation pattern is omnidirectional pattern with the direction of maximum gain occurring at $\theta = 90°$. While the gain of co-polarized radiation at $\theta = 90°$ near ground observation is 0.46 dBi, the gain of cross-polarized radiation at $\theta = 90°$ is less than dBi. As expected, the proposed antenna provides excellent suppression of horizontally polarized radiation.
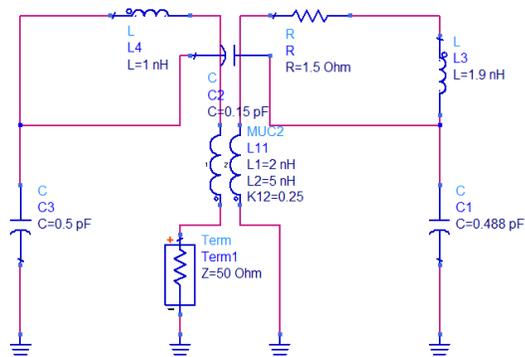
Figure 2.3: Equivalent circuit model of a multilayer ICCLMA.
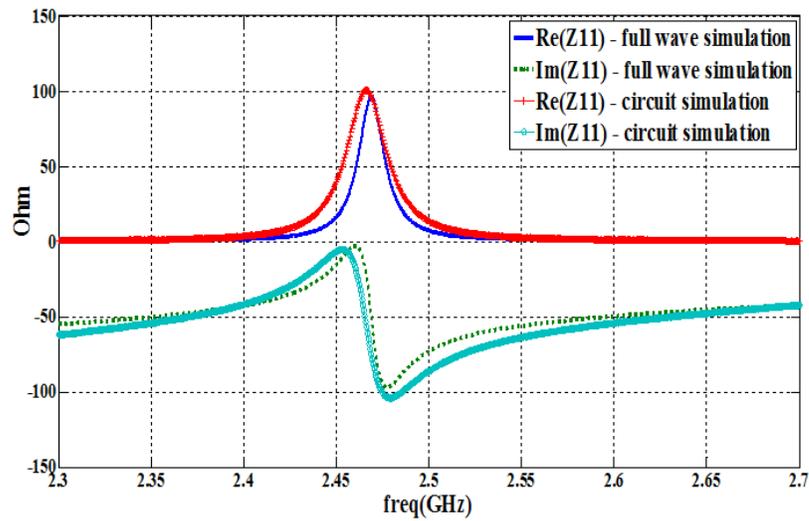
Figure 2.4: Real and imaginary parts of input impedance simulated by full wave and circuit simulators.
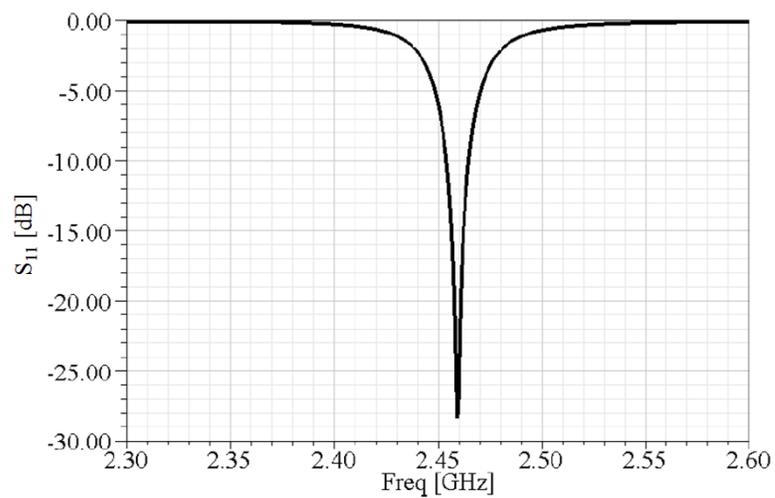
Figure 2.5: Simulated S_{11} when $L = \lambda_0/8$ and $h = \lambda_0/40$.

20
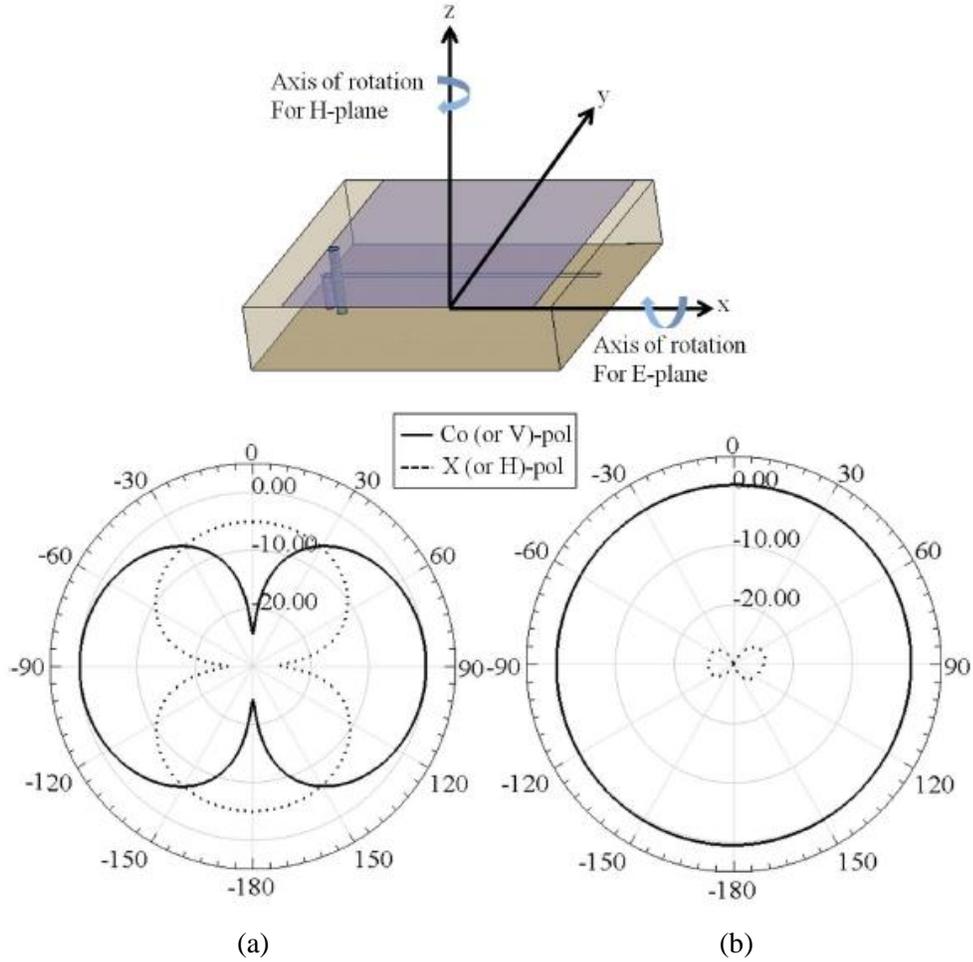
Figure 2.6: Simulated (a) E-Plane and (b) H-Plane radiation patterns when L = $\lambda_0/8$ and h = $\lambda_0/40$

2.1.2.3 Bench Marking

In this section, the performance of the proposed antenna is compared with those of other low-profile antennas reported in the literature. This comparison includes the size, gain, and polarization purity of the proposed antenna against a conventional inverted F antenna and the multi-element monopole antenna (MMA) introduced in [37]. Two antennas with the same height (= 3.14 mm = $\lambda_0/40$) as that of the proposed antenna, are designed as shown in Fig. 2.7. To address a general drawback of low profile antennas designed using a $\lambda_0/4$ open circuited transmission line, the conventional inverted-F antenna with a $\lambda_0/4$ open circuited transmission line, the conventional inverted-F antenna

with a $\lambda_0/4$ open circuited transmission line, the conventional inverted-F antenna with a $\lambda_0/4$ thin metallic trace is chosen. The drawback is poor polarization purity caused by very small height of the antenna ($=\lambda_0/40$) and horizontal current flowing along the thin metallic trace in one direction. While MMA has the same ground plane size as that of the proposed antenna, the conventional inverted-F antenna has larger ground plane since no miniaturization technique is applied. The simulated gain and the dimension of these antennas and the proposed antenna are presented in Table 2.1. For the case of an inverted-F antenna, horizontal polarized gain ($=-2.1$ dBi) on H-plane is dominant over the expected vertical polarized gain ($=-8.7$ dBi). Although MMA has the improved gain due to the efficient cancellation of horizontal current, its gain is still low as -3.6 dBi because of high ohmic loss generated from narrow metallic traces. For the proposed antenna, the gain is substantially improved ($=0.46$ dBi) and is 9 dB higher than that of the conventional inverted F antenna. Moreover, the new antenna has 4 dB higher gain than the MMA with the same physical dimensions, as shown in Table 2.1. At $\theta = 90°$ (near ground observation), the ratio of horizontally to vertically polarized gain is less than 25 dB, suggesting excellent suppression of the radiation in horizontal polarization.

TABLE 2.1
GAIN AND DIMENSION OF A CONVENTIONAL INVERTED-F ANTENNA, MMA
AND PROPOSED ANTENNA

Antenna type	Lateral dimension (mm X mm)	Height (mm)	Radiation Efficiency (%)	Gain (Co-pol.) on H-plane (dBi)	Gain (X-pol.) on H-plane (dBi)	Co-pol to X-pol (dB)	BW(%)
Inverted F Antenna	15 X 36	3.14	61.46	-8.7	-2.1	-6.6	0.62
MMA	15 X 15	3.14	44.57	-3.6	-5.2	1.6	0.49
ICCLMA	**15 X 15**	**3.14**	**70.89**	**0.46**	**-25.9**	**26.3**	**0.47**
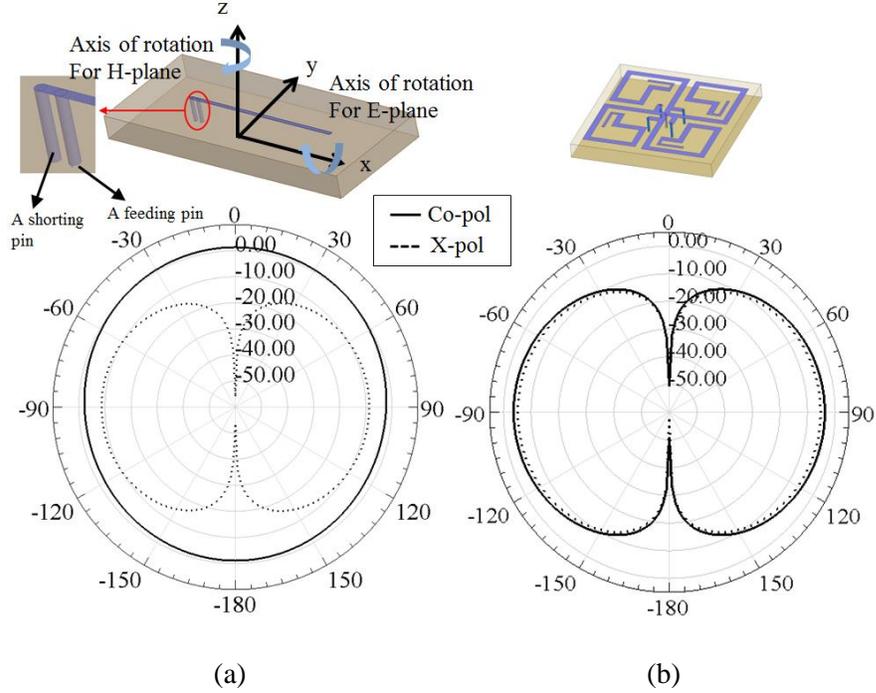
Figure 2.7: E-Plane radiation patterns of (a) a conventional inverted-F antenna and (b) multi-element monopole antenna with the same vertical profile as the height of the proposed antenna ($=\lambda_0/40$).

2.1.3 Single-Layer ICCLMA and Additional Size Reduction

2.1.3.1 Single-Layer ICCLMA

In the previous section, it was shown that the gain of a multilayer ICCLMA is greatly higher than that of other existing low-profile miniaturized antennas. However, the complexity of the multilayer geometry cannot be ignored. This architecture requires complex multilayer-printed circuit fabrication and is subject to alignment errors and higher cost. This is perhaps the reason why multilayer low-profile miniaturized antennas are not popular, although they have better performance [40], [42]. In this section, a modified single-layer ICCLMA having the same equivalent circuit model is presented. The multilayer structure had capacitances C2 and C3 in its equivalent circuit that are responsible for miniaturization as well as impedance matching. It turns out that the same

23

capacitances can be realized in single-layer ICCLMA architecture as shown in Fig. 2.8. The series capacitor C2 between the primary circuit and the secondary circuit is created by an in-plane interdigital capacitance, and C3 is the shunt capacitance between the strip attached to the primary circuit (left side of the interdigital capacitor) and the ground plane. Fig. 2.9 shows the simulated radiation pattern of single-layer ICCLMA having the same dimension as a multilayer ICCLMA. This antenna has a slightly lower gain of 0 dBi at the same resonant frequency.
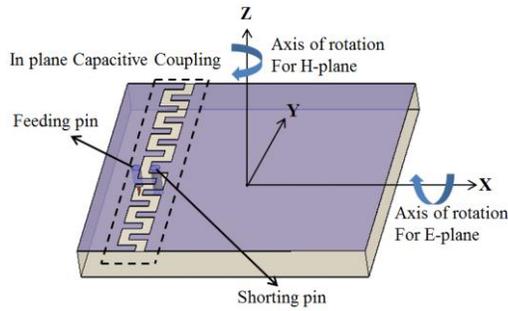
Figure 2.8: Topology of single-layer ICCLMA.

(a)   (b)
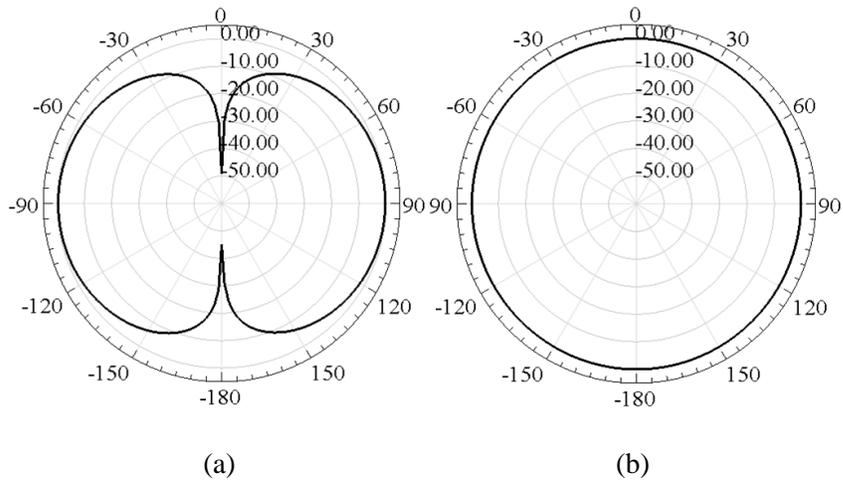
Figure 2.9: Simulated (a) E-Plane and (b) H-Plane radiation patterns of a single layer ICCLMA when $L = \lambda_0/8$ and $h = \lambda_0/40$.
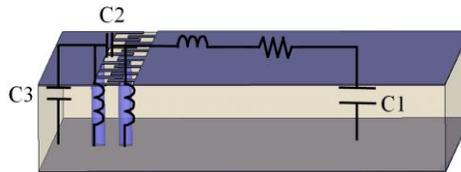
Figure 2.10: Equivalent circuit model of single-layer ICCLMA.

24
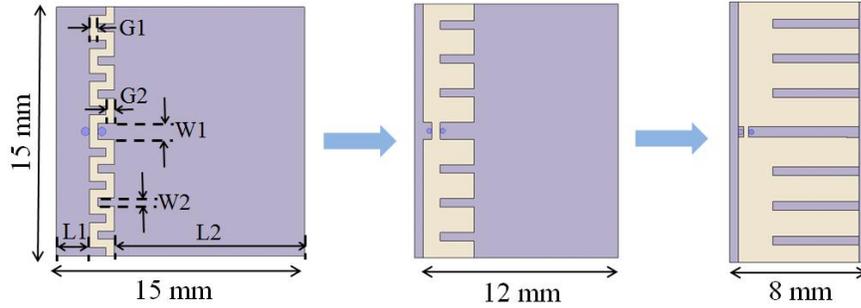
Figure 2.11: Design procedure for additional size reduction of single-layer ICCLMA.

2.1.3.2 Additional Size Reduction of Single-Layer ICCLMA

As discussed in Section 2.1.3.1, the introduction of the series capacitance C2 in the proposed ICCLMA antenna allows for the ease of impedance matching at lower frequency. This property also allows for obtaining additional size reduction of single-layer ICCLMA. Fig. 2.10 shows equivalent circuit model of single-layer ICCLMA. When C2 is changed by modifying the interdigital structure as shown in Fig. 2.11, C1 and C3 are also changed at the same time because they are proportional to the area of metal sheet on the top layer.

It is interesting to note that the proper combination of C1, C2 and C3 values can achieve excellent impedance matching of smaller antennas. Fig. 2.11 describes how this principle is applied for additional size reduction. The suitable combination of C1, C2 and C3 values can be found by changing the gap distance between two metallic sheets on the top layer (G1 and G2), the width of protruding parts of the interdigital shape (W1 and W2), as well as L1 and L2. For example, the center prong in Fig. 2.11 determines the series capacitance C2 and other prongs are modified to get the required capacitance C1. The impedance matching for three different dimensions is well achieved at the same resonant frequency as shown in Table 2.2. Finally, the size can be reduced from 15 mm

15 mm to 8 mm 15 mm, which corresponds to almost 50% size reduction. However, the size reduction comes at the expense of reduction in gain from 0 dBi to -1.9 dBi.

One important advantage of this design procedure is that smaller antennas can be perfectly matched to 50 ohm without modifying parameters related to pins such as the diameter of two pins and the gap distance between two pins, while folded low-profile antennas such as PIFA usually require changing the area of the rectangular sheet shorting the top plate when additional miniaturization is required. Furthermore, in the proposed antenna, thin pins with diameter as small as 0.5 mm are used, while most folded low-profile antennas have a wide rectangular shorting sheet that is comparable to the other antenna dimensions. This property is desirable when commercial PCB technology is used in fabrication of low-profile vertically polarized antennas. Basically, metalized via holes can be used to realize the shorting pins very accurately.

TABLE 2.2

GAIN AND RESONANT FREQUENCY OF SINGLE-LAYER ICCLMAS WITH THREE DIFFERENT DIMENSIONS

Size (mm X mm)	fc (GHz)	Gain (dB)	BW (%)	G1	G2	W1	W2	L1	L2
15 X 15	2.39	0	0.46	0.5	0.5	1	0.5	2	11.5
12 X 15	2.358	-0.6	0.38	1	3	1	0.5	0.5	8.5
8 X 15	2.362	-1.9	0.36	2	7	0.5	0.5	0.5	0.5

2.1.4 Measurements

In order to avoid the coupling to the feed line and the resulted undesirable radiation problem from the feed line connected to the antenna with electrically small ground plane, one can use a very large ground plane. The proposed antenna placed on a

large ground plane is measured by a vector network analyzer. It should be pointed out that the design parameters of the antenna on a large ground plane are slightly different from those of the same antenna on a small ground plane. A miniaturized single-layer ICCLMA on $3\lambda_0$ X $3\lambda_0$ ground plane is designed, fabricated and measured as shown in the measurement setup of Fig. 2.12. Fig. 2.13 shows the measured reflection coefficient, compared with the simulation result. A good agreement is observed. Measured radiation pattern of this antenna is compared to that of a $\lambda_0/4$ monopole antenna on the same ground plane. Fig. 2.14 shows the overall gain of the proposed antenna operating at the resonant frequency is comparable to that of a monopole $\lambda_0/4$ antenna.

(a)   (b)
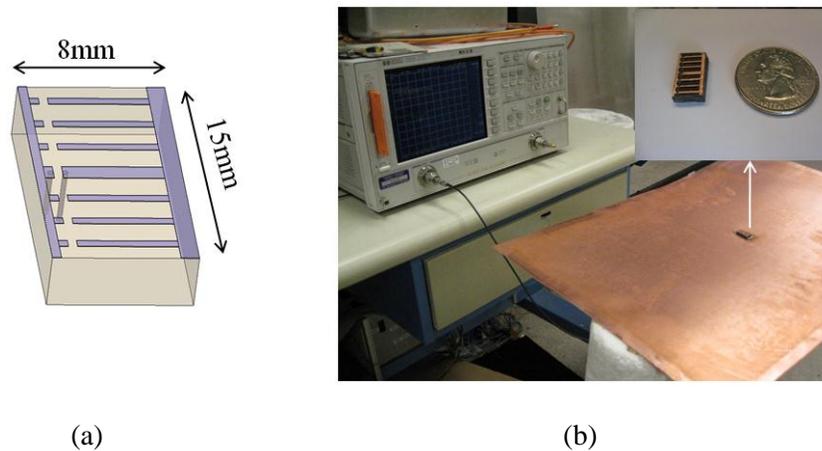
Figure 2.12: (a) Miniaturized single-layer ICCLMA and (b) measurement set up using a large ground plane ($3\lambda_0$ X $3\lambda_0$).
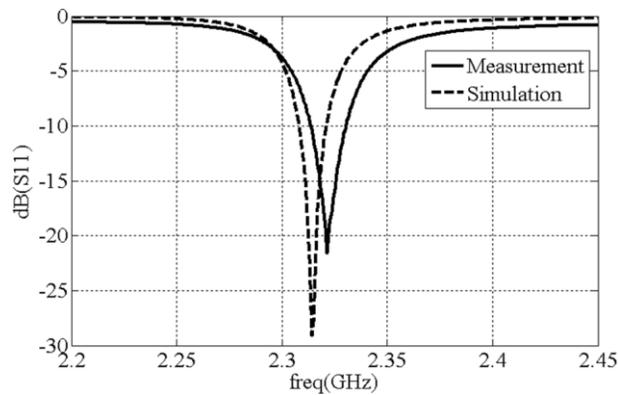
Figure 2.13: Measured and simulated S_{11} of a miniaturized single-layer ICCLMA on a large ground plane.

27
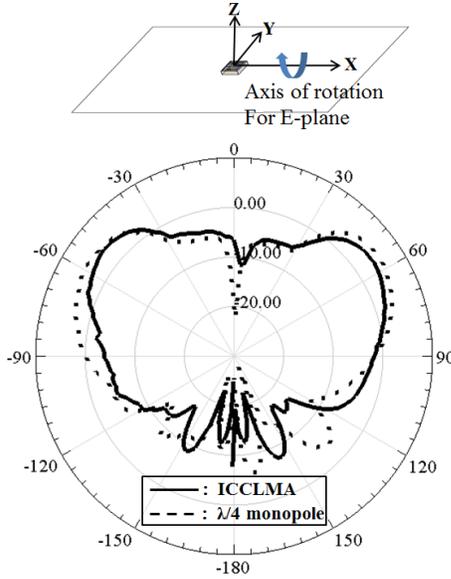
Figure 2.14: Measured E-Plane radiation patterns of a ICCLMA and $\lambda_0/4$ monopole antenna.

2.2 Extremely Small Two-Element Monopole Antenna

2.2.1 Introduction

Emerging wireless technologies increase the needs for small-size, light-weight and easily fabricated antennas. A quarter-wave monopole antenna is the most ubiquitous antenna used for many applications such as unattended ground sensors and ground-based communication systems at various frequency bands [48], [9]. However, the size of such antenna is prohibitively large for portable devices operating at low frequencies. This is particularly a major limiting factor at HF band whose applications for mobile wireless devices have been limited by the antenna size [49]-[51]. As a type of miniaturized monopole antenna, low-profile inverted-F antennas (IFA) are most commonly used. One drawback of these antennas is that as their height decreases, the gain corresponding to vertically (co-) polarized radiation drops rapidly. This performance degradation is due to the increased power loss and the increase in radiated power from cross (x-) polarized

electric currents flowing on metallic traces highly concentrated and meandered in a small area [40], [17]. However, the horizontal currents are essential in establishing the required high current level on the short vertical pin which is the main radiating component of the antennas [17]. In addition, many other types of low-profile electromagnetically coupled monopole antennas have been reported in the literature. In [18]–[23], capacitively loaded monopole antennas with different special disk geometries are presented for reducing the antenna height and improving the bandwidth. The height of these antennas is typically in the range of $\lambda_0/10$ with excellent operational bandwidth. However, their lateral dimensions are comparable to the wavelength. In [17], a new type of low-profile miniaturized monopole antenna utilizing inductive coupling and capacitive loading was reported. In this approach, significant size reduction ($\lambda_0/45$ X $\lambda_0/16$ X $\lambda_0/8$) is reported while polarization purity and high gain are maintained.

Recently, an antenna miniaturization technique using chip inductors has been investigated [23], [52]-[54]. In [53] and [54], the chip inductors are embedded into the printed monopole antennas to decrease the size of the antennas at the expense of gain and bandwidth. To make the size of the antennas small enough for portable wireless devices, extreme miniaturization must be attempted when the typical size of the antennas is comparable to or smaller than $\lambda_0/100$. At these small dimensions, all antenna components act as lumped elements. Utilization of chip inductors and capacitors with poor quality factor for the antenna structure lowers radiation efficiency.

In this work, a novel design for extremely small HF monopole antennas is presented. The proposed antenna utilizes two short vertical elements producing in-phase radiated fields. In this way, the effective height of the short dipole is increased without

29

physically increasing the height. This leads to enhanced gain compared to a short monopole with the same height [55]. In order to achieve the in-phase radiated fields from electric currents flowing on the two vertical elements, a novel antenna topology using a modified T-type 180 degree phase shifter is introduced. It is shown that increasing the quality factor (Q) of the inductors used in the phase shifter can lead to significant gain enhancement. For example, it is shown that optimized air-core inductors can improve the gain by a factor of 14 (=11.3dB) compared to a commercial chip inductor. The basic idea is presented in Section 2.2.2. Design, implementation and performance assessment of the proposed HF antenna using chip inductors are presented in Section 2.2.3. In Section 2.2.4, we discuss gain enhancement using optimized air-core inductors and the approach for incorporating such inductors within the antenna volume. In Section 2.2.5, the proximity effect of objects on the resonant frequency of the proposed antenna with narrow bandwidth is investigated.

2.2.2 Realization of Two In-Phase Radiating Vertical Elements Using a Modified T-Type 180 Degree Phase Shifter

Let us imagine a short-circuited $\lambda_0/2$ transmission line (TRL) resonator connected to two shorting pins at both ends. Large electric currents on the two shorting pins can radiate vertically polarized fields that are in phase. Fig. 2.15(a) shows two vertical elements (pins) connected by a $\lambda_0/2$ TRL. Radiated fields from the electric currents flowing on the two vertical pins are in phase because of the 180 degree phase shift from the $\lambda_0/2$ TRL. The corresponding circuit model is shown in Fig. 2.15 (b), assuming that small inductances from the two vertical pins with very low profile ($<<\lambda_0/100$) can be ignored. The black arrow depicts the reference direction of the electric current at each

probing position. To reduce the long lateral dimension of the $\lambda_0/2$ TRL, using a meandered metallic trace causes high ohmic loss, and increases x-polarized radiated fields [17]. Therefore, the proposed antenna is designed to achieve the electric currents that can radiate in-phase using an alternative approach.

Instead of using the $\lambda_0/2$ TRL, a T-type 180 degree phase shifter with a capacitive impedance inverter can be used [55]. Fig. 2.15(c) shows the circuit model and the reference directions of electric currents on the vertical elements. Fig. 2.16 shows the magnitude and phase of I_1, I_2, I_3, I_4 and I_5 which are highlighted in Fig. 2.15. As expected, at 23MHz I_1 and I_2 have the same magnitude but 180 degree phase difference. This corresponds to in-phase radiation from the vertical elements. However, Fig. 2.16(d) shows that the current in the capacitor branch flows in the opposite direction of the currents in the feed and shorting pins. The magnitude (0.08A at 23MHz) of I_4 is twice that (0.04A at 23MHz) of I_3 or I_5 as shown in Fig. 2.16(c). Hence, the radiated fields from I_4 cancel out the radiated fields from I_3 and I_5. To avoid this radiation cancellation, it is important to eliminate the conduction current path I_4, while maintaining the 180 degree phase shift for I_5.
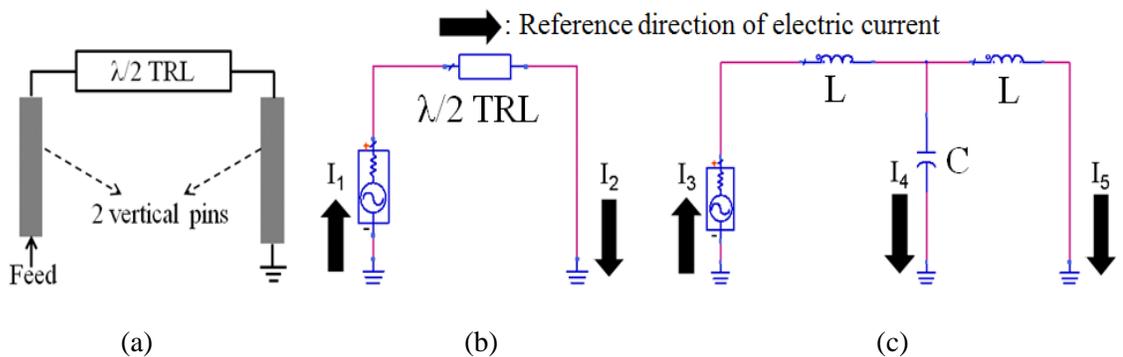
Figure 2.15: (a) Two vertical elements put $\lambda_0/2$ away from each other, (b) its circuit model and (c) a circuit model for the conventional T-type 180 degree phase shifter.
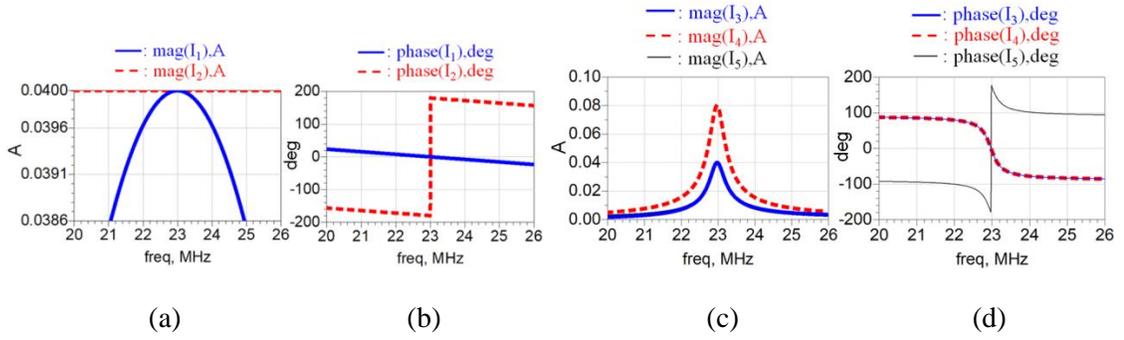
Figure 2.16: (a) Magnitudes and (b) phases of I_1 and I_2, and (c) magnitudes and (d) phases of I_3, I_4 and I_5 shown in Fig. 2.15.

(a)

(b)
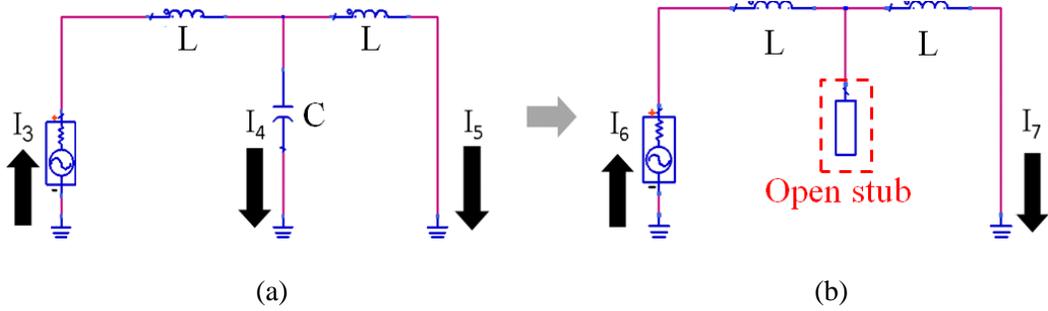
Figure 2.17: (a) Circuit model for a T-type 180 degree phase shifter and (b) circuit model employing an open stub instead of a grounded capacitor in (a).

(a)

(b)
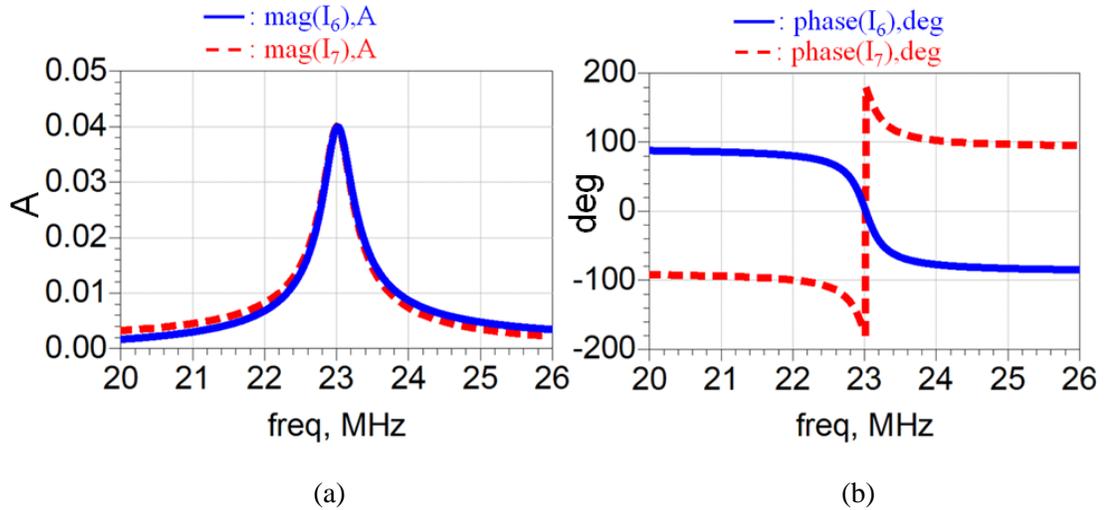
Figure 2.18: (a) Magnitudes and (b) phases of I_6 and I_7 shown in Fig. 2.17.

The conduction current I_4 can be eliminated altogether by replacing the lumped capacitor with an open-stub as shown in Fig. 2.17(b). Characteristic impedance and length of the open stub in the circuit schematic are appropriately chosen to achieve the required 180 degree phase shift at 23MHz. Fig. 2.18 shows the magnitudes and phases of I_6 and I_7, indicating the same magnitude and 180 degree phase difference for achieving efficient vertically polarized radiation.

2.2.3 Extremely Small Two-Element Monopole Antenna Configuration

2.2.3.1 Antenna Design

Based on the equivalent circuit model shown in Fig. 2.17(b), an extremely low-profile miniaturized HF antenna with two in-phase radiating vertical elements is designed. Fig. 2.19 shows the side view and the top view of the proposed antenna. The lateral dimension and height of the proposed antenna including the ground plane are 150mm $(0.0115\lambda_0)$ and 50mm $(0.0038\lambda_0)$, respectively. The top metallic plate acts as the open stub (capacitor of the phase shifter) connected between the two chip inductors (8μH) which are connected to the vertical pins. The substrate used in this design is air, allowing elimination of dielectric loss from the antenna structure. In order to include ohmic loss in the simulation, the finite conductivity of copper is used in all metallic traces and the two vertical pins. In order to consider actual characteristics of the chip inductors, equivalent series resistance (ESR) of 28ohm is extracted at 23MHz from the datasheet provided by the manufacturer [56]. The ESR is included in the simulation for calculation of antenna input impedance and radiation efficiency. By optimizing the distance between the shorting pin and the feeding pin appropriately, impedance matching to a 50ohm feed is

obtained. The geometry of the open stub on the top plate is chosen to be symmetric in terms of xz and yz planes and the positions of the two pins are chosen near the center of antenna structure to obtain omnidirectional radiation pattern.

Fig. 2.20(a) shows the simulated S_{11} of the proposed antenna with the center frequency of 23.2MHz. It should be noted that using a coaxial feed cable to measure S_{11} of the monopole antennas having a very small ground plane ($0.0115\lambda_0$ X $0.0115\lambda_0$) produces incorrect results. This is due to the strong near-field coupling between the antenna and outer conductor of the coaxial cable. The excited induced currents over the cable produce changes in radiation pattern and S_{11} [17]. To avoid this measurement problem, a small source module can be connected to the antenna feed. Fig. 2.21 shows the fabricated antenna integrated with the small source module consisting of a Voltage Controlled Oscillator (VCO), potentiometer and a 12V battery. By controlling the potentiometer, the bias voltage of the VCO can be changed, enabling frequency tuning. By observing the variation of received power versus frequency, the operating (resonant) frequency of the antenna is found. This is done using the proposed antenna with chip inductors as a transmitting antenna and using a $\lambda_0/10$ dipole antenna with a wider bandwidth as a receiving antenna. Fig. 2.20(b) shows the setup used to measure the received power and the radiation patterns of the proposed antenna. The transmitting antenna (the proposed antenna) is mounted on a positioner, and the receiving antenna ($\lambda_0/10$ dipole antenna) is mounted in an elevated position. By using this elevated range, the measurement error caused by the reflected waves from the ground can be decreased substantially. In order to calculate the measured gain of the proposed antenna, $\lambda_0/10$ dipole antennas are used, as reference antennas.

As mentioned earlier, S_{11} of the proposed antenna cannot be measured directly by a network analyzer due to the near-field coupling. However, it can be indirectly evaluated by comparing the slope and the center frequency of the measured received power versus frequency to those of the simulated response. Fig. 2.22 shows measured and simulated power received by the $\lambda_0/10$ dipole antenna in an elevated range versus frequency. The power is normalized by the peak value of each plot for a better slope comparison between the measured and simulated plots. It is shown that the slope of the measured plot is similar to that of the simulated plot, indicating that S_{11} of the fabricated antenna is well matched to the simulated S_{11}. Measured resonant frequency is 22.9MHz which is slightly shifted from the simulated resonant frequency of 23.2MHz due to the 5% tolerance range of the commercial chip inductors. Based on simulated S_{11}, 10-dB return loss bandwidth of 0.86% is derived at 23.2MHz. Fig. 2.23 shows measured and simulated radiation patterns in the E (yz) plane and H (xy) plane. Omnidirectional radiation patterns are observed. The measured antenna gain is -29.2dBi, which is similar to the simulated gain of -28.1dBi.

(a) (b)
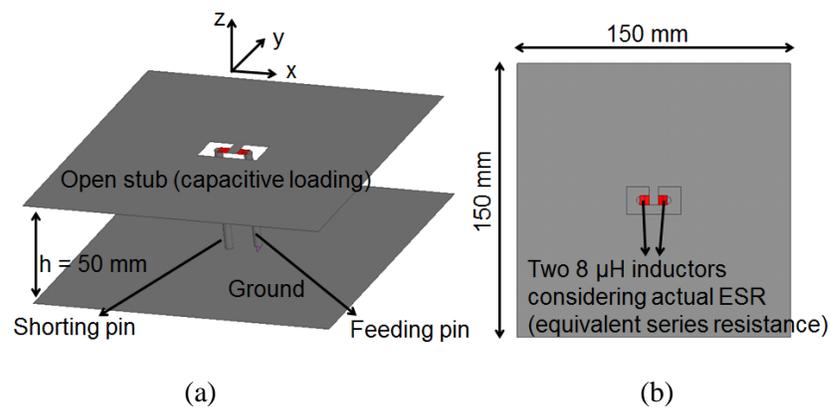
Figure 2.19: (a) Side view and (b) top view of the proposed antenna with chip inductors.

(a)   (b)
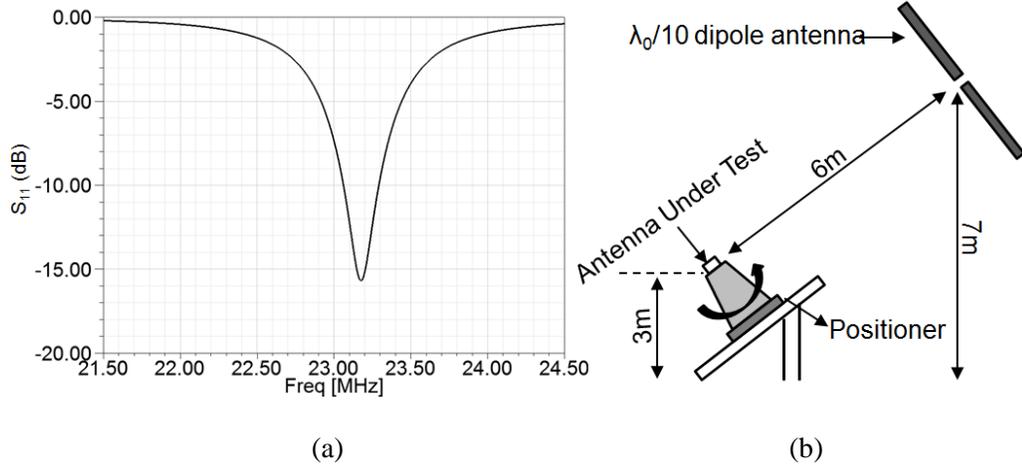
Figure 2.20: (a) Simulated S_{11} of the proposed antenna with chip inductors and (b) measurement setup in an elevated antenna range.
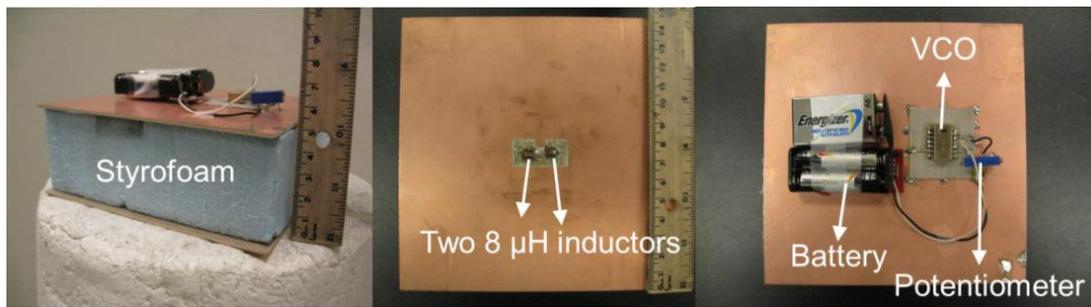
Figure 2.21: Fabricated antenna with chip inductors, integrated with the source module.

Figure 2.22: Measured and simulated power received at the reference $\lambda_0/10$ dipole antenna and normalized by the peak value of each response versus frequency when the proposed antenna with chip inductors is used as a transmitting antenna.

36

Figure 2.23: Measured and simulated radiation patterns of the proposed antenna with chip inductors in the (a) E (=yz) plane and (b) H (=xy) plane.

2.2.3.2 Gain and Mass Comparison

To examine a figure of merit of the proposed antenna, its gain and mass are compared with those of a conventional inverted-F antenna having the same dimensions and volume. A small inverted-F antenna can be fabricated using a $\lambda_0/4$ open-ended transmission line on a high index substrate material. The free space wavelength (λ_0) at 22.9MHz is 13.1m and thus $\lambda_0/4$ is 3.275m. Fitting a $\lambda_0/4$ inverted-F antenna on very small area of 150mm X 150mm ($0.0115\lambda_0$ X $0.0115\lambda_0$) is not practical. Thus, the use of a substrate with high dielectric constant (ε_r=10.2 and tan δ=0.002) is necessary. A spiral geometry is used to accommodate the quarter-wave transmission line as shown in Fig. 2.24. Fig. 2.25 shows the simulated S_{11} of the spiral-shaped inverted-F antenna, compared to that of the proposed two-element short monopole antenna. It is found that 10-dB return loss bandwidth of the spiral-shaped IFA is much narrower than that of the

proposed antenna due to the highly stored electric energy in the high dielectric substrate. Fig. 2.26 shows the simulated radiation patterns in the E-plane and H-plane of the spiral-shaped IFA. The gain of the spiral-shaped IFA is calculated as -34.4dBi which is 5.2dB lower than the measured gain of the proposed antenna. This is due to the ohmic loss in the spiral trace and dielectric losses, despite a very good dielectric loss tangent (tan δ=0.002). This result suggests that the parasitic losses from the two chip inductors in the proposed antenna are much lower than the ohmic and dielectric losses in the spiral-shaped IFA. It is also found that the proposed two-element short monopole antenna provides wider bandwidth than the spiral-shaped IFA.

Another advantage of the proposed two-element short monopole antenna over the IFA is its much lower mass. The substrate materials with high dielectric-constant usually have high mass density which makes the antenna that uses such substrates heavy. The proposed antenna provides miniaturization without the need for high index materials and thus it can be made very light. Table 2.3 shows the masses of all the materials used to fabricate the spiral-shaped IFA with a substrate having ε_r=10.2 and the proposed antenna with air substrate. The total mass of the conventional inverted-F antenna (3502g) is about 220 times heavier than that of the proposed antenna (15.8g). Fig. 2.27 shows the proposed antenna fabricated using flexible thin substrates.
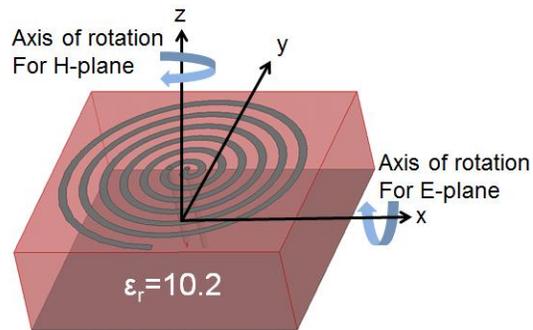
Figure 2.24: Spiral-shaped inverted-F antenna on the substrate with ε_r =10.2.
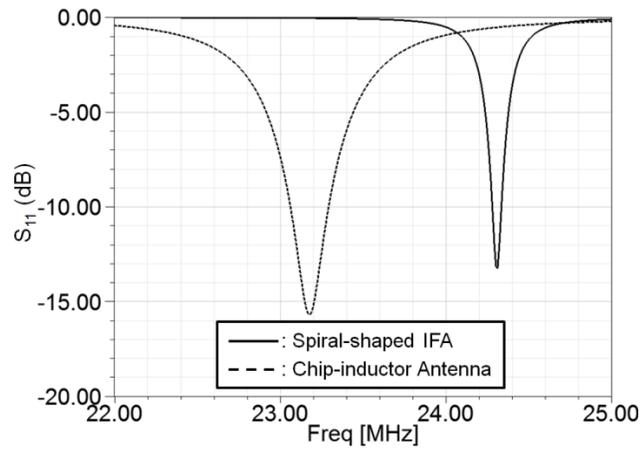
Figure 2.25: Simulated S_{11} of spiral-shaped inverted-F antenna on the substrate with $\varepsilon_r =10.2$, compared to that of the proposed antenna with chip inductors.

(a)   (b)
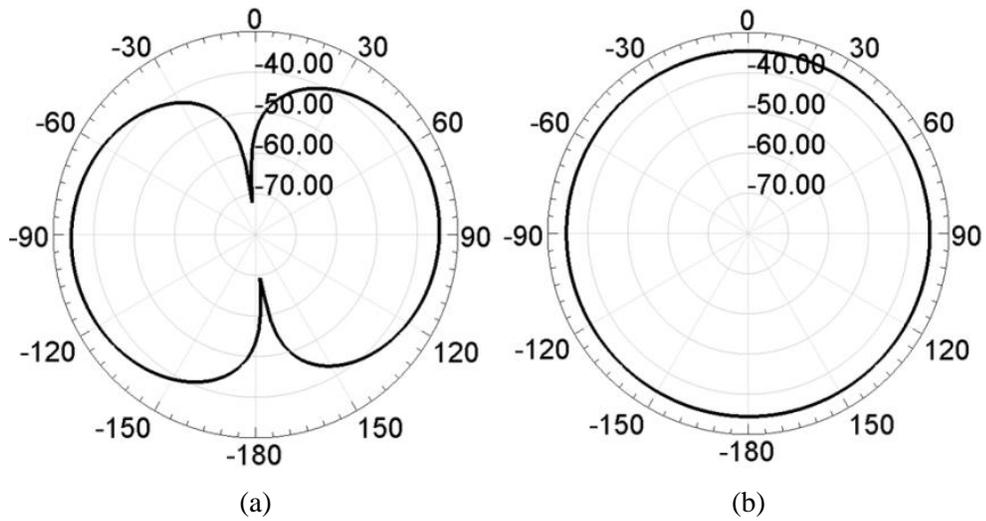
Figure 2.26: Simulated radiation patterns of spiral-shaped inverted-F antenna on the substrate with $\varepsilon_r =10.2$ in the (a) E (=yz) plane and (b) H (=xy) plane.
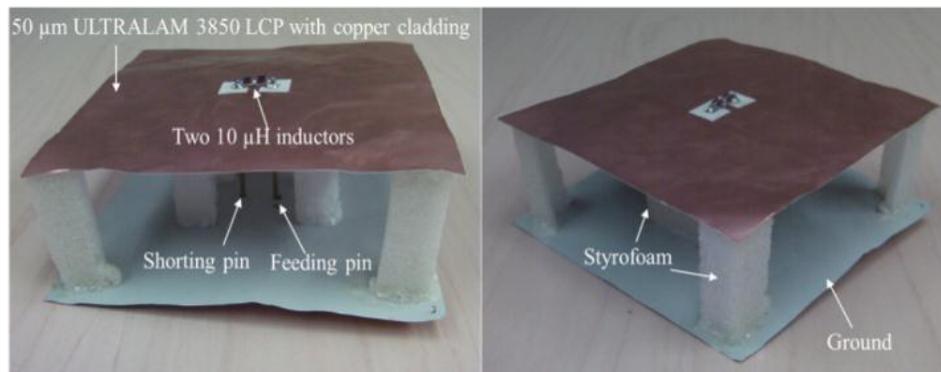
Figure 2.27: Proposed antenna fabricated using flexible thin substrates.

TABLE 2.3

MASS OF EACH PART OF THE PROPOSED ANTENNA WITH AIR SUBSTRATE AND
THE SPIRAL-SHAPED INVERTED-F ANTENNA ON THE SUBSTRATE WITH ε_r=10.2

Inverted-F antenna (g) on the substrate (ε_r=10.2)		The proposed antenna (g)	
One 50mm RO6010	3501	Two 50um ULTRALAM 3850 LCP	13.293
		Styrofoam to support a top-plate	0.352
Two inductors	0.1	Two inductors	0.1
One copper post	1.4	Two copper posts	2.02
Total mass (g)	3502	15.8	

2.2.4 Gain Enhancement Using Optimized Air-Core Inductors

As discussed in Section 2.2.3.2, the proposed two-element antenna provides higher gain than the conventional spiral-shaped IFA. This section shows that further gain enhancement can be achieved by increasing the Q of the inductors used in the phase shifter. This is possible because Q of the commercial chip inductor is rather low (Q=45). Fig. 2.28 shows simulated gain of the proposed antenna versus Q of the inductors. It indicates that increasing Q of the chip inductors from 45 to 450 can lead to gain enhancement of about 10dB. The relationship between the gain and Q of the inductors is almost linear up to about Q 104. Beyond the value, radiation resistance in the proposed antenna dominates over losses on the metallic surfaces. The gain will saturate to the gain of the ideal short dipole (1.76dBi) if one were to ignore metallic losses.

It is reported that Q of air-core inductors can be as high as several hundred at HF band due to the absence of the ferrite core loss [57]-[61]. In this section, design and performance of an extremely small two-element monopole antenna using air-core inductors are discussed. Since air-core coils have lower inductance values than the

ferromagnetic core coils, the size of the inductors must be increased. Therefore, the most important design issue determining antenna gain is to optimize Q of air-core inductors restricted by the size of the antenna.
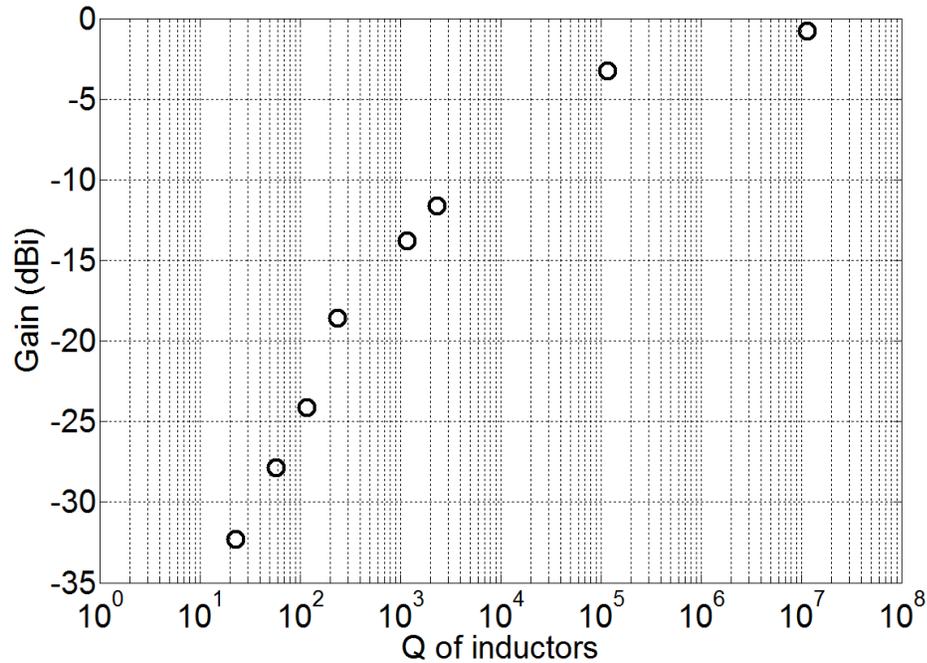
Figure 2.28: Simulated gains of the proposed antennas with chip inductors versus Q of the chip inductors.

2.2.4.1 Optimization of Quality Factor of Air-Core Inductors

The Q of an air-core inductor is determined by two loss mechanisms related to proximity effect and skin effect. The proximity effect refers to the concentration of electric currents on a small portion of wires due to the proximity of the adjacent wires in the inductor coil. This proximity effect can significantly increase AC resistance of adjacent conductors when compared to its DC resistance. The adverse proximity effect on the AC resistance increases with frequency. At higher frequencies, the AC resistance of a conductor can easily exceed ten times its DC resistance [62]. Recently, methods for accurate prediction of inductance and AC resistance of coils at high frequencies have been reported [63]-[64]. In [63], the coil is analytically modeled as a slow-wave anisotropic

waveguide and analytic formulas to determine the inductance and AC resistance are presented. The formulas are corrected based on experimental data as presented in [64]-[65]. Fig. 2.29 shows design parameters of the coil, and (2.1) and (2.2) are the analytic formulas including the correction factor derived from experimental data to calculate the inductance and AC resistance.
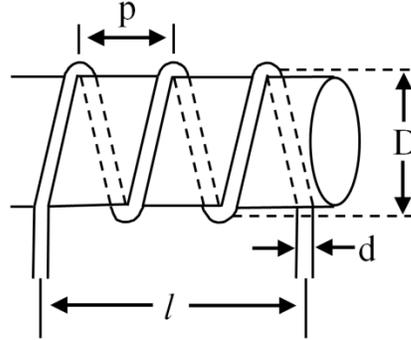
Figure 2.29: Design parameters of the air-core coil.

Based on the literatures, the inductance is given by

$$L=(\mu_0\pi D^2 N^2 k_L/4l)-[\mu_0 DN(k_{s(e)}+k_m)/2]+L_i \qquad (2.1)$$

where D is the effective current-sheet diameter, N is the number of turns, l is the coil length, L_i is the internal inductance, k_L is Nagaoka's coefficient, k_m is Rosa's mutual-inductance correction term presented in [64], and $k_{s(e)} = (3/2)-\ln(2p/d)$ where d is the diameter of the wire and p is the winding pitch-distance

The AC resistance is given by

$$R_{AC}=R_{DC}[1+ (\Omega-1) \psi(N-1+1/ \psi)/N] \qquad (2.2)$$

where R_{DC} is DC resistance, ψ is proximity factor (derived by the interpolation of Medhurst's table of experimental data [65]) and $\Omega = d^2/[4(d\delta_i - \delta_i^2)]$ where δi=skin depth.

Based on (2.1) and (2.2), dimension parameters of an air-core solenoid with inductance of 8µH are optimized considering the constrained antenna volume of 150mm X 150mm X 50mm. In order not to increase vertical profile of the antenna, the coil is placed between the ground plane and the top plate, which limits the diameter of the coil to be strictly smaller than 50mm. In the proposed antenna, 25mm is chosen for the coil diameter in order not to drastically increase the top plate capacitance. With the fixed coil diameter (D), the effects of coil length (*l*) and wire diameter (d) on Q are investigated. Once the values of D and *l* (or d) are chosen and fixed, the values of other parameters such as the number of turns (N) and the winding pitch-distance (p) are accordingly determined to achieve the required inductance of 8µH. Fig. 2.30(a) shows the calculated Q versus *l* where d is 1mm. This figure suggests that increasing *l* after about *l*=60mm doesn't affect Q of the inductor. This is due to the fact that the proximity effect vanishes once wires are far from each other (large p). 70mm is chosen as the optimum value of *l*. With the chosen *l*=70mm, the effect of d is iteratively examined. Fig. 2.30(b) shows Q versus d where *l* is 70mm. The figure suggests that increasing d beyond d=1mm, the Q of the inductors decreases because p decreases with fixed *l*, leading to the increase in the proximity effect. Finally, the values of D, N, *l*, d and p are chosen as 25mm, 32, 70mm, 1mm and 2.3mm, respectively, resulting in a quality factor of about 730.

<div align="center">(a)</div>

<div align="center">(b)</div>
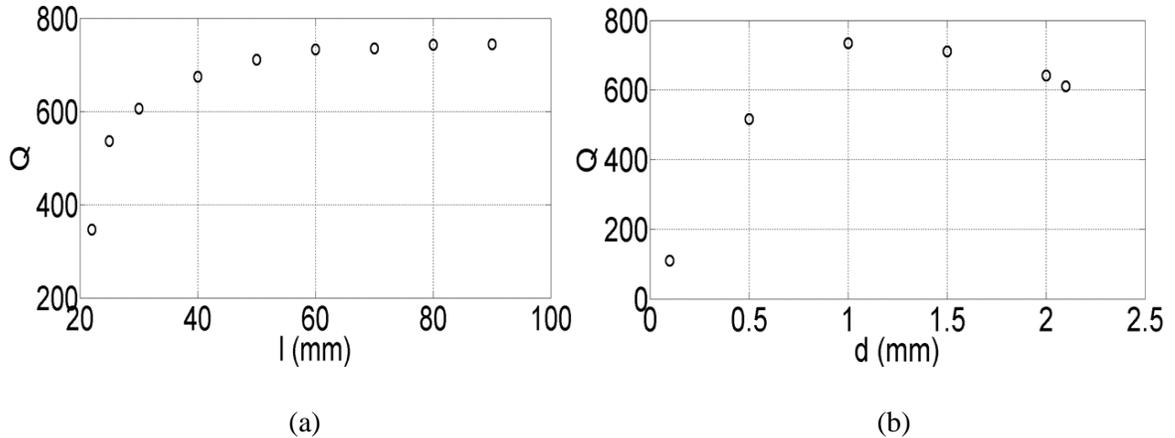
Figure 2.30: Calculated Q versus (a) l (=coil length) where d = 1 mm, and (b) d (=wire diameter) where l = 70mm.

2.2.4.2 Antenna Design

The air-core solenoids designed in the previous section are used to design an extremely small two-element monopole antenna. Fig. 2.31 shows the geometry of the proposed antenna with the same dimensions as the previous antenna where chip inductors were used. As mentioned earlier, the solenoids are integrated underneath the capacitive loading plate not to increase the overall vertical profile of the antenna. The copper layer over the area where the solenoids are positioned is removed to reduce the effect of the top metallic plate on the inductance and the effect of the solenoids on the top plate capacitance. An additional shorting pin with a chip inductor of 40nH is used to get impedance matching to a 50Ohm feed. Fig. 2.32 shows the side and bottom view of the fabricated antenna integrated with the source module.

Fig. 2.33 shows the simulated S_{11} of the antenna with air-core inductors, compared to that of the antenna with chip inductors. As expected, the bandwidth of the antenna with air-core inductors (10-dB return loss bandwidth of 0.13% at 22.1MHz.) is narrower than that of the antenna with chip inductors due to very high Q ($\approx$730) of the air-core inductors. As discussed in Section 2.2.3.1, S_{11} of the proposed antenna cannot be

measured directly by a network analyzer due to the aforementioned near-field coupling. As before, the center frequency and the bandwidth are characterized through transmission measurement. Fig. 2.34 shows the measured and simulated power received at the reference $\lambda_0/10$ antenna as a function of frequency. The power is normalized by the peak value of each response to compare the different plots. It is shown that the slope of the measured response of the antenna with air-core inductors is much steeper than that of the antenna with chip inductors, showing good agreement with the simulated plot. Measured resonant frequency is 22.9MHz which is slightly different from the simulated resonant frequency of 22.1MHz due to the interaction between the solenoids and other metallic parts. Fig. 2.35 shows the measured and simulated radiation patterns in the E (=yz) plane and H (=xy) plane. Omnidirectional radiation patterns are observed and measured antenna gain is found to be -17.9dBi. This is 11.3dB and 16.5dB higher than that of the antenna with chip inductors and the spiral-shaped IFA, respectively. The total mass of the antenna with two air-core solenoids made of copper is 51.95g.
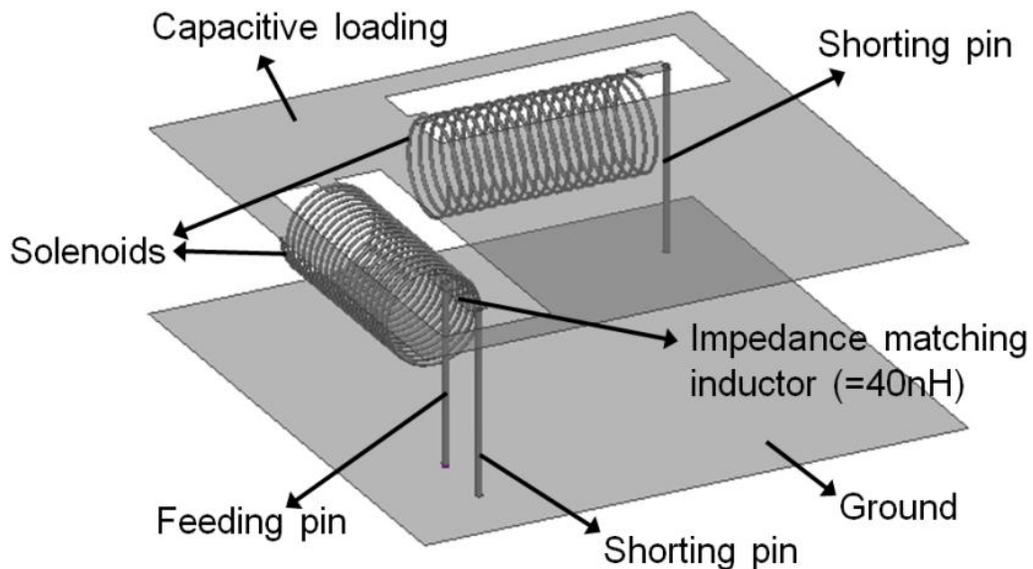
Figure 2.31: Geometry of the proposed antenna with air-core inductors having the dimensions of 150mm X 150mm X 50mm.

(a)   (b)
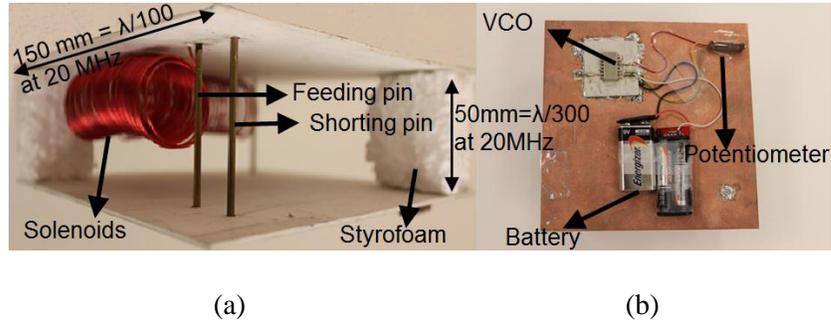
Figure 2.32: (a) Side view and (b) bottom view of the fabricated antenna incorporating air-core inductors, integrated with the source module.
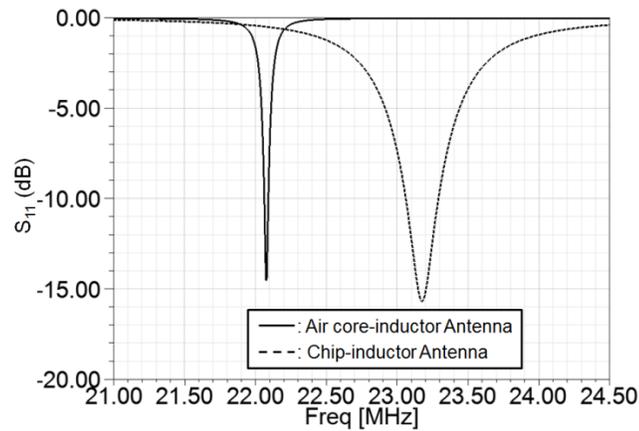
Figure 2.33: Simulated S_{11} of the proposed antenna with air-core inductors, compared to that of the antenna with chip inductors. Narrower bandwidth indicates higher radiation efficiency because the antenna volume is fixed.
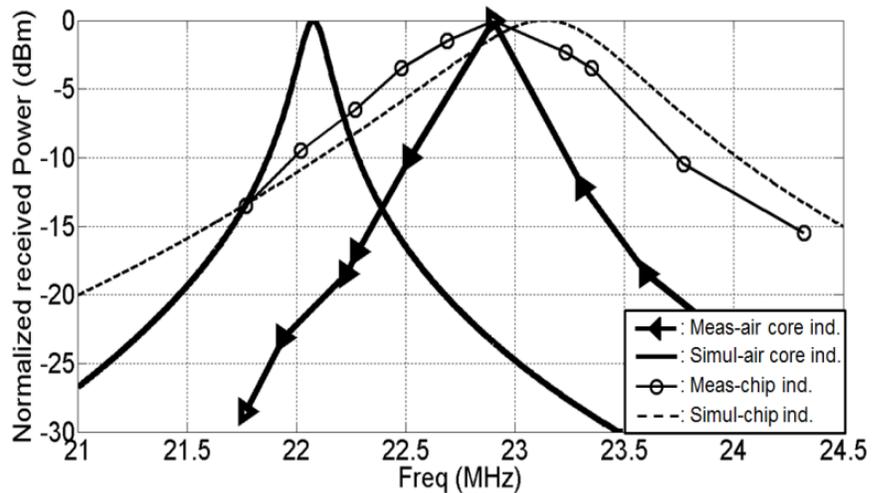
Figure 2.34: Measured and simulated power received at the reference $\lambda_0/10$ antenna and normalized by the peak value of each response versus frequency when the proposed antenna with air-core inductors is used as a transmitting antenna, compared to those of the antenna with chip inductors.

46

(a)   (b)

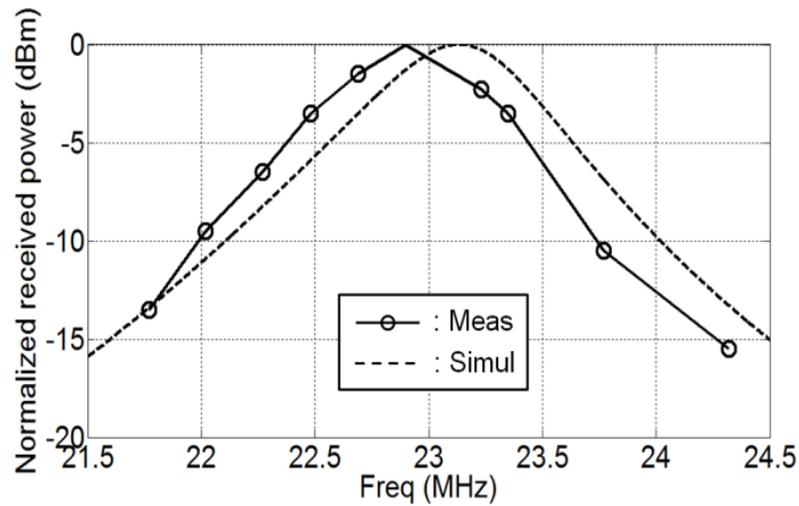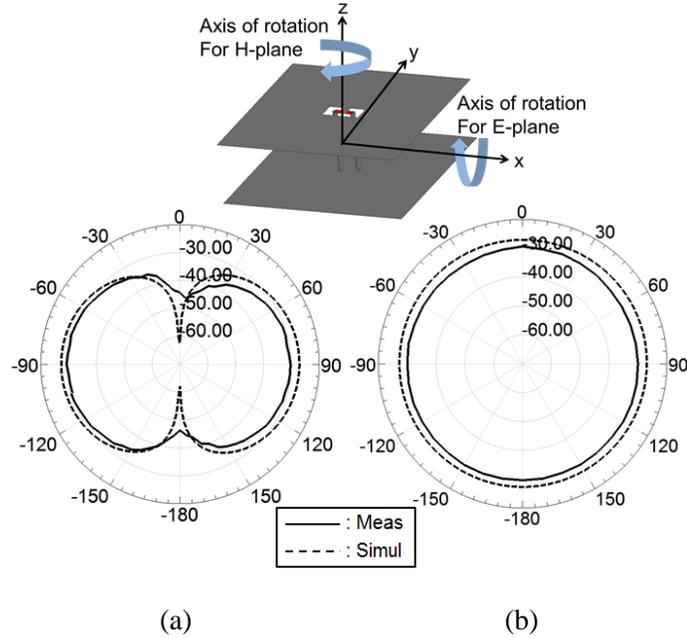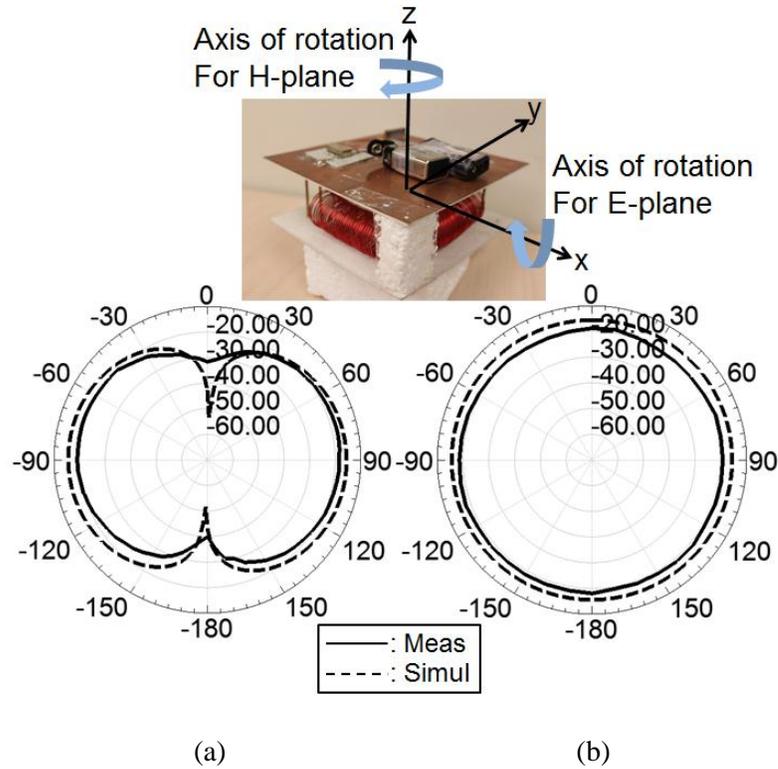Figure 2.35: Measured and simulated radiation patterns of the proposed antenna with air-core inductors in the (a) E (=yz) plane and (b) H (=xy) plane.

Since the sizes of the antennas under discussion are electrically very small, it is interesting to compare the performance of the antennas to the fundamental limit derived by [66]. To do that, a figure of merit is used, defined as the product of the 3-dB return loss bandwidth (BW) and radiation efficiency (η). Fig. 2.36 shows the figures of merit corresponding to the antennas, electrical small antennas in literature and the fundamental limit. The 3-dB return loss bandwidth (BW) of the fundamental limit is calculated using BW=1/Q where Q$\approx$1/(kr)^3 where k is the wave number and r is the radius of the smallest sphere that can enclose the antenna. The results suggest that although the bandwidth of the antenna with air-core inductors is narrower than those of the antenna with chip inductors and the spiral-shaped IFA, because the radiation efficiency of the antenna with air-core inductors is tens of times higher than those of others, the figure of merit of the antenna with air-core inductors gets much closer to the fundamental limit than the other

antennas. With this analysis, it is successfully validated that the proposed electrically small antenna provides significantly enhanced performance, compared to the conventional IFA.
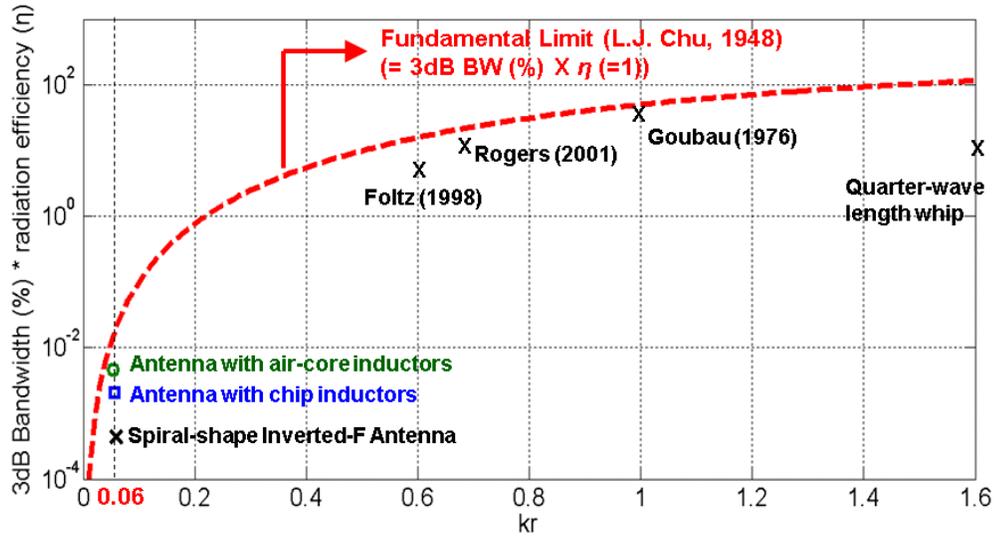
Figure 2.36: Performance comparison among the electrically small antennas shown in this work.

2.2.5 Proximity Effect of Nearby Objects

For very small antennas with narrow bandwidth, there is always a concern about the proximity effect of nearby objects as regards the possible shift in resonant frequency. At HF band where the wavelength is large, typical distances between the small antennas and nearby objects in an indoor environment are very small compared to the wave length. In order to examine the feasibility of using the proposed antennas for such environments, the change in the operating frequency caused by nearby objects is investigated. This is done experimentally by changing the distance between the antenna and a concrete wall, and the ground in an indoor environment. Fig. 2.37 shows the measurement set up. At wall separation distance (s) = 0.5, 1, 1.5 and 2m, and ground height (h) = 0.2m and 1.4m, the power received at the $\lambda_0/10$ dipole antenna is measured and normalized by the peak value of each plot when the proposed antenna with air-core inductors is used as a

transmitting antenna. Fig. 2.38 shows the measurement results, indicating a stable operating frequency of the proposed antenna. The small variation observed is due to frequency jitter of the VCO itself. Also the frequency response of a $\lambda_0/10$ dipole antenna as the transmitting antenna when the same $\lambda_0/10$ dipole antenna is used as the receiving antenna, is shown to indicate that the observed steep frequency response is due to the frequency response of the proposed two-element monopole antenna.
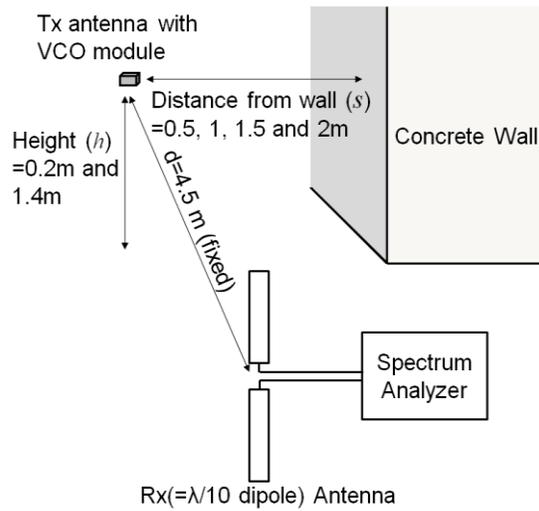
Figure 2.37: Measurement set up for examining the proximity effect of nearby objects on the resonant frequency of the proposed narrow band antenna.
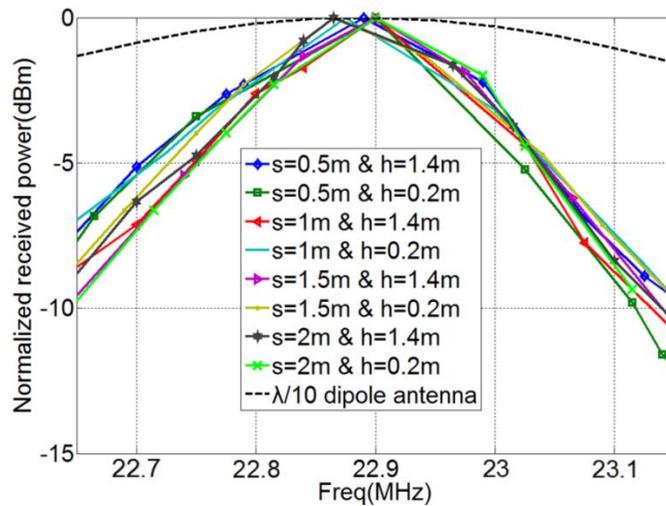
Figure 2.38: Measured received normalized power corresponding to various positions of the transmitting (=proposed) antenna shown in Fig. 2.37.

Chapter 3

Realization of Omnidirectional Radiation Pattern/Broad Bandwidth for Low Profile Antennas on a Small Ground Plane

In this chapter, techniques are presented to realize omnidirectional radiation pattern for low profile antenna on a small ground plane ($<<\lambda$). Based on these techniques, an antenna embedded into small robotic platforms is designed and its performance is discussed. In addition, a broadbanding technique compatible with the miniaturization techniques for realizing omnidirectional radiation pattern is presented.

3.1 Low Profile Balanced-Type Omnidirectional Antennas

3.1.1 Introduction

Recent development in wireless device technologies urges antennas to be integrated with very small ground plane. However, such antennas on the small ground plane ($<< \lambda_0$) suffer from serious distortion in radiation pattern. In this section, we try to propose a design approach for low profile omnidirectional antennas by addressing a problem in characterizing the input impedance and radiation pattern of such antennas with unbalanced feed. For measuring the input impedance using a network analyzer or

the radiation pattern using a spectrum analyzer, a coaxial cable must be connected to the antenna. The problem is that the antenna with the small ground plane is coupled to the coaxial cable over which an electric current can get excited. As a result, both the input impedance and the radiation pattern of the antenna are changed. Fig. 3.1 depicts the electric field distribution around the proposed antenna fed by a coaxial cable. Significant electric current exists on the external layer of the coaxial cable that unexpectedly contributes to radiation. This causes a shift in the resonant frequency, poor impedance matching and radiation pattern. Although omni-directional radiation pattern is expected (see Fig. 3.2(a)), deformed radiation pattern is measured as shown in Fig. 3.2(b). At $\theta=90°$, which is in the azimuthal plane of ICCLMA, the gain drops from 0 dBi to -8 dBi.
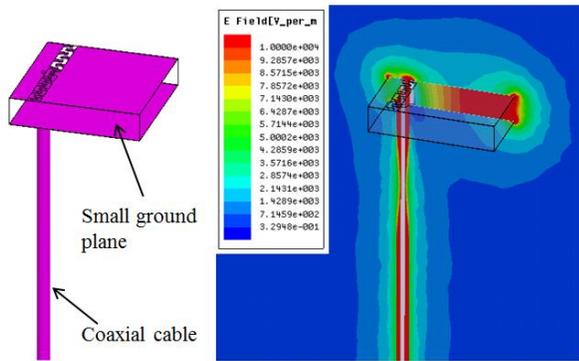
Figure 3.1: Electric field distribution in the proposed antenna fed by coaxial cable.

(a)   (b)
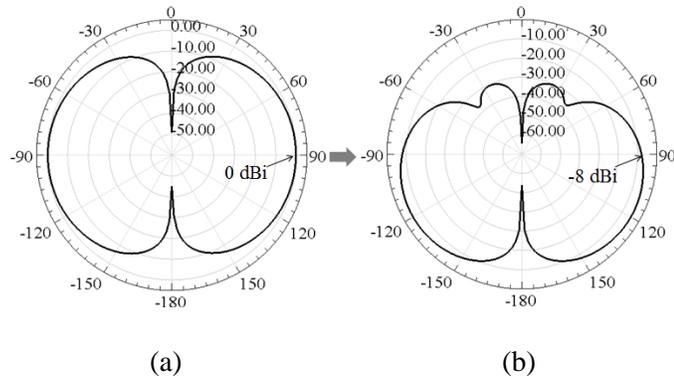
Figure 3.2: Simulated E-Plane radiation pattern of single-layer ICCLMA (a) without and (b) with a coaxial cable.

3.1.2 Balanced Type of ICCLMA

Miniaturized monopole antennas are considered for wireless nodes with small platforms where the back of the antenna ground plane can support the active elements. As described in the previous section, the characterization of small antennas by connecting a long coaxial cable leads to uncertainties in the antenna radiation parameters. One approach is to use large ground planes ($>\lambda_0$ on each side) as was shown in Section 2.1.4, but at low frequencies the size of the ground plane may become prohibitively large. To avoid this problem, an alternative method to measure the input impedance and radiation pattern of electrically small antennas is presented. This can be done using a balanced architecture or simply the dipole version of the monopole antenna (see Fig. 3.3). A balanced architecture produces a null surface in the plane bisecting the dipole structure. In this plane, any metallic structure like the antenna feed can be inserted without affecting the antenna characteristics. The only difficulty is that a balun structure must be used. Although measuring a balanced version of the antenna is not representative of the performance of the antenna on small ground, by redesigning and testing the antenna on small ground as a balanced topology it can be examined whether the simulation results of the antenna previously designed on small ground is trustable or not.

Fig. 3.4 shows a balanced low-profile miniaturized antenna connected to a microstrip balun in the null plane. The standard microstrip tapered balun is connected to two back-to-back ICCLMAs. The vertical dimensions of the antenna and balun set up shown in Fig. 3.4 are given by $h1 = 3.175$mm and $h2 = 0.787$mm. Fig. 3.5 shows the measured and simulated reflection coefficients of a balanced architecture. The simulated fractional 10-dB return loss bandwidth is 0.78%, while that of 8mm X 15mm single

ICCLMA with small ground plane is 0.36%. The simulated and measured gains in Fig. 3.6 are 0.66 dBi and 0.36 dBi, which are higher than that of 8mm X 15mm single ICCLMA with small ground plane. This is not a surprise because the volume of the dipole ICCLMA is twice that of the monopole version. In Fig. 3.6, measured radiation pattern shows good agreement with the simulated results. We also tested the antenna with different length of balun and feed line, and found out that the antenna input impedance and radiation pattern remain unchanged regardless of the length of the feeding lines. Therefore, placing active components with differential (=balanced) outputs in the null plane, this balanced architecture can be used for small RF platforms requiring purely vertically polarized radiation.
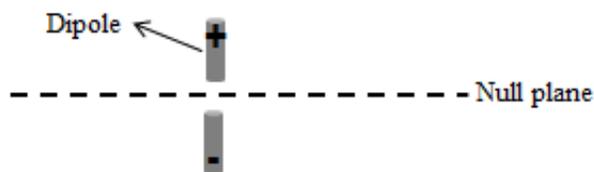
Figure 3.3: Measurement method using a balanced architecture.
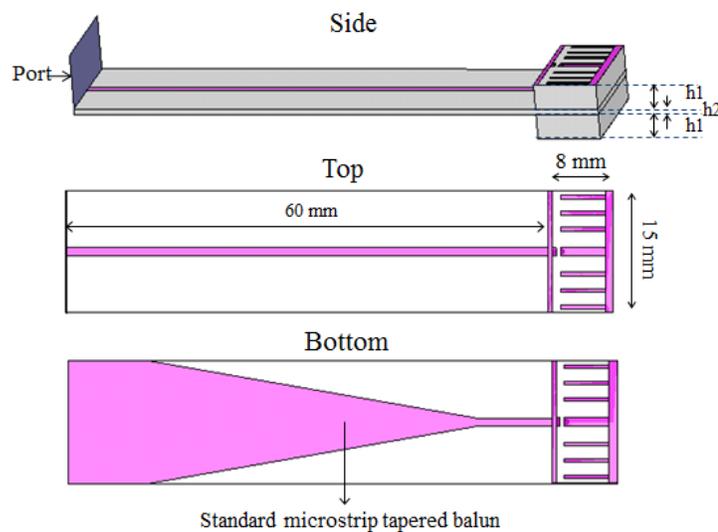
Figure 3.4: Side, top and bottom views of measurement set up of a balanced miniaturized antenna compatible with unbalanced measurement system.
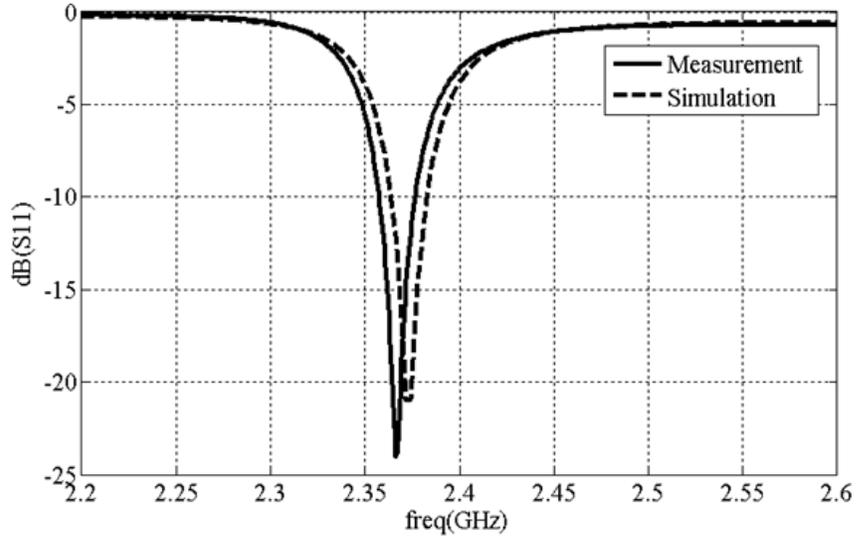
Figure 3.5: Measured and simulated S_{11} of the proposed balanced architecture.

(a)   (b)
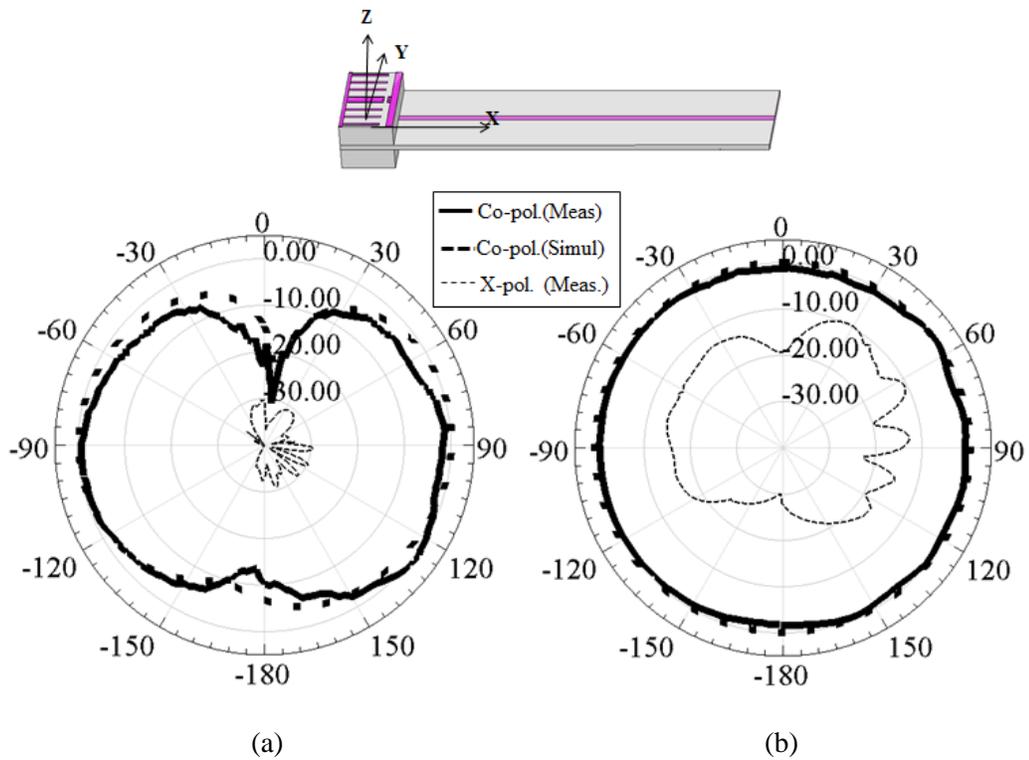
Figure 3.6: Measured and simulated (a) E-Plane (=XZ-Plane) and (b) H-Plane (=XY-Plane) radiation patterns of the proposed balanced architecture.

3.1.3 Application of Low Profile Balanced-Type Antenna

In this section, a low Profile balanced-type vertically polarized omnidirectional antenna structurally embedded into a compact crawling spy robot is presented. There are

54

mainly three challenging objectives in designing this type of antenna. The first objective is to get high gain for vertical polarization from a low-profile configuration. Fig. 3.7(a) depicts the layouts corresponding to top, middle and bottom layers of a crawler. As shown in Fig. 3.7(b), the space of 19mm X 19mm is considered for a vertically polarized antenna. Fig. 3.8 shows how embedded antenna is integrated with Bluetooth module. It says that the available height to be able to contribute to vertically polarized radiation is just 8mm, which is $\lambda/16$. The second objective is to design an antenna structure to be able to compensate distorted and limited ground plane near the radiator generated by bending a paper, which result in low gain related to vertically polarized radiation.

Top   Middle   Bottom

Space for an antenna : 19mm X 19mm

(a)   (b)
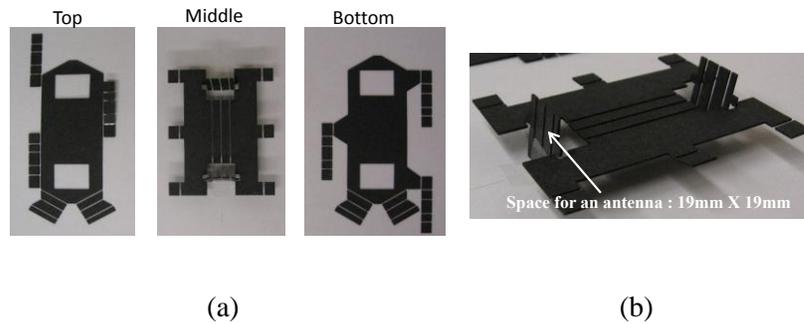
Figure 3.7: (a) Layout of Crawling Robot and (b) location and space for antenna.
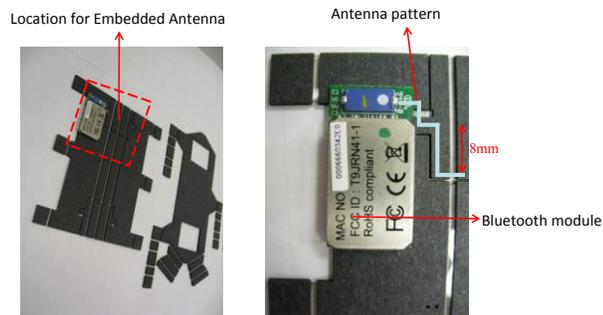
Figure 3.8: Integration of an embedded antenna with Bluetooth module.

The third objective is to suppress the radiation from the extended feeding line connected to Bluetooth module as shown in Fig. 3.8.

One can design ordinary meandered monopole antenna similar to an antenna used in cell phone, as shown Fig. 3.9(a). However, it turns out that this antenna has very poor gain of -7.8 dB near ground at θ=90° as shown in Fig. 3.9(b). It explains why antenna design based on given limitations is challenge.

(a)   (b)   (c)
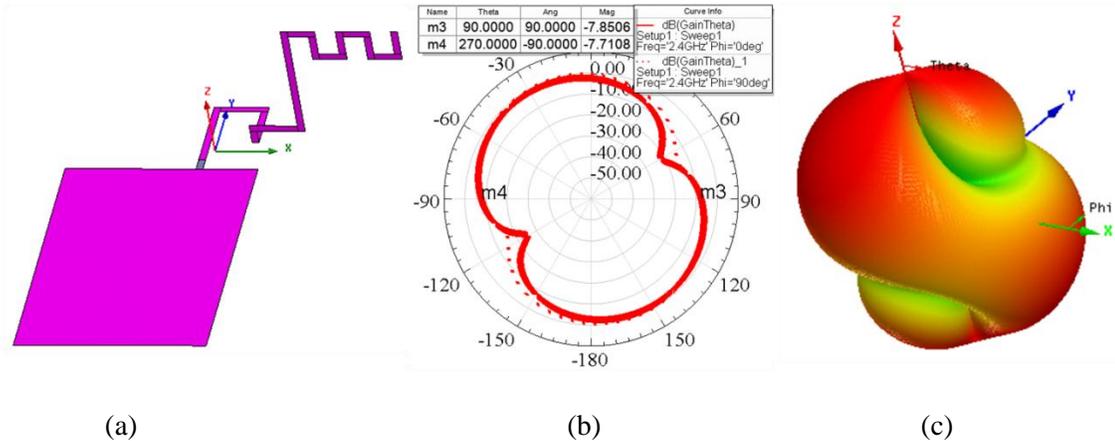
Figure 3.9: (a) Meandered monopole antenna, (b) 2D and (c) 3D radiation pattern of v-pol.

The idea to suppress the radiation from horizontal current on the extended feeding line is to make it ideal transmission line by putting extended ground near feeding line. As shown in Fig. 3.10, it can be achieved by choosing the gap distance between the feeding line and extended ground. Moreover, a balanced structure is designed to achieve omnidirectional radiation pattern related to vertical polarization. It should be noted that ideal omnidirectional pattern enable to maximize the gain of vertical polarization at θ=90°.
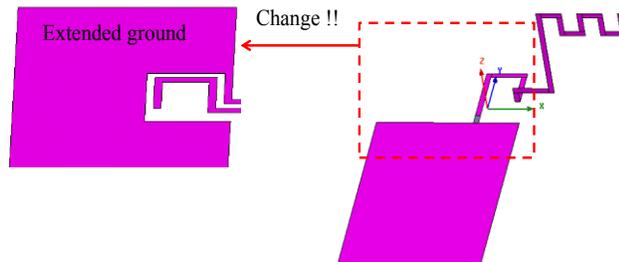
Figure 3.10: Suppression of radiation from horizontal current using extended ground.

Fig. 3.11 shows the geometry of the proposed antenna and its surface current distribution. A balanced structure contributes to symmetry radiation pattern of vertical polarization. Furthermore, Instead of a λ/4 resonator, the design of a λ/2 resonator generates in-phase two radiating elements for vertical polarization, as shown in Fig. 3.11(b). Fig. 3.12 shows 2D and 3D radiation patterns of the proposed antenna, showing desirable ideal omnidirectional pattern. The gain of v-pol at θ=90° is improved to 0.12 dB which is about 8dB higher than the gain of ordinary meandered monopole antenna.

(a)   (b)
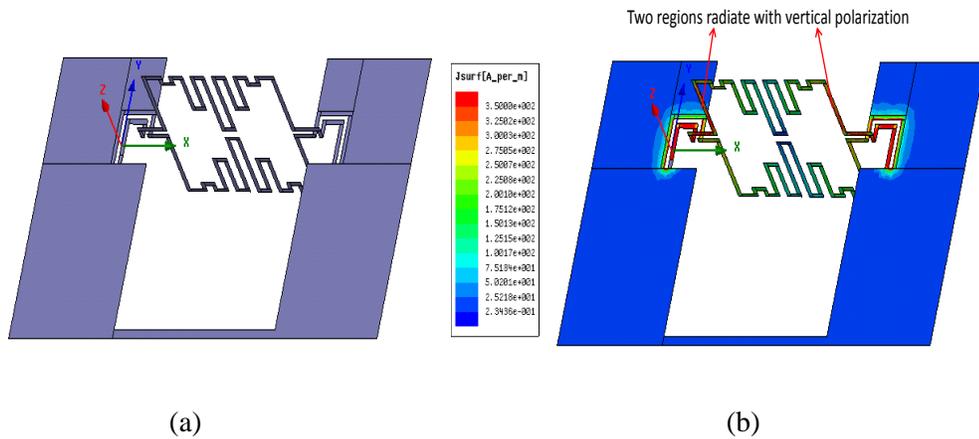
Figure 3.11: (a) The proposed antenna and (b) its surface current distribution.
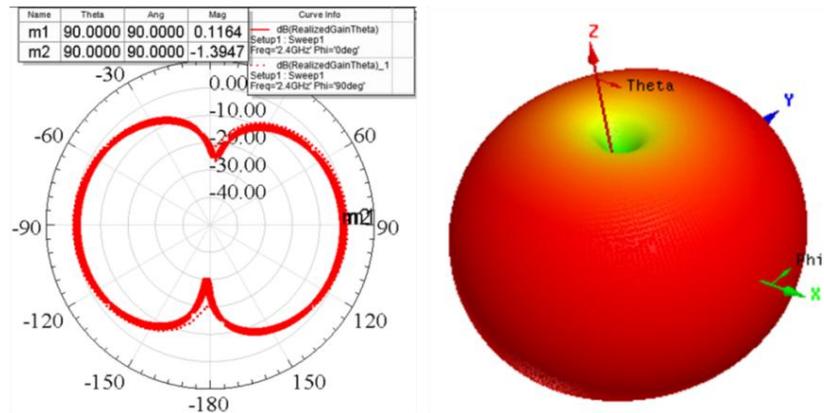
Figure 3.12: 2D and 3D radiation patterns of the proposed antenna.

It is required to consider the dielectric constant of paper in which the proposed antenna is embedded. Since dielectric constant is 1.8, the resonant frequency of antenna

structure in Fig. 3.11 is changed a little bit, thus the resonant length is reduced in order to maintain desirable resonant frequency, 2.4GHz. Fig. 3.13 shows simulation model and results of embedded antenna inside paper.
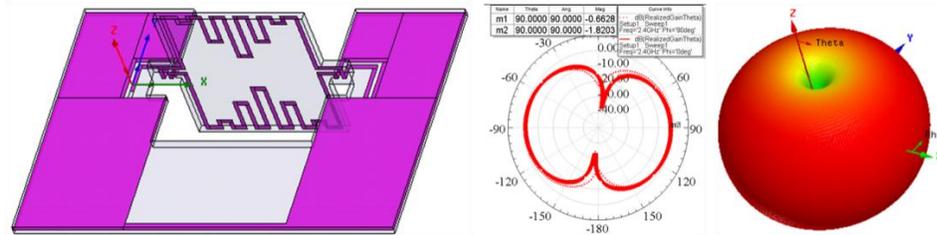
Figure 3.13: Embedded antenna inside paper and its 2D/3D radiation patterns.

- Fabrication of crawler antennas to be embedded in thin paper

The proposed antenna needs to be fabricated on very thin film in order to provide flexibility, which enables the bending connection between feeding line and an antenna. It is difficult to fabricate antennas on films only using general substrate-processing technology such as milling and chemical etching. Suitability and drawbacks of various fabrication methods are investigated. Fig. 3.14 shows three popular fabrication methods (Lift-off, Shadow mask and Etch-back). In the Lift-off method, Photoresist (PR) is first deposited on a polyester sheet and exposed to light with a proper mask. Depending on the polarity of PR, PR corresponding to the antenna pattern is removed or remained. This process is finished by depositing metal on the patterned PR and then dissolving the rest of PR which is covered with metal. The metal over PR is also removed when PR is dissolved and only the areas where there was no PR will be covered by metal. The drawback of this process is the difficulty of dissolving thick PR of 2μm totally at the first step. Shadow Mask is also a popular process for depositing a thick metal layer. However, this method is not appropriate for the wing antennas since the isolated thin patterns between metallic traces in the center of MASK cannot be supported. Therefore, we used

58

the Etch-back method to fabricate wing antennas. In this method, the metal is first deposited and PR deposited next. Similar to Lift-off, the exposed PR forms the desirable pattern. After etching metal, the covered PR on the metal patterns is removed. Based on this method, 2µm Gold layers is deposited on 25µm polyimide using sputter and etched chemically.

(a)   (b)   (c)
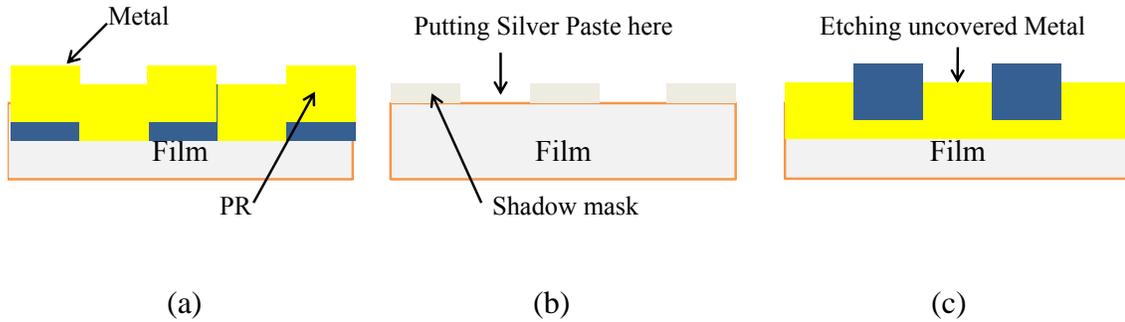
Figure 3.14: (a) Lift-off, (b) Shadow mask, and (c) Etch-back.

Fig. 3.15 shows equipment for etch-back process. The function of photoresist laminator is to put photoresist (PR) on the thin film of up to 12 inch width with high pressure and temperature (105°C). Exposure machine allows large PR of up to 40cm by 40cm to expose to the light. Magnetron sputtering system is chosen for thin film deposition since it provides stronger adhesion, compared to evaporator machine.

(a)   (b)   (c)
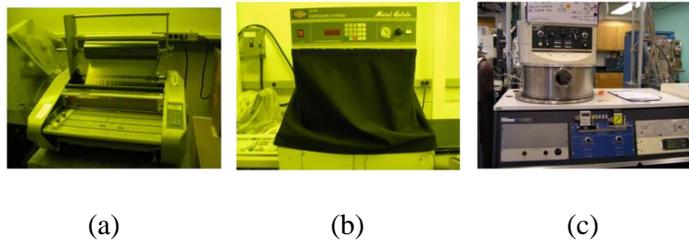
Figure 3.15: (a) Photoresist laminator, (b) exposure machine, and (c) sputtering system.

Some problems had to be handled to fabricate antennas on very thin film, as shown in Fig. 3.16. Firstly, sputtering causes tensile stress problem. It is very serious problem for the deposition of thick metal (>2µm) on thin film (25µm). In order to reduce the tensile stress generated during sputtering, the position of the source is properly

59

controlled. Secondly, long deposition times cause the damage of PET such as melting due to high temperature. Fabrication conditions such as deposition time and target position were properly optimized to solve these problems.

(a)   (b)   (c)
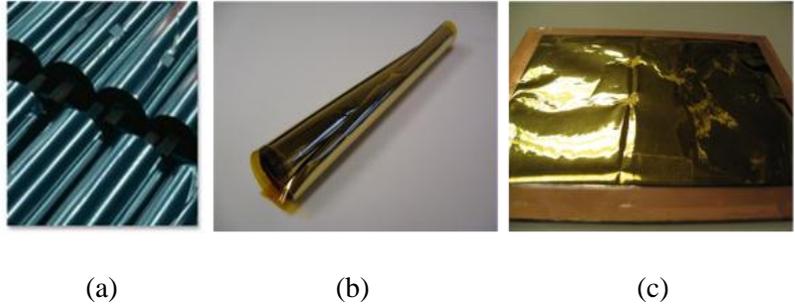
Figure 3.16: (a) Commercial PET (Polyester) film, (b) rolled thin film by tensile stress and (c) damaged metal surface by high temperature.

- Measurement set up and results for crawler antennas

Fig. 3.17 shows fabricated antennas including alignment keys to be matched exactly with the layout of a crawler robot. It is embedded in between top and bottom carbon papers after aligned carefully. Laser cut path of carbon papers for embedded antenna is shown in Fig. 3.17. Fig. 3.18 shows measurement set up and its simulation model. Coaxial cable is used to achieve the feeding at the proper location, which is combined with gold layer on thin film by silver paste. This actual measurement set up is considered in simulation results. As expected, adding the coaxial cable doesn't affect the performance of original proposed antenna.
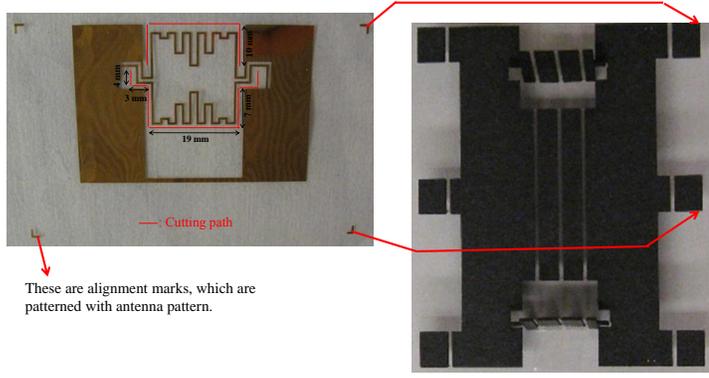
Figure 3.17: Fabricated antenna with alignment marks.
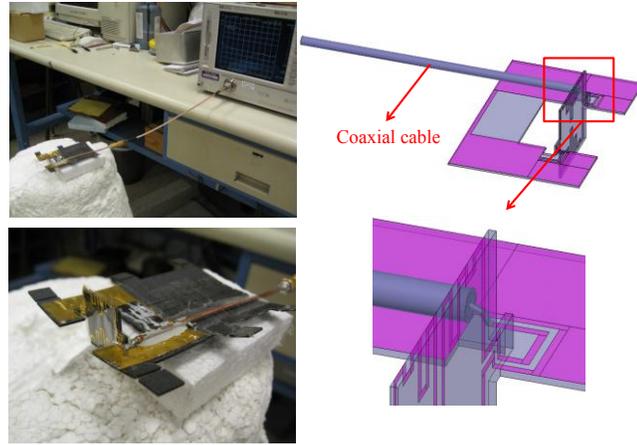
(a)   (b)
Figure 3.18: (a) Measurement set up and (b) its simulation model.

Fig. 3.19 shows the measured return loss which has good agreement with the simulated return loss.
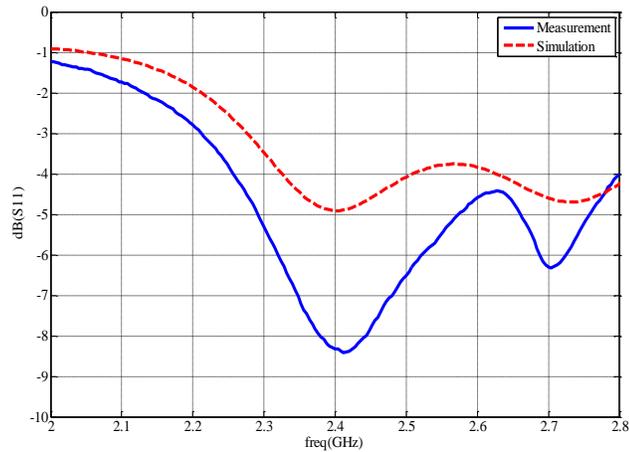
Figure 3.19: Measured and simulated return loss (S_{11}).

Fig. 3.20 depicts measured E and H-plane related vertical polarization. Based on the gain of ordinary half wavelength dipole antenna, the gain with vertical polarization on H-plane is obtained as between 0.3 and -3.7 dB, which is well matched with simulation results.
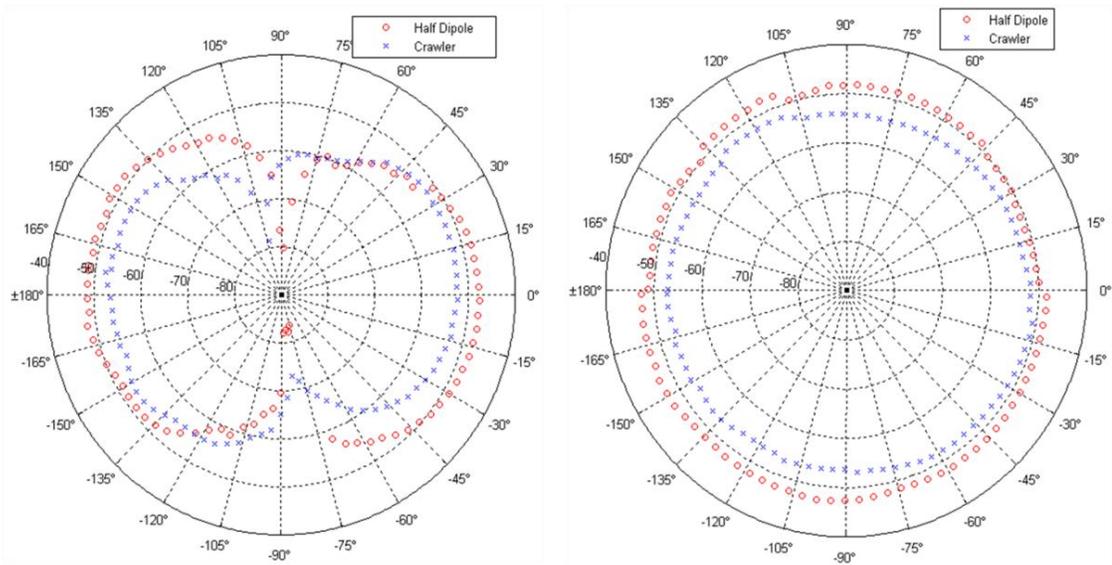
Figure 3.20. Measured (a) E-planes and (b) H-planes of λ/2 dipole and proposed antennas.

- Embedding fabricated antennas into crawler robot

The fabricated antennas were embedded inside a crawler by Prof. Rons Fearing's group, University of California, Berkeley. As shown in Fig. 3.21, a proposed antenna was successfully embedded in crawler robot made of carbon paper.

Figure 3.21: Embedded antenna inside a crawler robot.

Some parts of top paper layer are removed to put Bluetooth module. The RF output from Bluetooth module is connected to feeding line of an antenna through wire bonding. Fig. 3.22 describes how Bluetooth model and embedded can be integrated in a crawler robot.

Wire for connection between the output from Bluetooth module and antenna

	Bluetooth Module	Top Paper Layer

Bottom Paper Layer

1 mil-thickness Metallized Film layer including Antenna
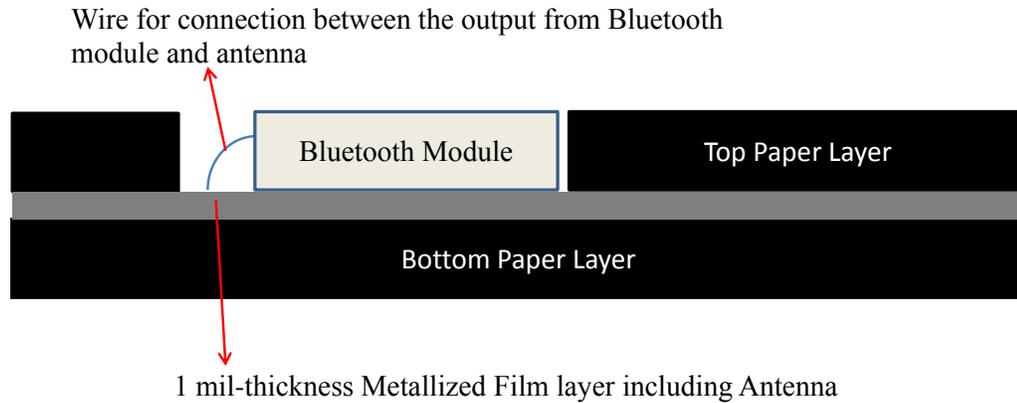
Figure 3.22: Integration of embedded antenna in thin paper with Bluetooth module.

3.2 Low-profile Omnidirectional Wideband Antenna

3.2.1 Introduction

Broadband antennas with vertically polarized omnidirectional radiation pattern in the azimuthal plane have attracted significant attention for their applications in wireless communications such as unattended ground sensor networks and wireless local area network (WLAN) systems [67]-[71]. Vertical polarization is important for near-ground applications in so far as the path-loss is concerned and omnidirectional radiation characteristic is needed for wide coverage in all directions. It is reported that near-ground propagation path loss between two near-ground antennas for vertically oriented antennas is by many orders of magnitude lower than any other antenna orientation configurations [8]-[9]. Quarter-wave ($\lambda/4$) monopole antenna is a typically used for near-ground communication applications. However, the size of the ground plane must be large, antenna height may be prohibitively large ($\lambda/4$) and its bandwidth is relatively low (<10%). The literature concerning antenna miniaturization is vast but far less for low profile, electrically small, wideband and vertically polarized antennas. Many different types of low-profile inverted-F antenna have been the most commonly used [15]-[16].

However, in most of such antenna topologies, only a short vertical segment of the resonant structure contributes to the vertically polarized radiation, while the much larger portion of the antenna structure generates higher radiation with undesired polarizations. This causes poor polarization purity and a serious deformation in the desired omnidirectional radiation pattern [17]. Recently, a new type of low-profile antenna with omnidirectional radiation pattern and vertical polarization was reported [40]. The concept is based on a superposition of multiple quarter-wave segments that are meandered and spiraled around to suppress the radiation from horizontal currents above the ground plane. As a result, the antenna features a pure vertically polarized radiation in the horizontal plane.

Various types of multiband and wideband inverted-F antennas with parasitic elements have also been reported [72]-[75]. In these papers inverted-L parasitic elements are inductively coupled to the inverted-F antennas to enhance the bandwidth. The inductively coupled parasitic element method for improving the bandwidth is widely used because of its simplicity in design and ease of integration with inverted-F antennas. In order to achieve the required level of inductive coupling, the parasitic elements are positioned close to the feeding segment of the inverted-F antennas which perturbs the uniformity of radiation pattern. In addition, similar to ordinary inverted-F antennas, these antennas are in capable of generating pure vertical polarization in the horizontal plane of the antenna.

Section 3.2 presents a novel antenna topology that makes use of capacitively coupled parasitic elements to achieve broad bandwidth without perturbing omnidirectional radiation pattern or the polarization of the antenna. The proposed antenna

is a combination of meandered λ/2 folded (bent over a ground plane) monopole antenna coupled capacitively to the parasitic elements. In Section 3.2.2.1, the behavior of the input impedance of the capacitively coupled parasitic elements is studied based on its equivalent circuit model. In Section 3.2.2.2, the resonant modes of the antenna with a parasitic element as a function of the parasitic element parameters are determined based on which a design procedure is developed. In Section 3.2.3.1, geometrical optimization of the antenna structure is presented to achieve omnidirectional radiation pattern and impedance matching to a 50Ω feed. In Section 3.2.3.2, a meandered λ/2 folded monopole antenna with a single parasitic element is designed. In Section 3.2.3.3, the antenna bandwidth is enhanced by introducing an additional capacitive coupled parasitic element.

3.2.2 Circuit Analysis of Folded Monopole Antenna with Capacitively Coupled Parasitic Element

3.2.2.1 Equivalent Circuit Model of Capacitively Coupled Parasitic Element

A λ/2 folded monopole antenna is used as the starting point for the proposed wideband, omnidirectional, vertically polarized antenna with small dimensions. Here λ/2 folded monopole antenna refers to a short circuited microstrip transmission line fed from one end by a vertical pin. The bandwidth of the folded monopole antenna based on λ/2 transmission line (TRL) is wider than that of the conventional λ/4 inverted F antennas, just as the bandwidth of λ/2 folded dipole antenna is 2~3 times wider than ordinary λ/2 dipole antenna [75]-[76]. In addition, modifying the antenna topology to be fitted in a small area allows for omnidirectional radiation pattern, as will be discussed in Section 3.2.3.1. Fig.

3.23 shows the directions and the magnitude of electric currents on a conventional $\lambda/2$ folded monopole antenna. Two radiating vertical elements at both ends of the TRL are responsible for vertically polarized omnidirectional radiation. This section presents the operation of the capacitively coupled parasitic element to excite an additional resonant frequency (f_{low}) lower than the original operating frequency (f_{high} where $f_{high} > f_{low}$) of the folded monopole antenna. Positioning the two resonant frequencies close to each other results in increasing the bandwidth of the antenna. It is shown that this can be done by adding a reactive parasitic element.
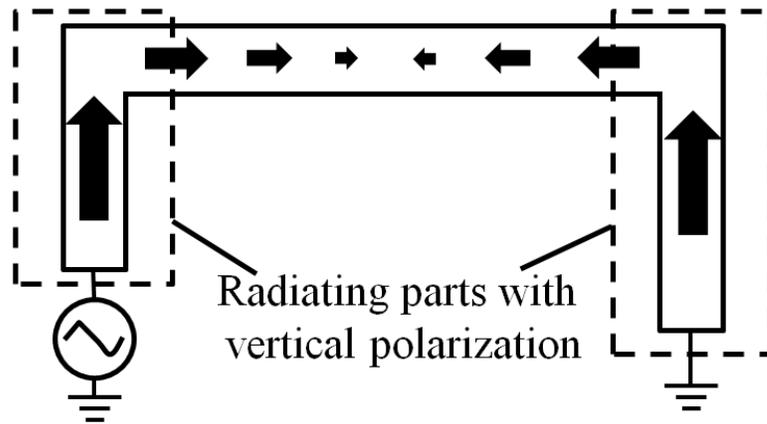
Figure 3.23: Directions and amplitudes of electric currents on $\lambda/2$ folded monopole antenna.

(a)   (b)
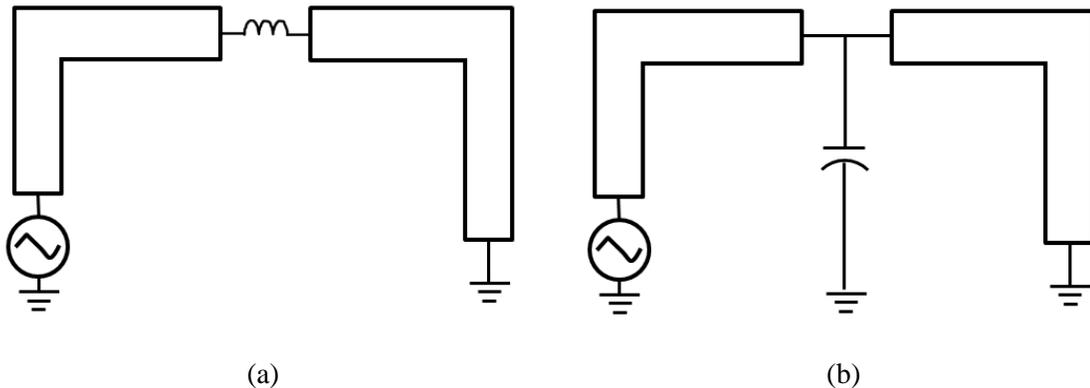
Figure 3.24: Folded monopole antennas with (a) a series inductor and (b) a shunt capacitor to excite the lower resonant frequency (f_{low}).

(a)   (b)
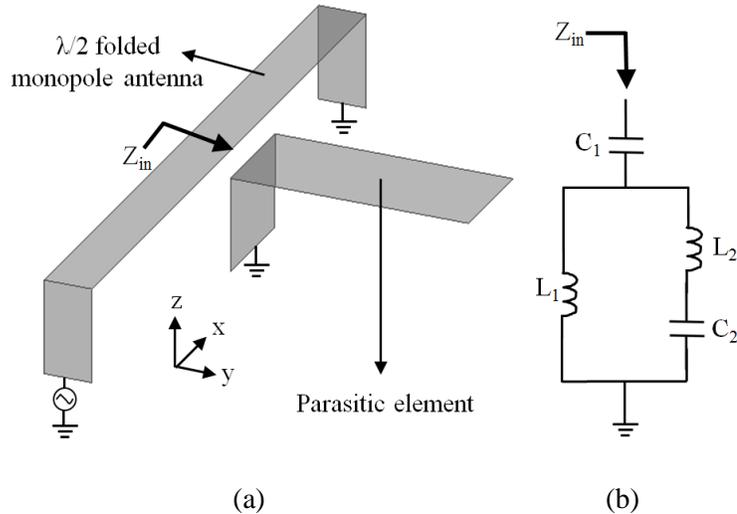
Figure 3.25: (a) Side view of $\lambda/2$ folded monopole antenna with a capacitively coupled parasitic element and (b) equivalent circuit model of the parasitic element.

Let us consider the required antenna configuration to excite the resonance at f_{low}. The original operating frequency (f_{high}) can be moved down to f_{low} by adding a series inductor or a shunt capacitor to the transmission line as shown in Figs. 3.24(a) and 3.24(b) due to an additional phase shift through the reactive elements. Our goal is to design a proper reactive parasitic element supporting two resonant frequencies (f_{low} and f_{high}) simultaneously as a way to enhance the bandwidth. It is proposed to simultaneously excite both resonant modes by positioning an inverted-L parasitic element with proper length and distance near the middle of the $\lambda/2$ folded monopole antenna where the electric filed is maximum.. Because of the high electric field in the middle of the antenna, the antenna can establish a strong capacitive coupling with a parasitic element at that location. Counter intuitively, the short-circuited end is placed near the folded antenna in order to excite the desired mode. This way the short-circuited end that acts as an inductor appears as a shunt element to the open-ended stub and are both connected to the series parasitic capacitance. Fig 3.25(a) shows the $\lambda/2$ folded monopole antenna capacitively coupled to the inverted-L

parasitic element. Fig. 3.25(b) shows the equivalent circuit model of the parasitic element.

Input impedance (Z_{in}) of the equivalent circuit model can be found from

$$Z_{in} = \frac{L_1 L_2 C_1 C_2 w^4 - (L_1 C_1 + L_1 C_2 + L_2 C_2)w^2 + 1}{jwC_1\left(1 - (L_1 C_2 + L_2 C_2)w^2\right)} \tag{3.1}$$

At $w = 1/\sqrt{L_1 C_2 + L_2 C_2}$ where $w = 2\pi f$, Z_{in} is infinite and thus no electric currents are induced on the parasitic element. As a result, the antenna works as if the parasitic element doesn't exist. On the other hand, at frequencies where

$w < \sqrt{(Y - \sqrt{Y^2 - 4/(L_1 L_2 C_1 C_2)})/2}$, $\mathrm{Im}(Z_{in})$ becomes negative (capacitive), noting that

$Y = 1/(L_1 C_1) + 1/(L_2 C_1) + 1/(L_2 C_2)$. In this case, the antenna structure works the same way as the topology shown in Fig. 3.24(b). Therefore, the use of the capacitively coupled inverted-L parasitic element enables the operations corresponding to two resonant frequencies (f_{low} and f_{high}) simultaneously. In order to further investigate the operation of the capacitively coupled parasitic element, the imaginary part of Z_{in} of the equivalent circuit model of the parasitic element is compared with that of the circuit without the coupled capacitance (C_1), as shown in Fig. 3.26. The values of the lumped elements are chosen as C_1=0.5pF, L_1=20nH, C_2=3pF and L_2=20nH, approximately corresponding to physical dimensions of the parasitic element for frequency of operation at f_{high} =460MHz. It is found that below 460MHz the imaginary part of Z_{in}, in the presence of C_1, becomes negative (capacitive). This is desirable since it allows excitation of an additional resonance at a frequency lower than 460MHz, as discussed earlier. The physical length of the folded monopole antenna is designed to be λ/2 at 460MHz (f_{high}) that must match the pole of (3.1) given by $f_{pol} = 1/(2\pi \sqrt{L_1 C_2 + L_2 C_2})$.
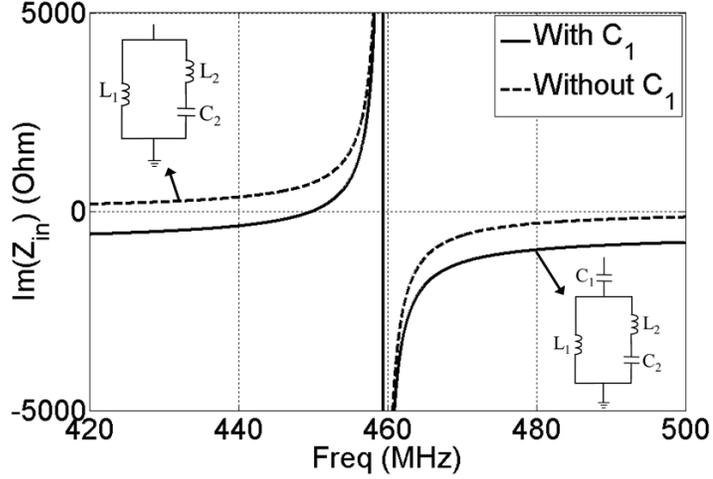
Figure 3.26: Imaginary part of Z_{in} in the equivalent circuit model of the capacitively coupled parasitic element shown in Fig. 3.25(b), compared to the same circuit model without C_1.

3.2.2.2 Parametric Study to Set up Design Procedure

In order to develop a design procedure for the proposed wideband antenna, it is essential to investigate the characteristics of the two resonant frequencies as a function of design parameters of the parasitic element. The design parameters are the gap between the $\lambda/2$ folded monopole antenna and the parasitic element (corresponding to C_1 in Fig. 3.25(b)), the width and height of the shorting strip (L_1) and the geometry of the top plate (C_2 and L_2). Another important parameter to estimate is the characteristic modes of the antenna structure. To determine the resonant frequencies the transverse resonance technique can be used. This technique is based on the fact that at any point on the resonant TRL, the sum of the input admittances (impedances) seen looking into either sides must be zero at the resonant frequencies. That is,

$$Y_{in}^{r}(x) + Y_{in}^{l}(x) = 0, \text{ for all } x, \tag{3.2}$$

69

Where $Y_{in}^r(x)$ and $Y_{in}^l(x)$ are the input admittances seen looking to the right and left, respectively, at the point x on the resonant TRL. Referring to Fig. 3.27, this condition renders

$$\frac{1}{jZ_0 \tan \beta_0 l} + \frac{1}{jZ_0 \tan \beta_0 l} + \frac{jwC_1(1 - (L_1 C_2 + L_2 C_2)w^2)}{L_1 L_2 C_1 C_2 w^4 - (L_1 C_1 + L_1 C_2 + L_2 C_2)w^2 + 1} = 0 \quad (3.3)$$

Where Z_0 is the characteristic impedance of the TRL (chosen as 200Ω), β_0 is the propagation constant in free space and l is $\lambda/4$ at 460MHz (λ is free space wave length)
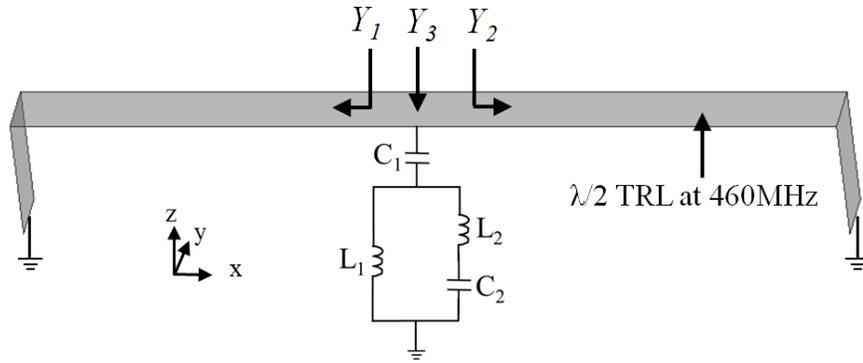
Figure 3.27: Input admittances toward two shorting sheets and parasitic element in the middle of a shorted $\lambda/2$ TRL.

The solutions of (3) give the two resonant frequencies (f_{low} and f_{high}) as a function of C_1, L_1, C_2 and L_2, as shown Fig. 3.28. Except for the lumped element under parametric study, all other values are fixed as the same values used in Section 3.2.2.1. Fig. 3.28(a) shows that as C_1 increases, f_{low} decreases while f_{high} doesn't change as expected. This means that the change in the gap distance between the $\lambda/2$ folded monopole antenna and the parasitic element only results in the shift of f_{low}. On the other hand, Fig. 3.28 (b), (c) and (d) suggest that the increase in L_1, C_2 or L_2 leads to the decrease in f_{high} as well as f_{low}. This is due to the fact that the pole of (3.1) is a function of L_1, C_2 and L_2 and thus once their value is changed, the pole of (3.1) is not equal to the frequency at which the electrical

length of the folded monopole antenna is seen as $\lambda/2$ any longer. As a result, the f_{high} moves down to satisfy the resonance condition of (3.4).

It is expected that both f_{low} and f_{high} can be decreased by increasing the area of the top plate along y-axis or decreasing the width of the shorting strip of the parasitic element. Based on this parametric study, a design procedure to optimize the geometry of the parasitic element can be established. Firstly, for a given lateral dimensions, the area of the top plate of the parasitic element needs to be maximized to lower both f_{low} and f_{high}, leading to antenna miniaturization. Secondly, L_1 is tuned to make the pole of (3.1) to be positioned around the frequency at which the electrical length of the folded monopole antenna is seen as $\lambda/2$. Next, since the change of C_1 only affects f_{low}, the desired separation between f_{low} and f_{high} can be set to maximize the bandwidth for a desired minimum return loss. The frequency separation can be adjusted by controlling the gap distance between the antenna and the parasitic element.

(a) (b)

(c) (d)
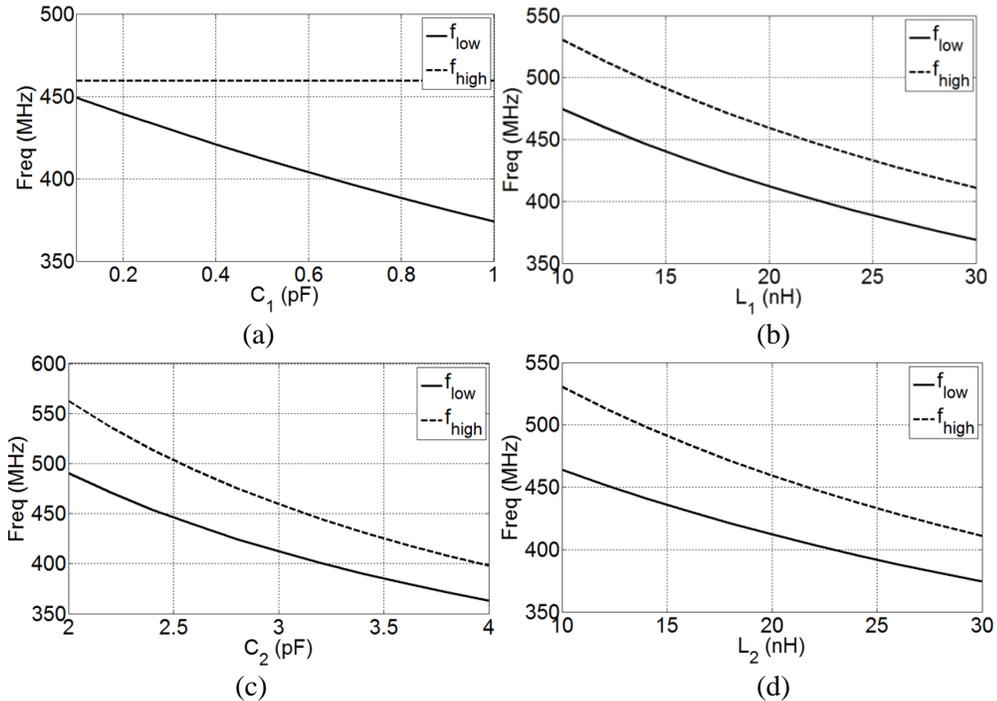
Figure 3.28: f_{low} and f_{high} versus (a) C_1, (b) L_1, (c) C_2 and (d) L_2 in the equivalent circuit model of the parasitic element in Fig. 3.27. Each plot shows the fixed values of other parameters.

3.2.3 Antenna Design

3.2.3.1 Design of Meandered Folded Monopole Antenna

This section presents the geometry optimization of the $\lambda/2$ folded monopole antenna to achieve omnidirectional radiation pattern and impedance matching to a 50Ω feed. Fig. 3.29 shows the geometries and electric current distributions over a straight $\lambda/2$ folded monopole antennas matched to a 50Ω port. Since the separation between the two vertical pins of the antenna is $\lambda/2$ and the electric currents on the vertical pins are in-phase, there is an undesired cancellation of vertically polarized radiation along the x-axis. In order to achieve omnidirectional radiation pattern in the horizontal plane (xy plane), the lateral dimension of the antenna must be reduced to avoid the radiation cancellation. Meanwhile, the polarization purity of the straight $\lambda/2$ folded monopole antenna must be maintained. As shown in Fig. 3.29(a), horizontal electric currents on the left side of the top plate are in the opposite direction of those on the right side. This suppresses the radiated fields with undesired (horizontal) polarization from the metallic trace on the top plate. This desired property can be maintained by making the metallic trace meander in the way shown in Fig. 3.29(b). Fig. 3.30 shows the design parameters of the antenna geometry. Since a short segment (L_c) can work as an impedance transformer, impedance matching to a 50Ω feed can be obtained by tuning L_c and W_b. Fig. 3.31 shows the simulated S_{11} as a function of W_b where the values of other parameters are fixed as L_a=200mm, L_b=85mm, L_c=70mm, W_a=42.5mm and W_c=30mm. For the full-wave electromagnetic (EM) simulations, Ansoft HFSS 13.0 is used.
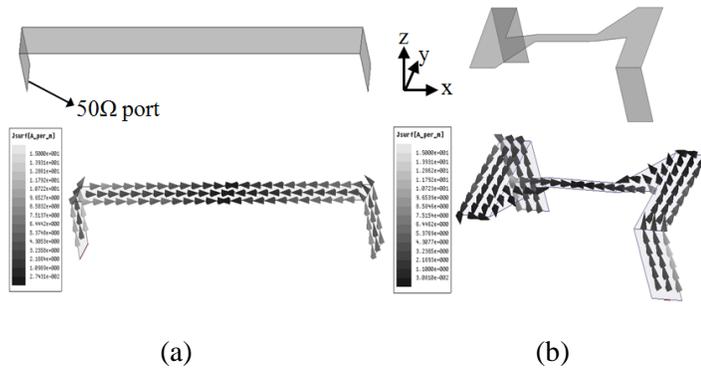
Figure 3.29: Geometries and electric current distributions of (a) the straight and (b) meandered $\lambda/2$ folded monopole antenna.
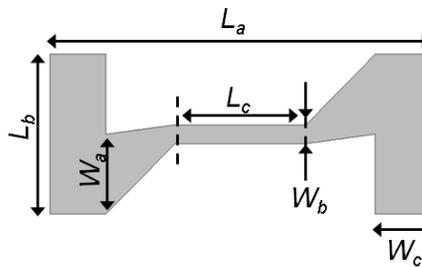
Figure 3.30: Design parameters of the meandered $\lambda/2$ folded monopole antenna.
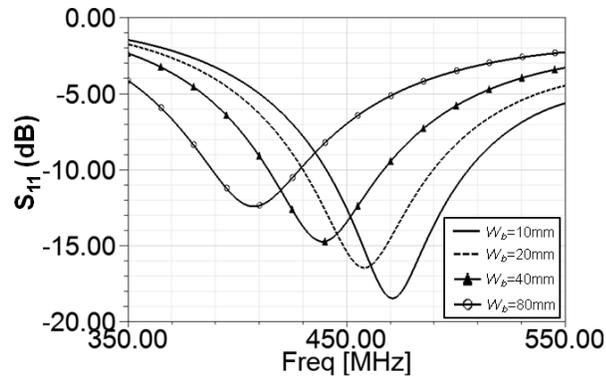
Figure 3.31: Simulated S_{11} of the modified folded monopole geometry as a function of width parameter W_b shown in Fig. 3.30.

3.2.3.2 Design of Meandered Folded Monopole Antenna with One Parasitic Element

The capacitively coupled parasitic element combined with the meandered $\lambda/2$ folded monopole antenna is optimized, based on the design procedure proposed in Section 3.2.2.2. Fig. 3.32 shows three design parameters determining the geometry of the parasitic

element. In order to maximize C_2 and L_2 in Fig. 3.25(b) for a given area, a trapezoid-shaped top plate is chosen. Once the value of L_d is decided, the value of W_d is appropriately chosen to make the pole of (3.1) to be positioned around the frequency at which the electrical length of the folded monopole antenna is $\lambda/2$. The proper separation between f_{low} and f_{high} can be designed by tuning the gap distance g because C_1 only affects f_{low}. Changing W_d and g slightly, excellent impedance matching to a 50Ω feed at both f_{low} and f_{high} is obtained. Fig. 3.33 shows simulated S_{11} as a function of g, L_d and W_d. The initial values used for this study are g=15mm, L_d=81mm, W_d=65mm and h=60mm. As expected, while the change in g only affects f_{low}, the change in L_d does both f_{low} and f_{high}, showing the behavior predicted by circuit simulations. On the other hand, decreasing W_d only lowers f_{low}, contrary to the circuit-model prediction where the increase in L_1 results in lowering both f_{low} and f_{high}. This difference is due to the fact that the change in W_d also causes a change in C_1 and the transition geometry between the shorting sheet and the top plate.
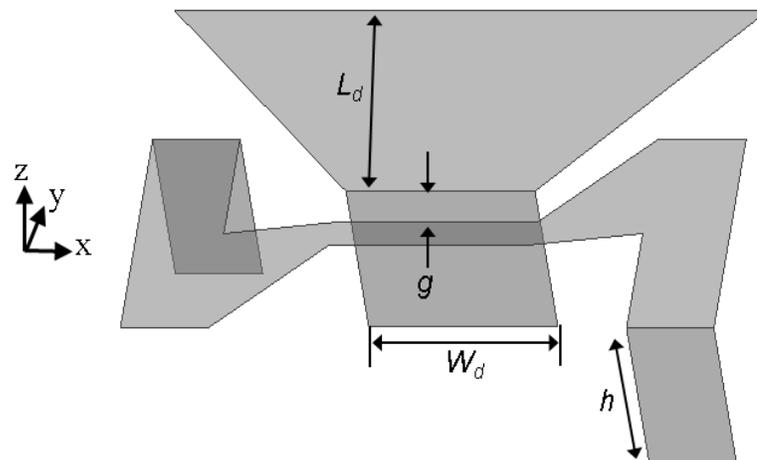
Figure 3.32: Geometry and design parameters of the meandered $\lambda/2$ folded monopole antenna with the capacitively coupled parasitic element.

(a)

(b)

(c)
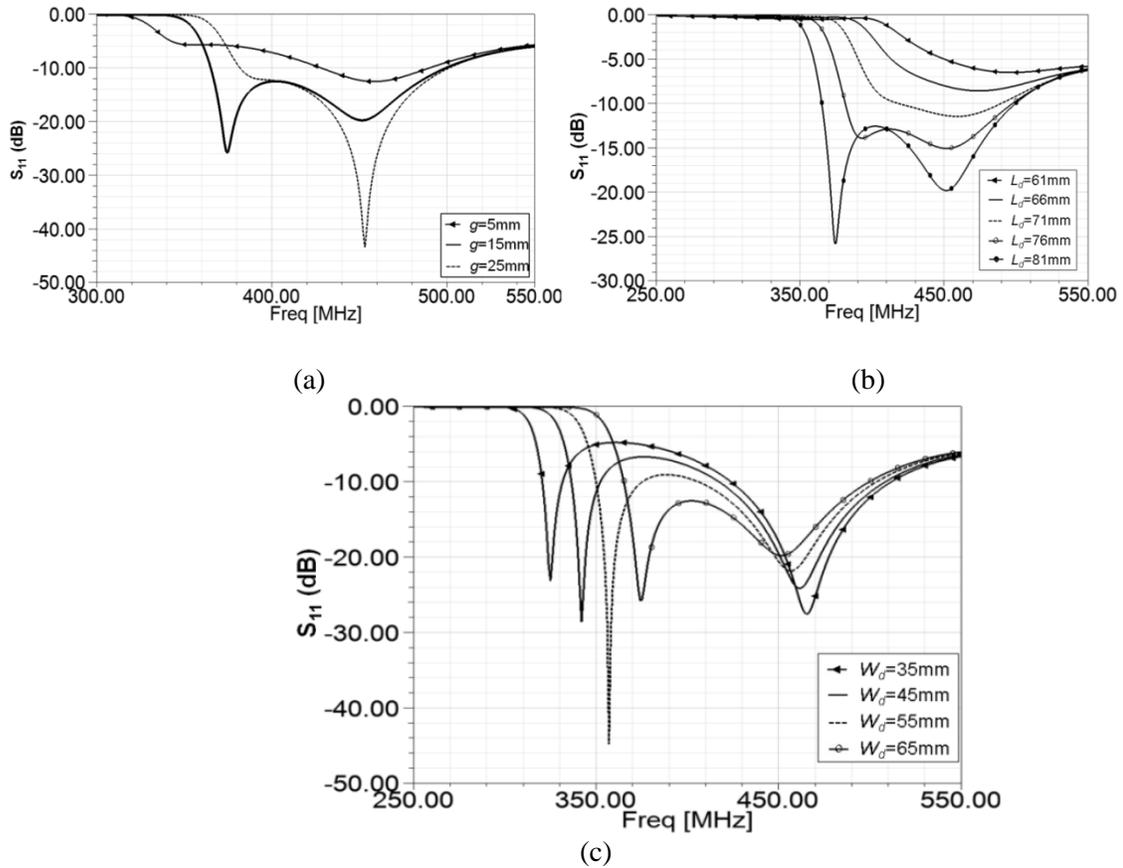
Figure 3.33: Simulated S_{11} as a function of (a) g, (b) L_d and (c) W_d.

3.2.3.3 Bandwidth Enhancement Using Two Back-to-Back Parasitic Elements

Introducing an additional parasitic element to the antenna topology with one parasitic element, as shown in Fig. 3.32, makes the antenna topology symmetric with respect to the E plane (xz plane). This has the potential to enhance the antenna performance. Noting that the electric currents on the horizontal plane of the second parasitic element are in the opposite direction of those on the first parasitic element ensures cancellation of horizontally polarized radiated fields from the first and second parasitic elements. This will enhance the polarization purity of the vertically polarized

antenna. The addition of the second parasitic element with identical dimensions does not change the circuit model and the principle of operation, but it allows storage of electric and magnetic energy over a larger volume, which should result in higher bandwidth. In addition, tuning the dimensions of the second parasitic element provides the opportunity to excite another resonance. Considering the second parasitic element with dimensions identical to those of the first element, as discussed in the previous section, the performance of the modified antenna is studied. Fig. 3.34 shows the geometry and design parameters of the modified antenna topology. In order to compensate the slight change in impedance matching due to the addition of the second parasitic element, W_a is adjusted. The values of design parameters are given by L_a=200mm, L_b=85mm, L_c=75mm, L_d=81mm, W_a=85mm, W_b=8mm, W_c=30mm, W_d=65mm, g=15mm and h=60mm. Fig. 3.35 shows the simulated S_{11} corresponding to three cases: i. Antenna without any parasitic element (denoted by 'no parasitic'), ii. Antenna with one parasitic element ('one parasitic') and iii. Antenna with two parasitic elements ('two parasitic'). Comparing the case of 'one parasitic' to the case of 'two parasitic', it is shown that the addition of the second parasitic element lowers both flow and fhigh, and enhance the antenna bandwidth. Fig. 3.36 shows electric current distribution at 328MHz and 419MHz of the proposed antenna shown in Fig. 3.34 (Case iii in Fig. 3.35). As intended, all the electric currents in the horizontal plane of the antenna have a counterpart that is in the opposite direction, leading to the cancellation of the radiated fields from the top plates.
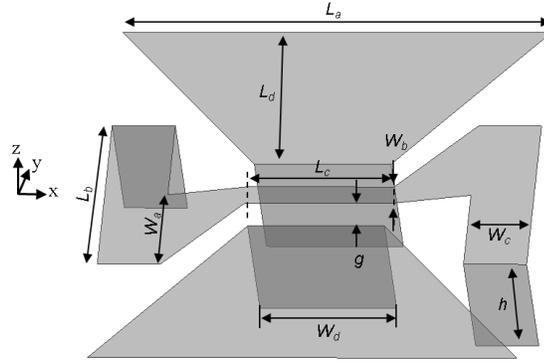
Figure 3.34: Geometry and design parameters of the omnidirectional antenna topology with two back-to-back parasitic elements.
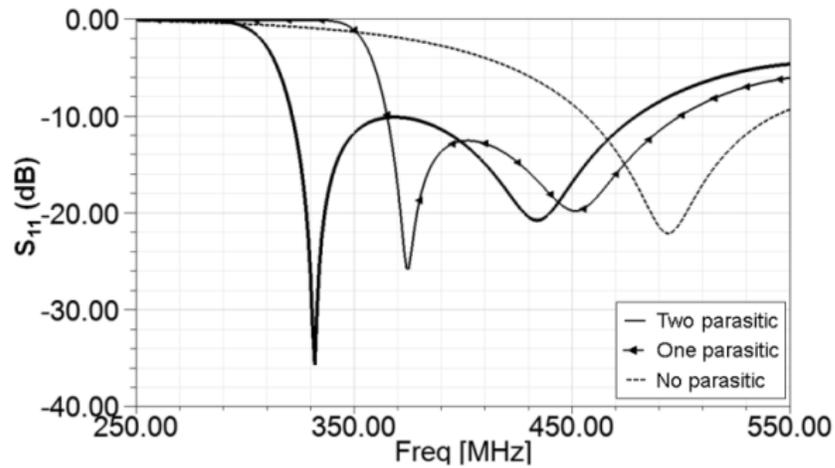
Figure 3.35: Simulated S_{11} of the proposed antenna corresponding to three cases: *i*. Antenna without any parasitic element ('no parasitic'), *ii*. Antenna with one parasitic element ('one parasitic') and *iii*. Antenna with two parasitic elements (denoted by 'two parasitic').
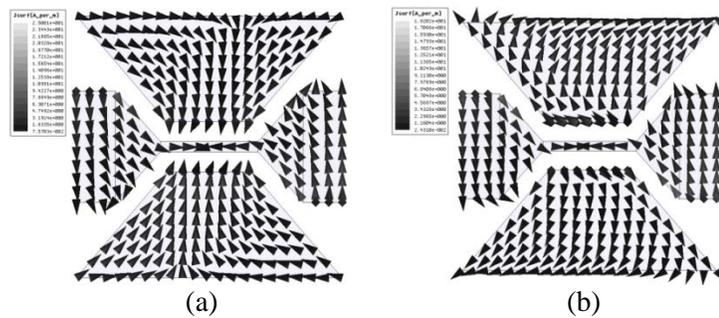
Figure 3.36: Horizontal electric current distributions at (a) 328MHz and (b) 419MHz.

The antennas corresponding to Case *i*, *ii* and *iii* are fabricated and measured. Fig. 3.37 shows the measured S_{11} of the fabricated antennas. Fig. 3.38 and 3.39 show the measured radiation patterns of the proposed antenna (Case *iii*) at 310MHz and 430MHz. At both

frequencies, the desired omnidirectional radiation patterns with a null in the broadside direction are observed. In the proposed antenna topology, although the lateral dimensions are much larger than the vertical profile, the average ratios of co- to cross- polarization are as high as 7.5dB and 13.5dB at 310MHz and 430MHz, respectively. The size of the ground plane used in these measurements is $0.6\lambda_{LF}$ X $0.6\lambda_{LF}$ where λ_{LF} is the wavelength at the lowest frequency of the operation.
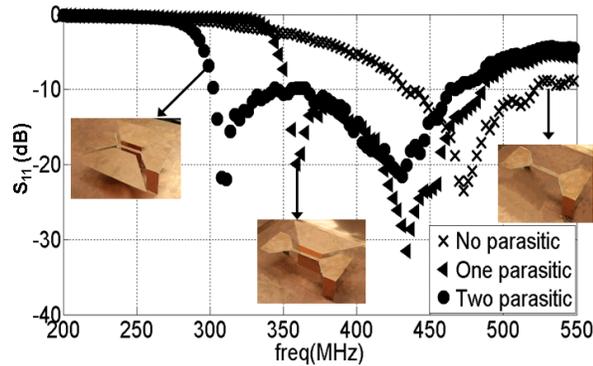
Figure 3.37: Measured S_{11} of the proposed antenna corresponding to the three cases: *i*. No parasitics, *ii*. One parasitic and *iii*. Two parasitics.

(a)   (b)
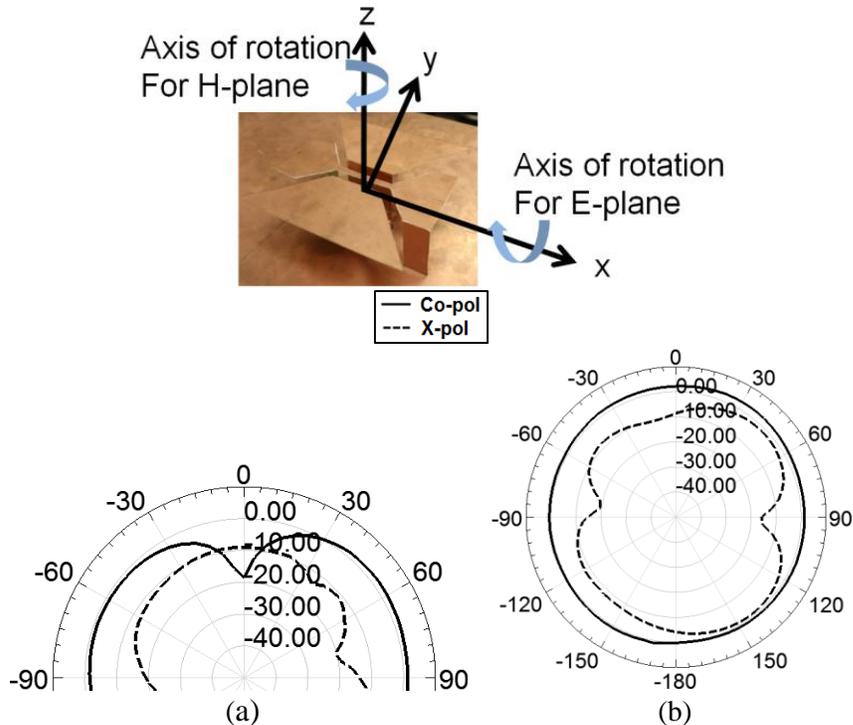
Figure 3.38: Measured radiation patterns of the proposed antenna at 310MHz: (a) E-Plane and (b) H-Plane.
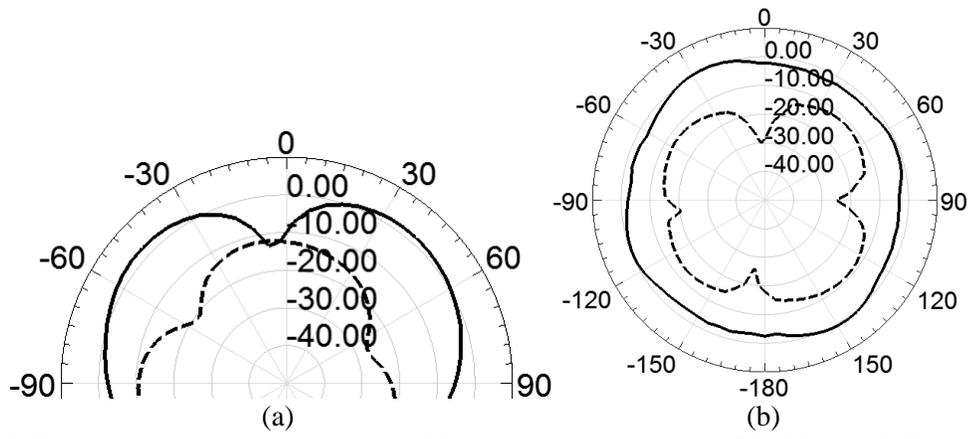
Figure 3.39: Measured radiation patterns of the proposed antenna at 430MHz: (a) E-Plane and (b) H-Plane.

Chapter 4

A Topology-Based Miniaturization of Circularly Polarized Patch Antennas

A novel topology-based approach for the miniaturization of circularly polarized patch antennas is presented. It is shown that this enables a size reduction of as high as 75%, compared to a conventional circularly polarized patch antenna [77], [78].

4.1 Introduction

Many modern satellite and terrestrial point-to-point communications systems use circularly polarized (CP) waves in order to maximize the polarization efficiency and thus improve the propagation link budget [11]. CP is also desirable in applications where the orientation of transmitting or receiving antennas may vary, such as mobile platforms. CP antennas have the ability to combine two orthogonal linearly polarized components of the radiated fields of equal amplitude and a 90° phase difference. Although a CP antenna with a low profile, small size and light weight is highly desirable in many applications such as compact satellite or mobile platforms [79], most miniaturization techniques are developed for linearly polarized antennas. This is mainly due to the fact that antennas with extremely small lateral dimensions are incapable of internally generating the required conditions for CP operations.

Many compact CP patch antennas have been proposed and investigated [24]–[25], [80]. These efforts have relied mainly on intuitive techniques such as inserting several slots or slits in suitable locations on the patch itself. In such antenna designs, the splitting of two near-degenerate orthogonal modes with equal amplitudes and a 90° phase difference is achieved by slightly adjusting the embedded slots, such as a cross-slot in a patch or slits at the boundary of the patch. Theses inserted slots and slits force redirection of the excited fundamental mode surface current and also cause the resonant frequency to be shifted down to some extent. However, this approach has yielded somewhat limited miniaturization due to lack of ability to simultaneously control the surface current paths as well as create the required 90° phase difference. It is shown that these methods can provide size reductions of as low as 50%. Although a size reduction of about 70% is also reported, the area covered by the feed structure makes the overall size bigger. This is due to the fact that such antennas with higher size reductions are not compatible with the direct probe-fed method since no 50Ω feed positions exist inside the microstrip patch due to the large cross-slot cut inside the patch [77], [78].

Circularly polarized patch antennas are often classified by feed type; single-fed type or dual-fed type, depending on the number of feed points necessary to generate the circularly polarized radiation. The single-fed type has the advantage of not requiring an external power divider and phase shifter, such as a 90° hybrid coupler. Although there are various single feed methods (direct, aperture-coupled and proximity-coupled feeds [81]), the direct single feed is the most desirable for its simplicity, light weight and low cost, and thus this will be the type of antenna feed that will be investigated in this work.

This work presents a new miniaturized circularly polarized (CP) probe-fed patch antenna. Section 4.2 presents a miniaturized linearly polarized patch antenna formed by an anisotropic conductor. Section 4.3 introduces a topology modification for generating two orthogonal modes, and Section 4.4 shows antenna topology designs for achieving circular polarization. Section 4.5 describes a topology optimization process for size reduction. Details in each design step and measurement results are discussed, and a size reduction of as high as 75% is demonstrated, as compared to the conventional corner-truncated CP square microstrip antenna.

4.2 Miniaturization of Linearly Polarized Patch Antennas Using Meandered Metallic Traces

4.2.1 Wire-Mesh Microstrip Patch Antenna

The proposed design approach for miniaturizing circularly polarized patch antennas starts from the miniaturization of a linearly polarized microstrip antenna using an anisotropic conductor. The anisotropic conductor is formed by removing parallel thin metal strips from the conventional microstrip antenna. The concept of the modified topology begins by considering electric current distribution on an ordinary rectangular microstrip antenna at its fundamental mode. In this case, the electric current is primarily parallel to one edge with a sinusoidal intensity variation attaining a null value at the edge. On the other hand, the electric field under the patch has maxima where the electric current is zero, forming two parallel fictitious magnetic currents responsible for the radiation of the patch antenna. Considering an ordinary $\lambda_g/2$ microstrip antenna with linear polarization along the x-axis (where $\lambda_g = \lambda_0/\sqrt{\epsilon_r}$, λ_0=free-space wavelength and ϵ_r=2.2), the progression of topology modification is shown in Fig. 4.1. The uniform metallic patch is replaced with a mesh which can be thinned out without performance loss

so long as the mesh dimensions are roughly smaller than $\lambda_g/15$. Basically, the radiation pattern is not changed, but the resonant frequency is reduced slightly. This is due to the fact that thin wires have some additional inductance per unit length. To demonstrate this, the metallic patch and the wire mesh version are simulated assuming perfect electric conductor (PEC) (ignoring ohmic loss) using Ansoft HFSS 12.1.

Fig. 4.2 shows the simulated return loss (S_{11}) and E-plane radiation patterns (xz-plane) of the wire mesh and the original $\lambda_g/2$ microstrip antenna. The gains of both antennas are about 7 dBi. The lateral dimension of the $\lambda_g/2$ microstrip antenna is 40mm, and the thickness and dielectric constant of the substrate are 3.175mm and 2.2, respectively. The size of the ground plane is 80mm X 80mm. The wire mesh antenna is designed with the same substrate and physical dimensions. As explained above, the resonant frequency of the wire mesh antenna is shifted down by about 10%.
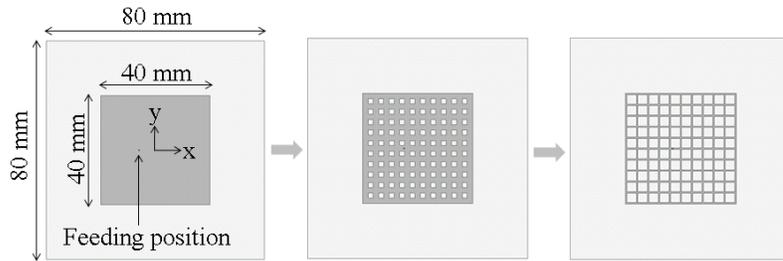
Figure 4.1: Conversion of a $\lambda_g/2$ microstrip antenna to an array of thin wires.

(a)   (b)
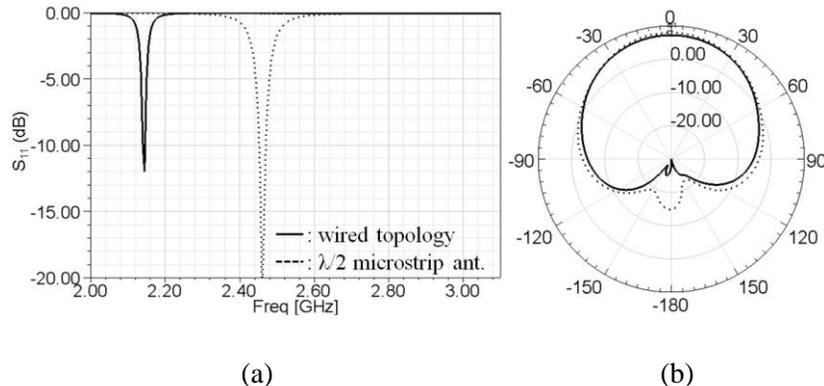
Figure 4.2: Simulated (a) S_{11} and (b) radiation pattern on xz-plane of a wire mesh patch antenna and a conventional $\lambda_g/2$ microstrip antenna with the same sizes and substrate.

83

4.2.2 Accordion Topology for Size Reduction

Straight wires in Fig. 4.1 are meandered to fit a longer path length in a given dimension, leading to the miniaturization of the linear dimension along the x-axis, as shown in Fig. 4.3(a). From this design step, the conductivity of copper is used in all metallic traces to consider ohmic loss. In order to reduce ohmic loss, the sharp edges of the meandered wires are made to be smoother, giving it a sinusoidal shape, as shown in Fig. 4.3(b). In addition, all metallic traces in parallel with the y-axis are eliminated, creating an anisotropic conductor, except for two wires at both ends and a wire connected with a feed probe. The end conductor strips are needed to facilitate uniform vertical electric fields between the conductors and the ground plane, which produces in-phase equivalent magnetic currents.

The topology shown in Fig. 4.3(b) still works as a linearly x-polarized antenna. As depicted in Fig. 4.4(b), the gain of this antenna is 5.5 dBi. The linear dimensions in both the x and y directions of the area covered by antenna pattern are 25.43mm (=$0.29\lambda_g$) and 40mm (=$0.46\lambda_g$), respectively. This renders a size reduction of 40%, compared to the conventional microstrip antenna.

(a)   (b)
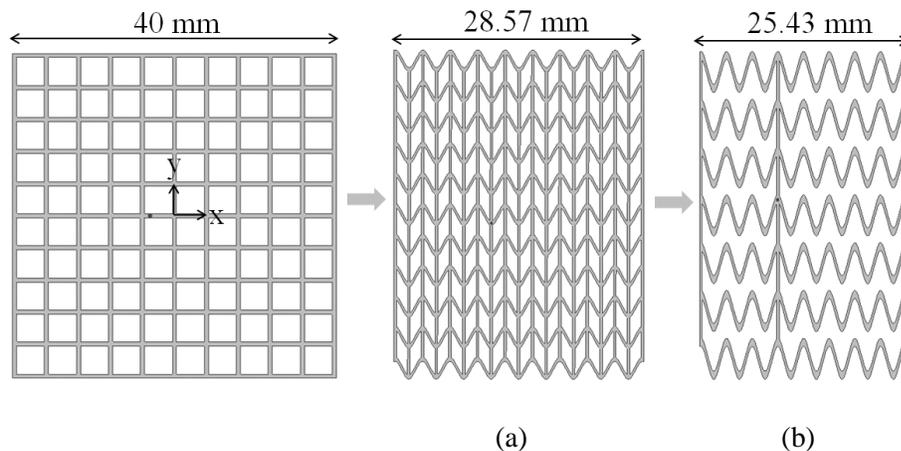
Figure 4.3: (a) Shrunk wires and (b) sinusoidal wires with the elimination of wires in parallel with y-axis.

(a)   (b)
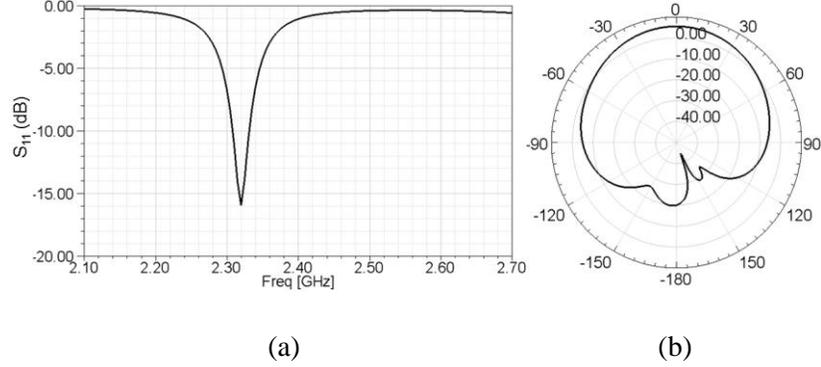
Figure 4.4: Simulated (a) S_{11} and (b) radiation pattern on xz-plane of the wired antenna depicted in Fig. 4.3(b).

4.3 Excitation of Two Near-Degenerate Orthogonal Modes

Starting with the accordion-shape patch antenna with linear polarization, modifications are sought to generate a simultaneous orthogonal polarization. Examining the topology shown in Fig. 4.3(b), it is obvious that y-directed electric surface currents can only be excited on the three y-directed wires. If a new resonance can be created by the currents, then y-polarized radiation can also be generated. It is found that two wires at both ends can act like two y-directed $\lambda_g/2$ dipole antennas. Appropriately extending and then bending two end wires, an additional resonant frequency related to y-polarized radiation can be created. Fig. 4.5(a) shows the modified topology and Fig. 4.5(b) shows simulated S_{11} and θ-polarized 3D radiation patterns at two resonant frequencies. At the first resonant frequency, where x-polarized radiation is dominant, a radiation null exists on the y-axis, and at the second resonant frequency, the radiation null exists on the x-axis.

Fig. 4.6 shows electric surface current distributions at two resonant frequencies of the topology shown in Fig. 4.5(a). As expected, while the surface current on the x-directed meandered wires is dominant at the first resonant frequency, the surface current on the y-directed two wires at both ends is dominant at the second resonant frequency.

85

| (a) | (b) |
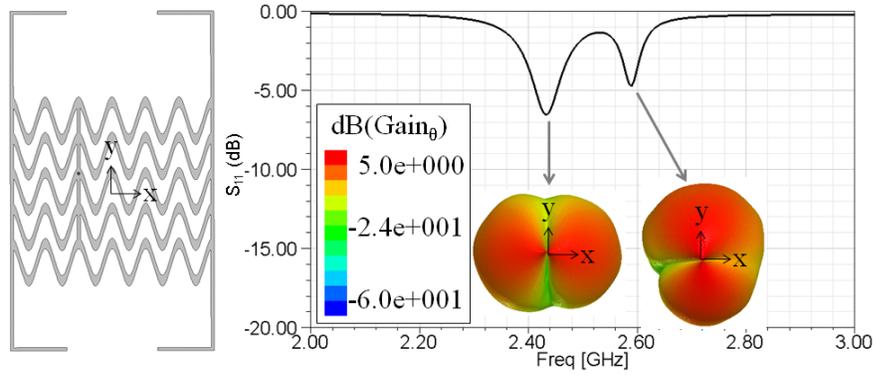
Figure 4.5: (a) Topology of a dual polarized antenna and (b) simulated S_{11} and θ-polarized 3D radiation patterns at two resonant frequencies.

| (a) | (b) |
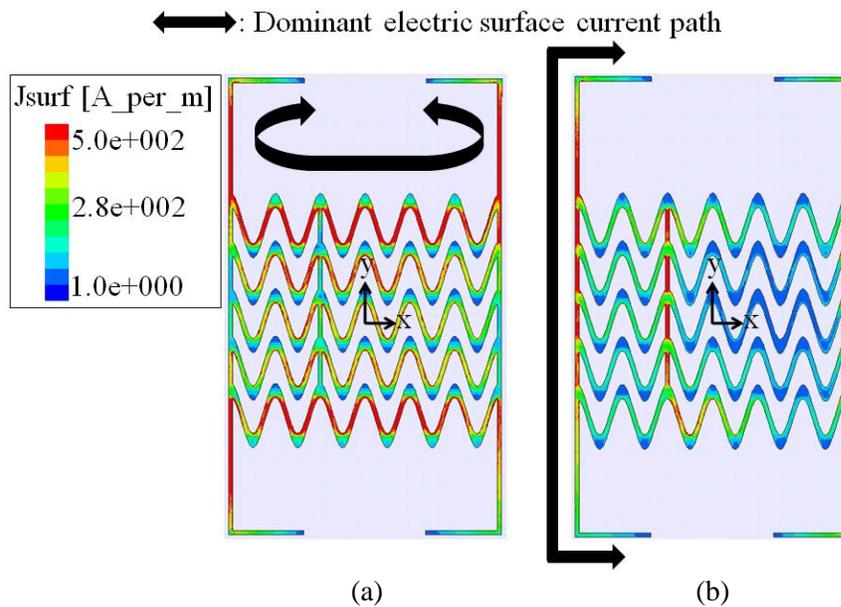
Figure 4.6: Electric surface current distributions at the resonant frequencies where the antenna radiates (a) x- and (b) y-polarized fields.

4.4 Design of Miniaturized CP Patch Antennas

In order to design a CP antenna using the topology shown in the previous section, the two resonant frequencies corresponding to two orthogonal modes must be at the same frequency, and the two orthogonal linearly polarized components of the radiated fields must have equal amplitudes and a 90° phase difference. This requirement makes the

miniaturization of CP antennas very difficult because the behaviors of the antenna at the two resonant frequencies must be controlled independently.

Considering the dominant electric surface current paths shown in Fig. 4.6, geometrical features must be extracted to independently tune the two resonant frequencies. Fig. 4.7(a) shows these tuning geometrical features of the structure. While l_1 and l_2 affect both the resonant frequencies, l_3 and l_4 only affect the electrical length related to the x-pol and y-pol, respectively. Varying these parameters simultaneously in such routines, the two split resonant frequencies can be merged into a single frequency with an acceptable return loss value as shown in Fig. 4.7(b). To achieve impedance matching with a 50Ω feed probe, parameters ($=f_x$ and f_y) related to a feeding position are appropriately optimized as well. The linear dimensions in both the x and y directions of the area covered by the antenna topology are 19mm and 32mm, respectively. This produces a size reduction of 59%, compared to a corner-truncated CP square microstrip antenna on the same substrate. In other words, the area of the proposed antenna is just 41% of that of a conventional CP square microstrip antenna. The values of other design parameters are given by l_1=5mm, l_2=6.86mm, l_3=46.3mm, l_4=g=2.83mm, f_x=6.13mm, f_y=16.1mm, w_1=0.3mm and w_2=1mm. For the sinusoidal meandering, a function of the form y=1.7cos(2x) is used where the argument is in radian and the value of the x dimension in millimeters is inserted.

It is interesting to note that if the positions of two resonant frequencies are moved slightly with respect to each other; both right-handed (RH) and left-handed (LH) CP can be obtained. When the resonant frequency of the x-pol is slightly lower than of that of the y-pol, the antenna radiates with RHCP. Contrary to this, when the resonant frequency of

the y-pol is slightly lower than that of the x-pol, the antenna radiates with LHCP. Fig. 4.8

shows a simulated axial ratio of the antenna shown in Fig. 4.7(a). The 3dB axial ratio

bandwidth is about 0.8%. Good RHCP radiation is observed in Fig. 4.9. The antenna gain

(RHCP) in the broadside direction is 5 dBi which is 2 dB lower than the conventional

corner-truncated square microstrip antenna due to size reduction.

(a)   (b)
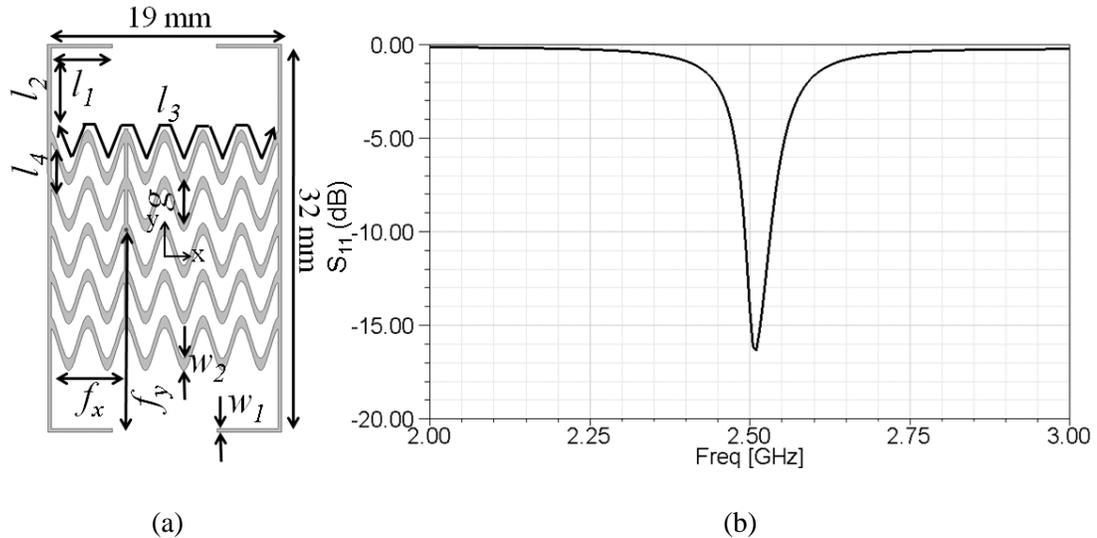
Figure 4.7: (a) Topology, design parameters and (b) simulated S_{11} of the proposed CP antenna exhibiting 59% size reduction as compared to the conventional corner-truncated square microstrip antenna.
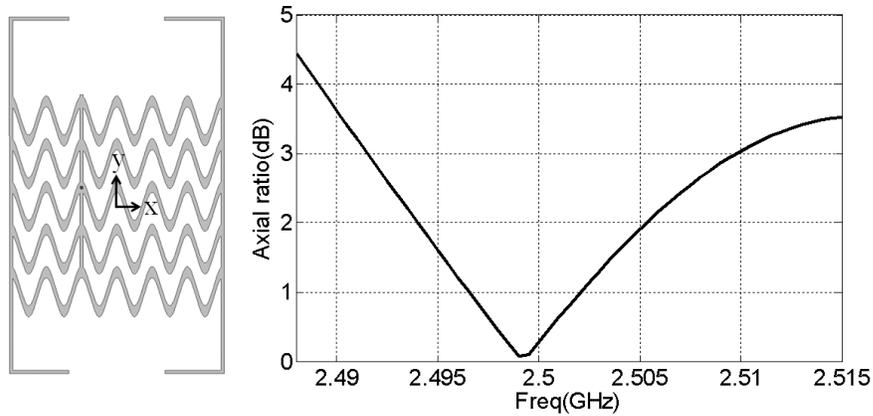
Figure 4.8: Simulated axial ratio in the broadside direction for the antenna shown in Fig. 4.7(a).

(a)   (b)
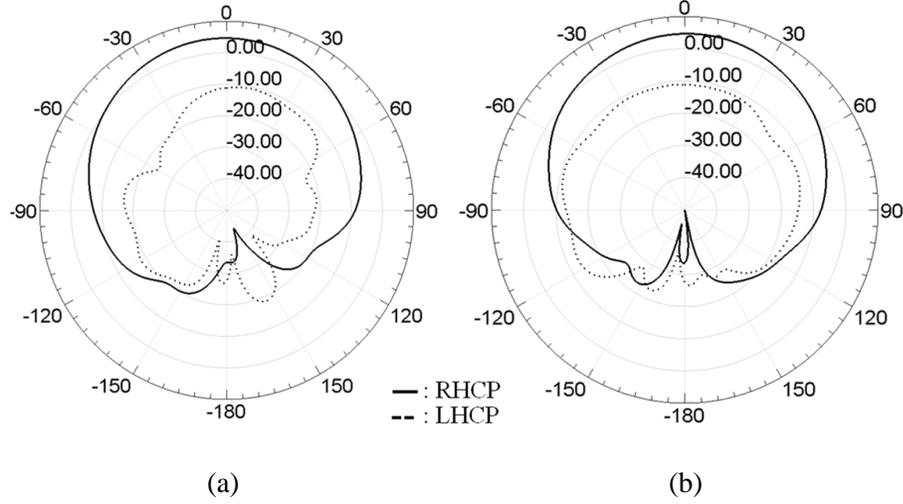
Figure 4.9: Simulated radiation patterns in two orthogonal planes of (a) xz and (b) yz-planes for the antenna shown in Fig. 4.7(a).

4.5 Additional Size Reduction by Simplifying Antenna Geometry

In this section, it is shown that additional size reduction can be achieved by modifying l_1, l_2, l_3, l_4 and the number of sinusoidal traces used in Fig. 4.7(a). The same principle described in the previous section is applied. Extending l_1 and l_2 leads to lowering both resonant frequencies. While l_3 works only for the extension of the x-directed surface current path, l_4 does for the y-directed surface current path. It is found that the number of sinusoidal traces can be reduced from 5 in Fig. 4.7(a) to 3 in Fig. 4.10(a), without affecting the dominant electric surface current paths. The space generated by eliminating 2 sinusoidal traces enables further size reduction since l_4 in Fig. 4.7(a) can be extended to $2*(l_4+l_5)+l_6$ in Fig. 4.10(a). As mentioned earlier, since l_4 in Fig. 4.7(a) is related to the y-polarized electrical length, the linear dimension of this antenna along the y-axis can be reduced from 32mm in Fig. 4.7(a) to 24mm in Fig. 4.10(a) while maintaining the antenna dimension along the x-axis as 19mm.

Fig. 4.10 shows the topology and simulated S_{11} of the proposed CP antenna exhibiting 72% size reduction compared to the conventional corner-truncated CP square

microstrip antenna. The antenna is designed to radiate with LHCP. The values of the design parameters are given by l_1=9mm, l_2=1.15mm, l_3=46.37mm, l_4=2.8mm, l_5=3.75mm, l_6=3.4mm, g=8.15mm, f_x=6.57mm, f_y=12.9mm, w_1=0.3mm and w_2=1mm. For sinusoidal meandering, the function of y=-1.3sin(8/3*x) is used. Fig. 4.11 shows the simulated axial ratio of the antenna in Fig. 4.10(a). The 3dB axial ratio bandwidth of 0.6% is computed. The antenna gain (LHCP) is about 3 dBi as shown in Fig. 4.12.

(a)   (b)
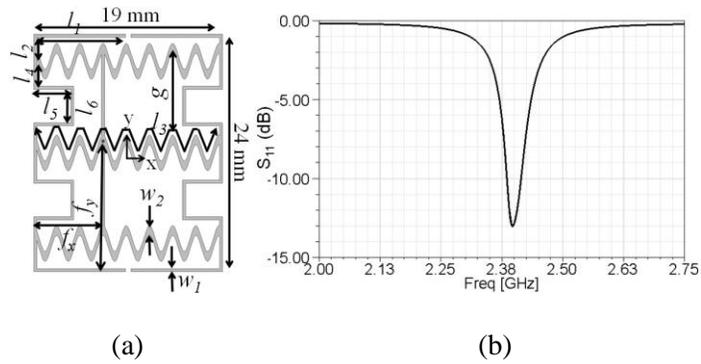
Figure 4.10: (a) Topology, design parameters and (b) simulated S_{11} of the proposed CP antenna exhibiting 72% size reduction as compared to the conventional corner-truncated square microstrip antenna.
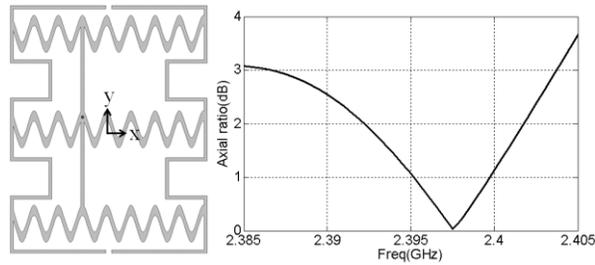
Figure 4.11: Simulated axial ratio in the broadside direction for the antenna shown in Fig. 4.10(a).

(a)   (b)
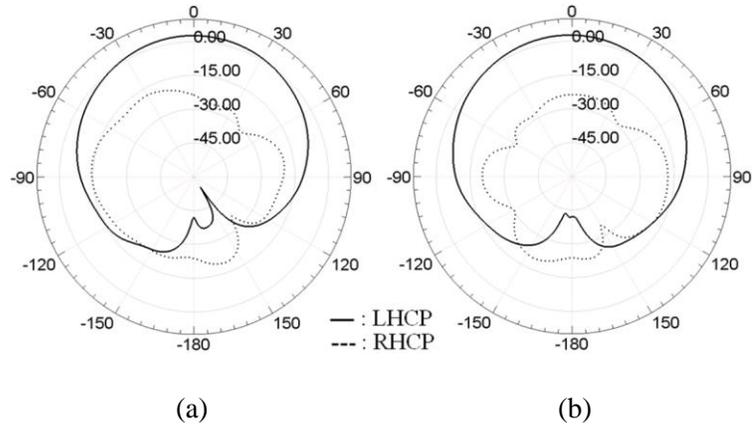
Figure 4.12: Simulated radiation patterns in two orthogonal planes of (a) xz and (b) yz-planes for the antenna shown in Fig. 4.10(a).

90

Lastly, further reducing the number of sinusoidal traces from 3 in Fig. 4.10(a) to 2 achieves more simplified antenna geometry. Fig. 4.13(a) shows that the topology and design parameters of the simplified antenna geometry exhibit a size reduction of 53% compared to the conventional corner-truncated square microstrip antenna. The effects of the design parameters shown in Fig. 4.13(a) are the same as explained in the previous sections. While l_3 and w_2 affect the resonant frequency of the x-pol, l_4 does so for the y-pol. It should be noted that while those design parameters independently affect the resonant frequencies of the two orthogonal modes, they constrain each other in some ways. For example, in order to increase l_4, w_2 should decrease when other design parameters and physical dimension of the antenna are fixed. Considering this limitation and the characteristics of the design parameters, an antenna with LHCP and a size reduction of 53% is designed and fabricated. The values of the design parameters are given by l_1=12.25mm, l_2=2.9mm, l_3=25mm, l_4=7.2mm, f_x=10.5mm, f_y=14.5mm, w_1=0.5mm and w_2=6mm. The measured S_{11} in Fig. 4.13(b) indicates an input impedance matching of better than 10 dB at the two resonant frequencies corresponding to the two orthogonal polarizations and the center frequency of 2.576GHz. This design also demonstrates that by separating the two resonant frequencies, a wider impedance bandwidth can be achieved. As shown in Fig. 4.14, the 3dB axial ratio bandwidth of 0.7% is measured. The measured radiation patterns in two orthogonal planes of the xz and yz-planes are presented in Fig. 4.15. As expected, this figure shows a smooth LHCP pattern with excellent suppression of RHCP radiation.

<center>(a)   (b)</center>
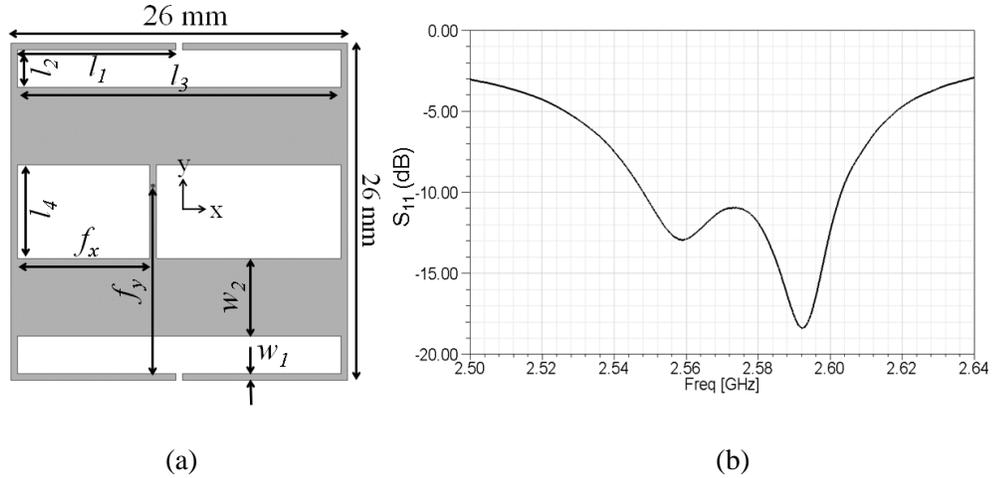
Figure 4.13: (a) Topology, design parameters and (b) measured S_{11} of the proposed CP antenna exhibiting 53% size reduction as compared to the conventional corner-truncated square microstrip antenna.
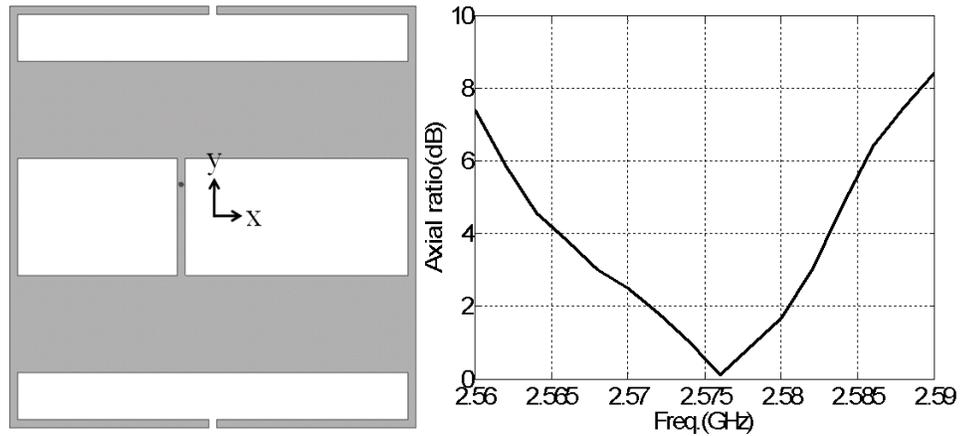
Figure 4.14: Measured axial ratio in the broadside direction for the antenna shown in Fig. 4.13(a).

Substituting l_4 in Fig. 4.13(a) by $2*l_4+4*l_5+2*l_6+l_7$ in Fig. 5.16(a) and optimizing the other design parameters still further size reduction can be achieved. An antenna with RHCP and a size reduction of 75% is designed and fabricated. The values of the design parameters are given by l_1=8.75mm, l_2=2.25mm, l_3=18mm, l_4=0.85mm, l_5=6.85mm, l_6=2.2mm, l_7=3.2mm, f_x=7.4mm, f_y=9.7mm, w_1=0.5mm and w_2=1.1mm. The measured S_{11} is shown in Fig. 4.16(b) with excellent impedance matching at two slightly different resonant frequencies. The center frequency of the antenna is 2.565GHz and its 10dB return loss bandwidth is 25MHz. As is the case with the other presented antennas,

<center>92</center>

impedance matching with a 50Ω feed probe is obtained by changing f_x and f_y. Fig. 4.17 and 4.18 show the measured axial ratio and radiation patterns of the antenna, respectively. The measured size reduction, resonant frequencies, 3dB axial ratio bandwidth, gain and radiation efficiency of the proposed antennas shown in Fig. 4.13(a) and Fig. 4.16(a) are listed in Table 4.1 and compared with the conventional corner-truncated square microstrip antenna as a reference.

(a)   (b)
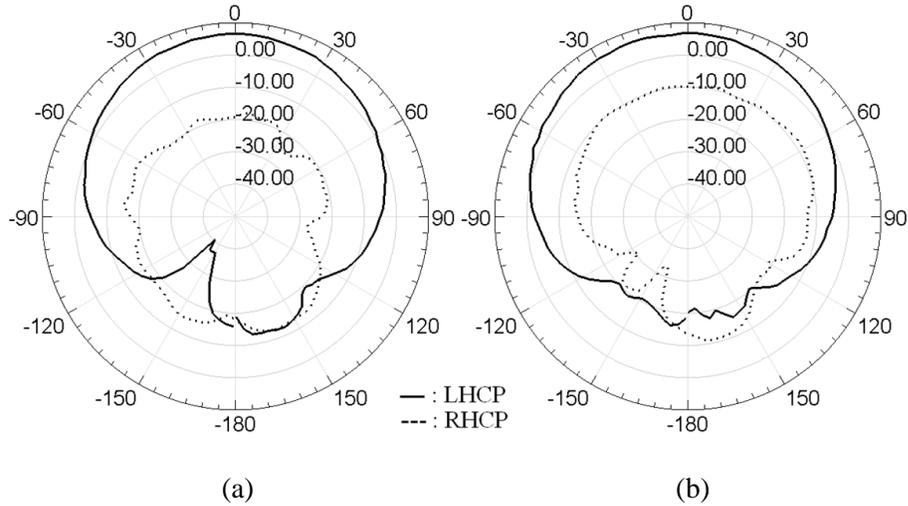
Figure 4.15: Measured radiation patterns in two orthogonal planes of (a) xz and (b) yz-planes for the antenna shown in Fig. 4.13(a).

(a)   (b)
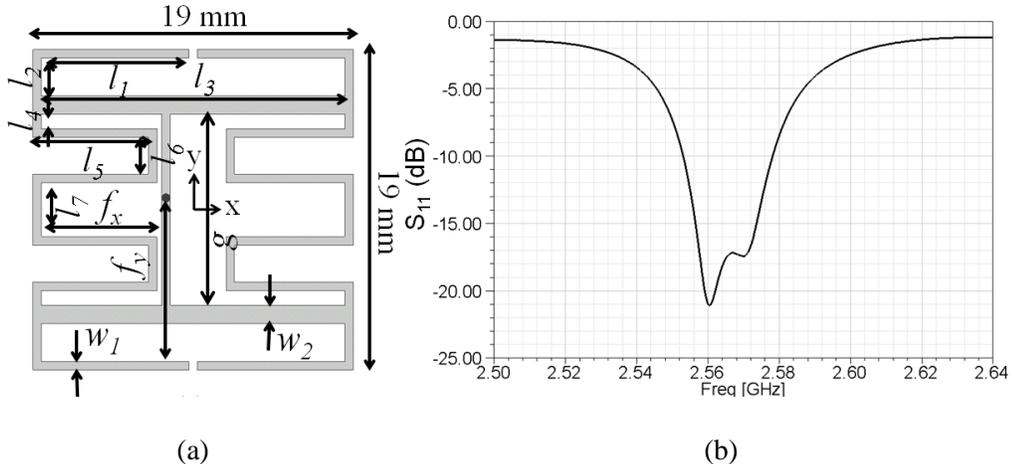
Figure 4.16: (a) Topology, design parameters and (b) measured S_{11} of the proposed CP antenna exhibiting 75% size reduction as compared to the conventional corner-truncated square microstrip antenna.
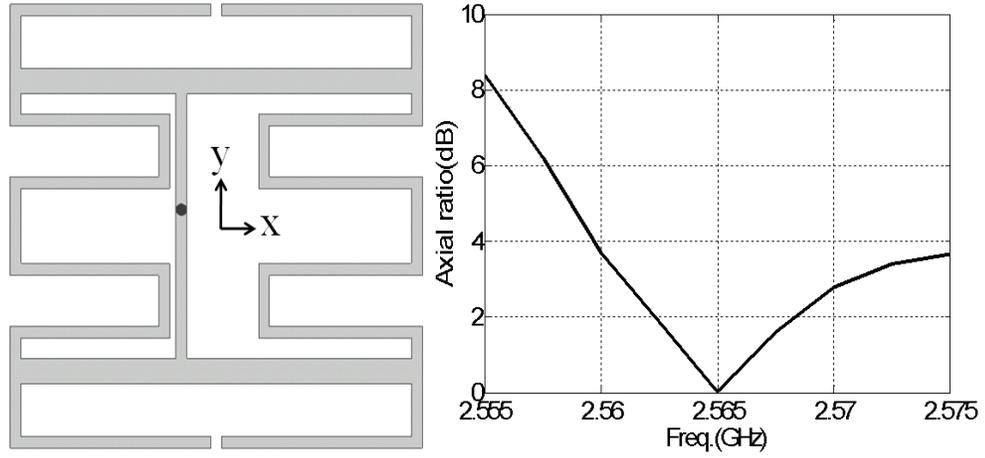
Figure 4.17. Measured axial ratio in the broadside direction for the antenna shown in Fig. 4.16(a).
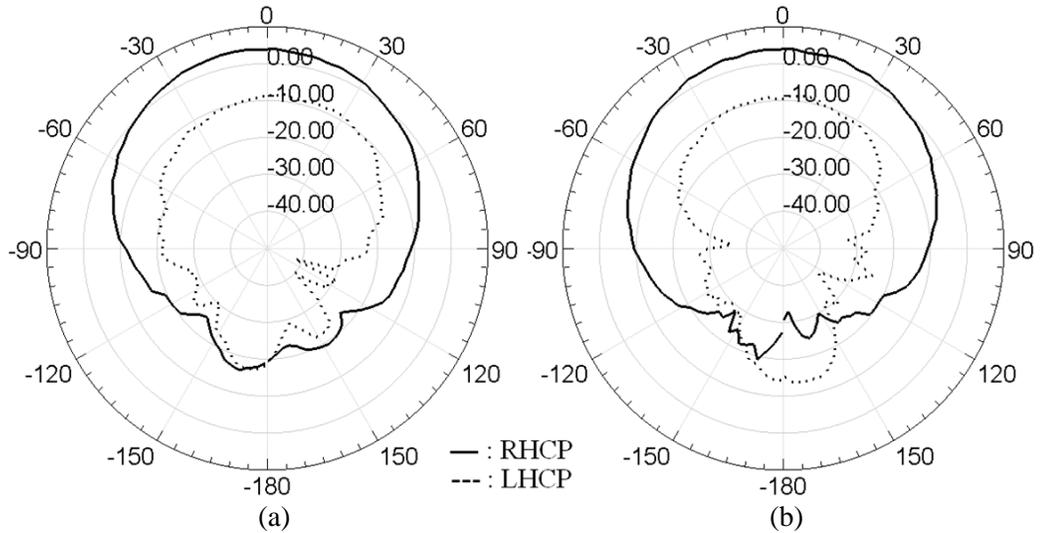
Figure 4.18: Measured radiation patterns in two orthogonal planes of (a) xz and (b) yz-planes for the antenna shown in Fig. 4.16(a).

TABLE 4.1
MEASUREMENT RESULTS OF THE PROPOSED ANTENNAS IN FIG. 4.13(A) AND 4.16(A)

Size reduction (%)	Resonant Freq. (GHz)	Pol.	3dB Axial Ratio Bandwidth (%)	Gain (dBi)	Radiation Efficiency (%)
0 % (Reference)	2.56	RHCP	1.7	7.8	97
53%	2.576	LHCP	0.7	6.8	86
75%	2.565	RHCP	0.5	4.1	54

Chapter 5

Design of Compact Co-Located Polarization/Pattern Diversity Antennas Using a New Class of Microstrip Antennas

Compact co-located planar polarization/pattern diversity antennas using a new class of microstrip antennas are presented. The sizes of the proposed diversity antennas and envelop correlations between two radiation patterns of two antenna elements composing each diversity antenna, are discussed.

5.1 Introduction

In the next generation of mobile communication systems there is a stringent demand for high speed and high quality data transmission of the mobile terminals. This makes Multiple-Input Multiple-Output (MIMO) technology attractive for its excellent performance in channel capacity without occupying extra spectrum and radiating power [12]. MIMO systems have emerged as a very interesting strategy to increase the capacity of wireless systems in rich scattering environments [82], [83]. Traditionally, the MIMO systems employ several transmit and receive antennas at each end of the radio link, and in order to achieve a high capacity, different signal paths between them should be uncorrelated. The MIMO gains are mainly due to the fact that a rich scattering environment provides independent transmission paths (multi-channel) from each transmit

antenna to each receive antenna. In the MIMO systems, antenna diversity is a well-known technique to enhance the performance of wireless communication systems by reducing the multipath fading and co-channel interference [13], [14]. The idea is based on gathering multiple uncorrelated copies of the multipath signals and their combining. Using antenna diversity reception increases the radio link signal level and reduces the effect of the multipath fading [13], [26].

It is well known that there are five different types of diversity techniques that can be used for the increased signal reception: spatial, temporal, polarization, frequency, and pattern. Of these, only spatial, polarization and pattern make for a practical implementation in WLAN antenna systems. Spatial diversity implies multiple antennas with some wavelength separations. Since the desired long separation among the diversity antennas makes the size of the diversity systems very bulky, polarization and pattern diversity are most commonly used. Polarization diversity uses different orthogonally-polarized field captures and pattern diversity implies different directed radiation patterns in space. Large volume that antennas in such diversity systems occupy remains a critical problem in implementing small wireless platforms. In the previous approaches, the reductions in antenna size have been achieved for individual antennas [26]–[28]. However, compact co-located diversity antennas have not been well studied. The current approach to achieve antenna diversity is based on placing two or more individual compact antennas in optimized positions that provide low envelope cross-correlation coefficients. This approach is good but the overall volume that the antennas occupy increases directly with their number and becomes too large for compact wireless applications.

With low-cost fabrication and low-profile structure, microstrip antennas are widely used in mobile communication systems [84]. However, suffering from the disadvantages of their large lateral dimension and limited configurations of polarization and pattern, the antennas are not easily applied for the diversity systems. A conventional way to design compact diversity antennas using the microstrip antennas is that without increasing the number of antenna elements one microstrip antenna is shared by two orthogonal feeds, leading to polarization diversity [85]-[88]. In [85], the size of such antennas is reduced by inserting a number of slits at the perimeter of a square patch. However, since geometric modifications of such antennas affect both orthogonal modes simultaneously, poor individual tunability is unavoidable. Recently, another way employing the microstrip antenna to achieve the compact diversity antennas was proposed [89], [90]. In [89], using a circular patch and hybrid feed network, two degenerate modes, TM_{11} and TM_{01}, are obtained at an overlapped frequency range. While TM_{11} mode reveals good broadside radiation patterns, TM_{01} mode shows monopole-like radiation patterns, leading to pattern diversity. But, the complexity in the feed network limits the extent of the antenna's applications.

In this work, we present a new class of microstrip antennas to be able to be applied for the design of compact co-located polarization and pattern diversity. Taking advantage of the geometry and field distributions of the proposed microstrip antenna, compact size and low envelop correlation are achieved for both types of diversity antennas. In Section 5.2, design and performance characteristics of the proposed microstrip antenna are presented. In Section 5.3, novel compact polarization and pattern

diversity antennas employing the proposed microstrip antenna element are proposed and their envelop correlation and diversity gain are discussed.

5.2 A New Class of Microstrip Antennas for Compact Diversity Antenna Systems

This section presents a new type of microstrip antenna whose geometry enables the size reduction of polarization and pattern diversity antennas with low envelop correlation between radiation patterns of two antenna elements composing the diversity antennas. The basic idea is to split the conventional microstrip antenna into two bodies by inserting an open area and shorting plates in its middle, as shown in Fig. 5.1(a). Fig. 5.2 shows voltage and current distributions on the conventional $\lambda/2$ microstrip antenna with x-polarized radiation on an infinite ground plane. In the middle of the antenna, the voltage is at minimum (=zero) and the current is at maximum. In the proposed antenna, although the open area exists in its middle, the shorting plates connected to the ground enable the zero voltage and maximum current. In addition, strong magnetic coupling between two shorting plates provides continuous transitions between current distributions of the two split bodies, which is essential to achieve broadside radiation pattern. The second element on the right side in Fig. 5.1(a) can be considered as a magnetically coupled parasitic element. It should be noted that while a shorted $\lambda/4$ microstrip antenna without the parasitic element (PIFA) provides the same resonant frequency as the conventional $\lambda/2$ microstrip antenna, it cannot achieve broadside radiation pattern. Fig. 5.1(b) shows the miniaturized bow-tie version of the proposed microstrip antenna, which will be used to design the proposed diversity antennas in the next section.

(a)   (b)
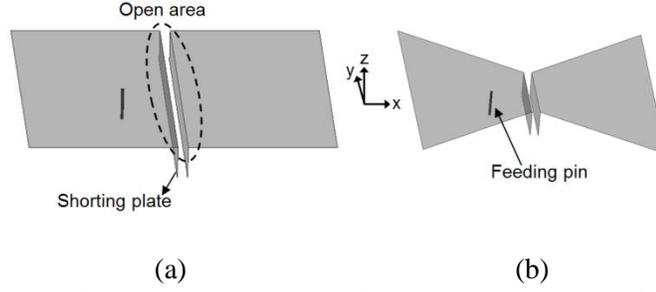
Figure 5.1: (a) Proposed microstrip antenna with an open area in its middle and (b) bow-tie version of the proposed microstrip antenna on the infinite ground plane.

(a)   (b)
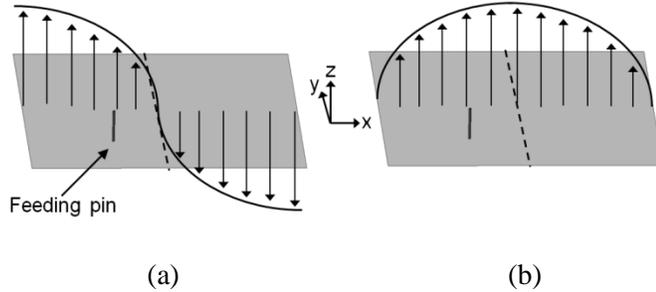
Figure 5.2: Distributions of (a) voltage and (b) current on the $\lambda/2$ microstrip antenna with x-polarized radiation on the infinite ground plane.

Fig. 5.3 shows geometry and design parameters of the proposed bow-tie microstrip antenna on a finite ground plane. Impedance matching to a 50ohm feed line is obtained by controlling g_2 that is the distance between the feeding plate and shorting plate on the right side, similar to the conventional $\lambda/2$ microstrip antenna. The values of design parameters are given by L_1=500mm, L_2=182mm, w_1=500mm, w_2=204mm, w_3=65mm, w_4=70mm, g_1=20mm, g_2=10mm and h=60mm. Fig. 5.4 shows simulated S_{11} of the proposed antenna. Two resonant frequencies are observed and Fig. 5.5 shows current distributions at the two resonant frequencies. At the first resonant frequency, horizontal currents on a trapezoidal top plate are in the opposite direction to horizontal currents on the other top plate, leading to the cancellation of the radiated fields from the top plates. On the other hand, at the second resonant frequency, the horizontal current on both top plates has a same direction. As a result, while the antenna has omnidirectional radiation pattern at the first resonant frequency (denoted by 'PIFA operation'), it has broadside

99

radiation pattern at the second resonant frequency (patch operation), as shown in Fig. 5.6. In this work, design parameters are optimized for the patch operation at the second resonant frequency. Fig. 5.7 shows simulated S_{11} as a function of g_1. As g_1 increases, the second resonant frequency decreases due to the increase in the antenna volume under the fixed other design parameters. However, antenna bandwidth also decreases. This is because of the significant drop in the magnetic coupling between two shorting plates related to stored magnetic energy responsible for antenna bandwidth.
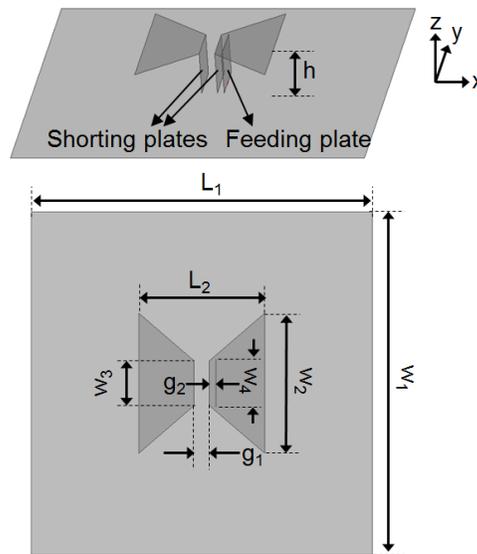
Figure 5.3: Geometry and design parameters of the bow-tie version of the proposed microstrip antenna with an open area in its middle.
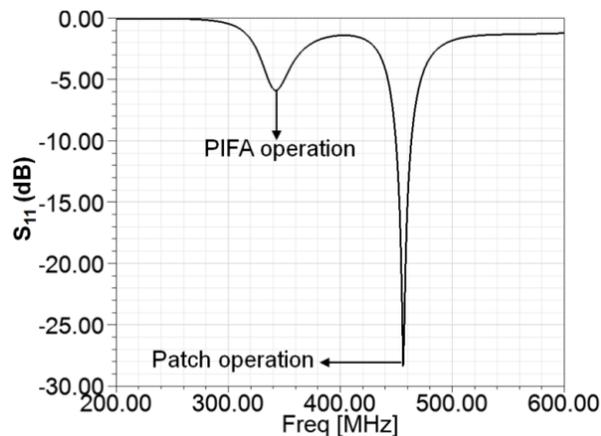
Figure 5.4: Simulated S_{11} of the proposed bow-tie microstrip antenna shown in Fig. 5.3.

(a)   (b)
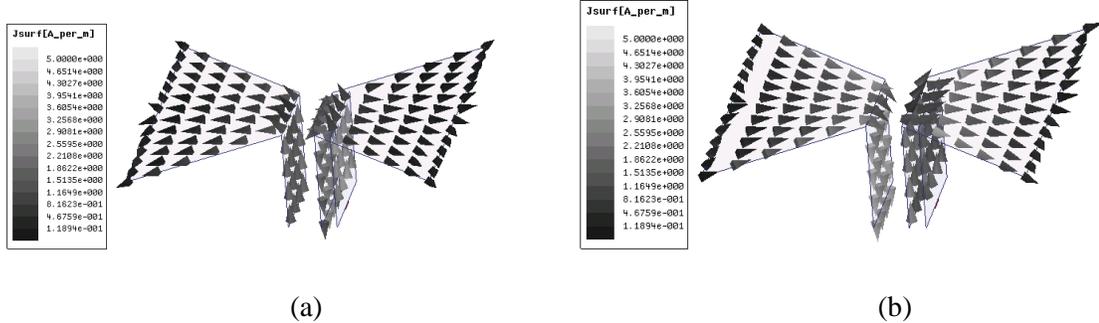
Figure 5.5: Current distributions of the proposed antenna in Fig. 5.3 at (a) 342MHz and (b) 456MHz.

(a)   (b)
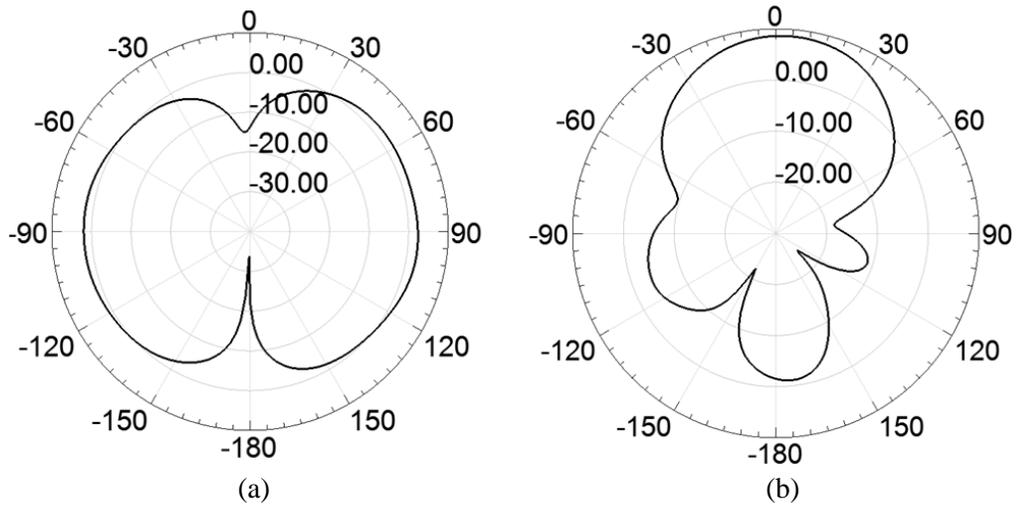
Figure 5.6: Simulated radiation patterns of the proposed bow-tie microstrip antenna on E-plane (xz-plane) at two resonant frequencies, corresponding to (a) PIFA and (b) patch operation shown Fig. 5.4.
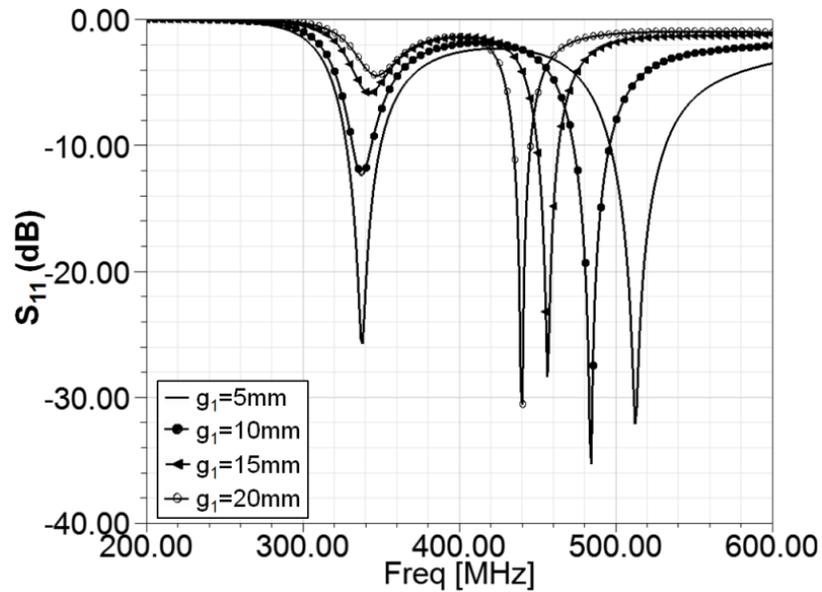
Figure 5.7: Simulated S_{11} of the proposed bow-tie microstrip antenna versus g_1.

5.3 Compact Co-Located Diversity Antennas

5.3.1 Design of Polarization Diversity Antenna

The aforementioned open area in the proposed bow-tie microstrip antenna provides a great advantage for the size reduction of diversity antennas because a part of another antenna can be placed in the open area. This section presents a novel compact polarization diversity antenna using the proposed microstrip antenna. The proposed polarization diversity antenna consists of two antenna elements with different linear polarizations. Fig 5.8 shows the two antenna elements, the proposed bow-tie microstrip antenna with x-pol and conventional bow-tie microstrip antenna with y-pol. As mentioned above, the metallic trace in the middle of the conventional antenna shown in Fig. 5.8(b) can be placed in the open area of the proposed microstrip antenna shown in Fig. 5.8(a). Fig. 5.9 shows geometry and design parameters of the proposed polarization diversity antenna, which is a combination of two antenna elements shown in Fig. 5.8. In Fig. 5.8(b), while for the desired patch operation, the position of the feeding plate connected to 'port2' must be around the center of the microstrip antenna, its position is moved up to an open end using a meandered coplanar waveguide (CPW) line. This minimizes the undesired coupling between two feeding plates connected to 'port1' and 'port2', effectively maintaining the near-center feeding position.

The values of the design parameters are given by a_{pol}=180mm, b_{pol}=160mm, c_{pol}=180mm, d_{pol}=63.3mm, e_{pol}=10.6mm, f_{pol}=1.8mm, g_{pol}=53.2mm, h_{pol}=60mm, i_{pol}=14mm, j_{pol}=40mm, k_{pol}=5mm and l_{pol}=83.8mm. Fig. 5.10 shows simulated S_{11}, S_{21} and S_{22} of the proposed polarization diversity antenna. Resonant frequencies of the two antenna elements are merged to 454MHz at which the isolation between two ports (S_{21}) is

-23.3dB. In Fig. 5.11, measured S parameters show good agreement with the simulated results. 10-dB return loss bandwidth of 2.3% is derived at 454MHz. The area of the proposed diversity antenna is just 29.7% of the area of the conventional microstrip antenna with the dimension of $\lambda/2 \times \lambda/2$. A great advantage of this antenna configuration is highly independent controllability of the two resonant frequencies corresponding to the two antenna elements. As mentioned in Section 5.1, while the two antenna elements in most of the dual polarized miniaturized microstrip antennas share a single top plate, each antenna element in the proposed diversity antenna has its individual top plate. As a result, the two antenna elements are completely physically separated and thus the change in the geometry of an antenna element has a minimal impact on the resonant frequency of other antenna element. Fig. 5.12 shows simulated S_{11}, S_{21} and S_{22} of the proposed polarization diversity antenna with 5mm increased and decreased l_{pol}. As expected, while the resonant frequency corresponding to the antenna element connected to 'port2' is slightly shifted, the other resonant frequency related to 'port1' doesn't change. This excellent characteristic can be utilized to design compact tunable diversity antennas.

(a)   (b)
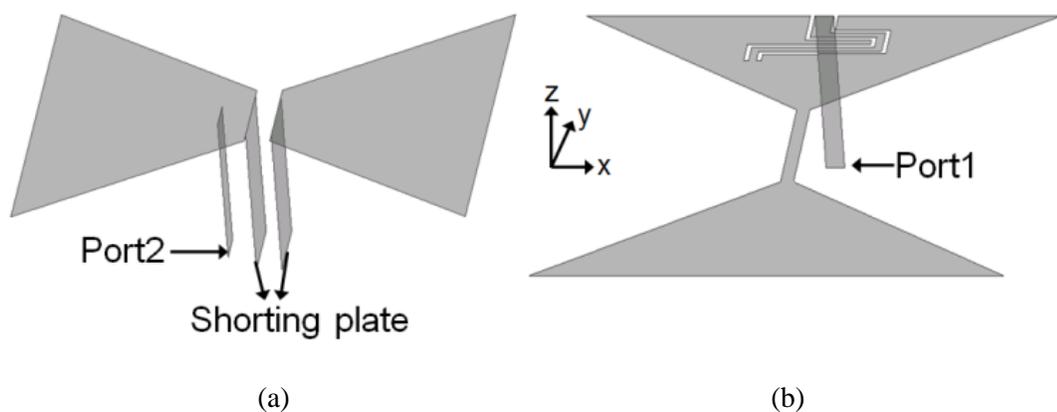
Figure 5.8: (a) Proposed bow-tie microstrip antenna with x-pol and (b) conventional bow-tie microstrip antenna with y-pol.

Figure 5.9: Geometry and design parameters of the proposed polarization diversity antenna.
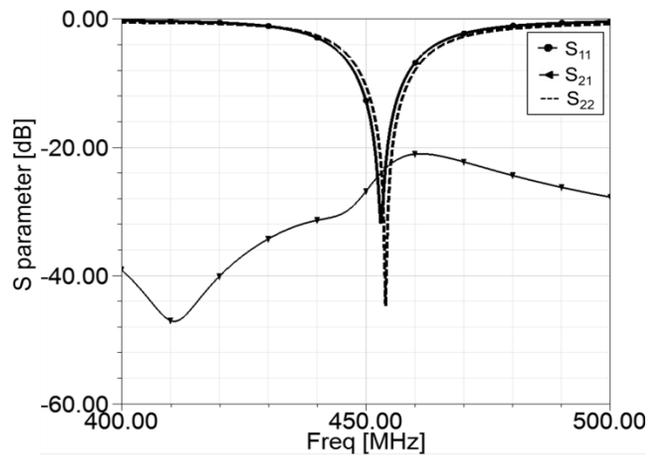
Figure 5.10: Simulated S_{11}, S_{21} and S_{22} of the proposed polarization diversity antenna.

Figure 5.11: Measured S_{11}, S_{21} and S_{22} of the proposed polarization diversity antenna.

(a)   (b)

Figure 5.12: Simulated S_{11}, S_{21} and S_{22} of the proposed polarization diversity antenna with 5mm (a) increased and (b) decreased l_{pol}.

The diversity gain is a function of antenna efficiency, envelope-correlation (ρ_e), and the relative signal strength levels between the two received signals [88]. In order to achieve a reduction in signal fading and thus a higher level of diversity gain, the following two conditions must be satisfied [13]:

$$\rho_e < 0.5 \text{ and } P_1 \approx P_2 \tag{4.1}$$

where P_i is the average signal strength received at each branch of the antenna and ρ_e is envelope-correlation. The envelop correlation can be obtained using radiation patterns or S-parameters which are described in detail in [26] and [91], respectively. In this work, the envelop correlation is calculated from S-parameters by using

$$\rho_e = \frac{\left| S_{11}^* S_{12} + S_{21}^* S_{22} \right|^2}{(1 - (|S_{11}|^2 + |S_{21}|^2))(1 - (|S_{22}|^2 + |S_{12}|^2))} \tag{4.2}$$

The formula assumes uniformly distributed radio channel and lossless antennas [92]. Based on [93], as the measured total efficiency of the proposed antennas is high over the operating impedance bandwidth, the effect of the losses on the diversity performance is assumed to be small. Effective diversity gain (EDG) can be obtained by using a selection combining criteria with maximum apparent diversity gain at 1% outage rate [94]. The EDG is calculated by multiplying the diversity gain with the radiation efficiency of the most efficient antenna element

$$EDG = e_{rad} \cdot 10 \sqrt{1 - |\rho|^2} \qquad (4.3)$$

where the relation between the complex cross-correlation (ρ) and envelop correlation (ρ_e) is $|\rho|^2 \approx \rho_e$.

Fig. 5.13 and 5.14 shows simulated or measured radiation efficiency, envelop correlation and EDG over the fractional 3-dB return loss bandwidth of the proposed bow-tie microstrip antenna. It is found that the measured envelop correlation (ρ_e) between radiation patterns of the two antenna elements is lower than -30dB over the 10-dB return loss bandwidth of the proposed microstrip antenna. Fig. 5.15 shows radiation patterns on E-planes of the two bow-tie microstrip antennas. For both the antennas, desired broadside radiation patterns and the ratio of co- to cross pol with more than 10dB are observed.
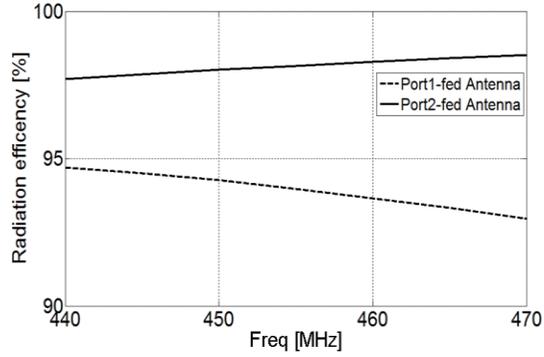
Figure 5.13: Simulated radiation efficiency of two antenna elements in the proposed polarization diversity antenna.
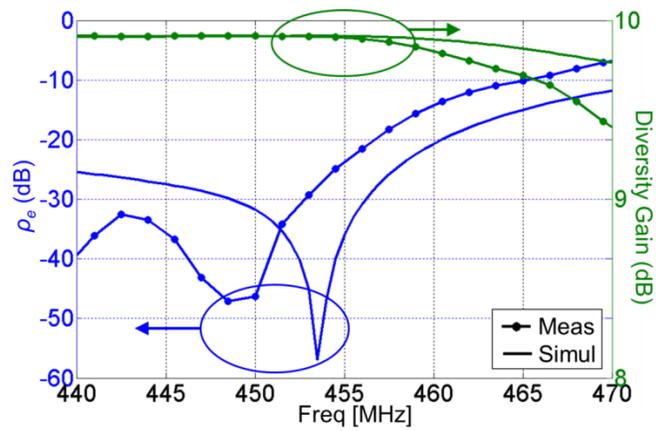
Figure 5.14: Envelop correlation (ρ_e) between radiation patterns of two antenna elements in the proposed polarization diversity antenna and diversity gain.

(a)　　　　　　　　　　　(b)
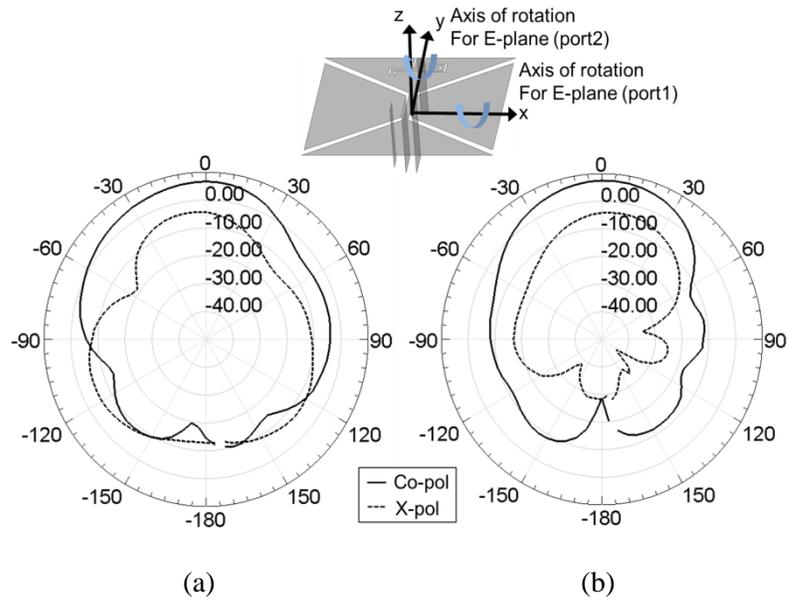
Figure 5.15: Measured radiation patterns on E-planes of two bow-tie microstrip antennas: (a) Port1: ON and Port2: OFF (50Ω terminated) and (b) Port1: OFF (50Ω terminated) and Port2: ON.

5.3.2 Design of Pattern Diversity Antenna

This section presents a novel compact pattern diversity antenna using the proposed bow-tie microstrip antenna. The proposed pattern diversity antenna consists of the proposed bow-tie microstrip antenna and a folded monopole antenna placed in the aforementioned open area of the proposed microstrip antenna. The broadside radiation pattern of the proposed bow-tie microstrip antenna and omnidirectional radiation pattern of the folded monopole antenna achieve radiation pattern diversity. Fig. 5.16 shows the folded monopole antenna and proposed bow-tie microstrip antenna. The folded monopole antenna is based on the shorted $\lambda/2$ transmission line resonator. For the selection of the positions of shorting and feeding plates in the folded monopole antenna, particular attention must be paid to minimize the undesired radiation from the horizontal currents on the top plate [17]. Impedance matching to a 50Ω feed line can be obtained by tuning e_{pat} and f_{pat} since a short segment (e_{pat}) can work as an impedance transformer [95]. Fig. 5.17 shows the geometry and design parameters of the proposed pattern diversity antenna. The values of the design parameters are given by a_{pat}=200mm, b_{pat}=70mm, c_{pat}=180mm, d_{pat}=30mm, e_{pat}=75mm, f_{pat}=8mm, g_{pat}=7mm, h_{pat}=60mm and i_{pat}=70mm.

At the resonant frequency of the $\lambda/2$ folded monopole antenna, voltage is maximum and current is minimum in the middle of the antenna, and thus input impedance at the node in the middle toward the proposed bow-tie microstrip antenna is ideally infinite. This property can provide low envelop correlation to the proposed pattern diversity antenna. However, it should be noted that parasitic in-plane coupling between top plates of two antenna elements causes a small increase in the envelop correlation. Fig. 5.18 shows simulated S_{11}, S_{21} and S_{22} of the proposed polarization diversity antenna. Resonant

frequencies of the two antenna elements are merged close to 455MHz at which the isolation between two ports (S_{21}) is -18.6dB. In Fig. 5.19, measured S parameters show good agreement with the simulated results. The area of the proposed diversity antenna is just 32% of the area of the conventional microstrip antenna with the dimension of λ/2 X λ/2. While the folded monopole antenna is a type of broadband monopole antennas, the microstrip antenna is inherently a narrowband antenna [95]. However, it is well known that the narrow bandwidth of the microstrip antenna can be enhanced by using broadband feeding structures such as the L-shaped probe feeding technique [96], proximity coupling by etching an H-shaped slot [97], and the capacitive feed technique [98]. For broadband diversity applications, the same approaches can be also utilized for the proposed bow-tie microstrip antenna. But, applying those techniques for the proposed antenna is out of the scope of this work. Fig. 5.20 and 5.21 show simulated or measured radiation efficiency, envelop correlation and EDG over the 3-dB return loss bandwidth of the proposed bow-tie microstrip antenna. It is found that the measured envelop correlation (ρ_e) between radiation patterns of the two antenna elements is lower than -30dB over the 10-dB return loss bandwidth of the proposed microstrip antenna. Fig. 5.22 shows measured radiation patterns on E-planes of the folded monopole antenna and proposed bow-tie microstrip antenna. For each antenna elements, desired omnidirectional or broadside radiation patterns are observed.

(a)   (b)
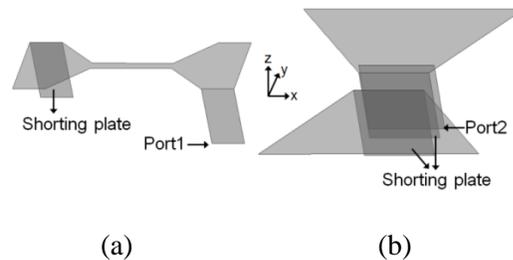
Figure 5.16: (a) Folded monopole antenna with omnidirectional radiation pattern and (b) proposed bow-tie microstrip antenna with broadside radiation pattern.
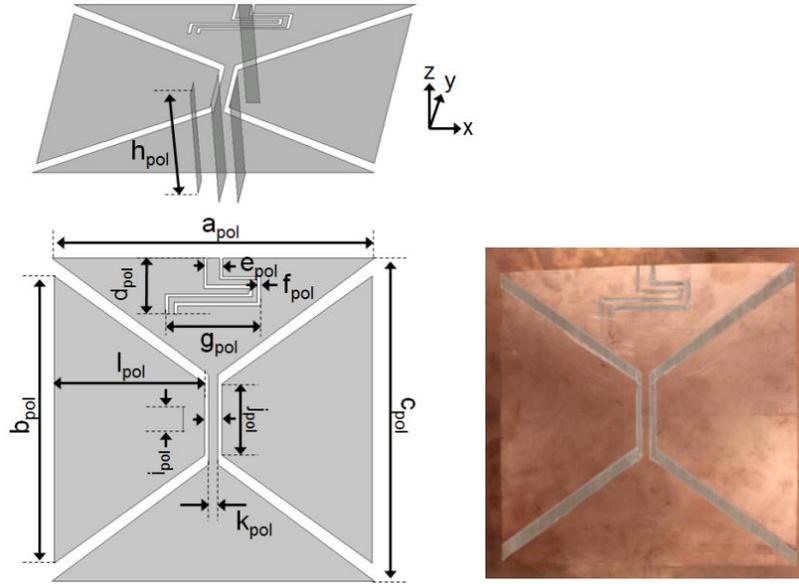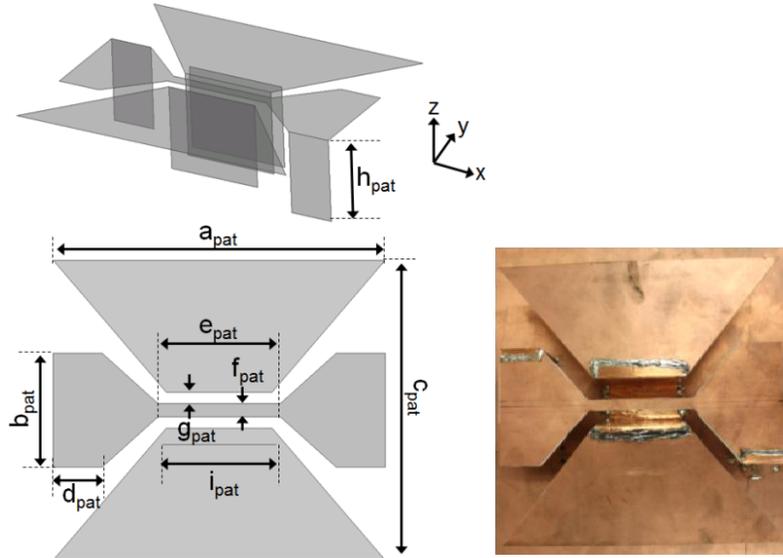
Figure 5.17: Geometry and design parameters of the proposed pattern diversity antenna.
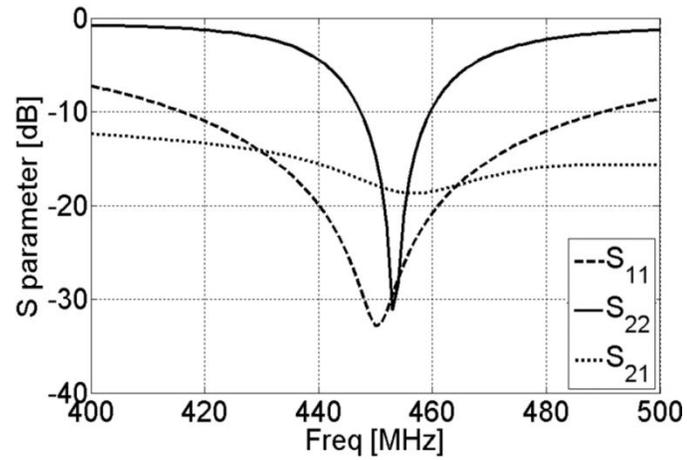
Figure 5.18: Simulated S_{11}, S_{21} and S_{22} of the proposed pattern diversity antenna.

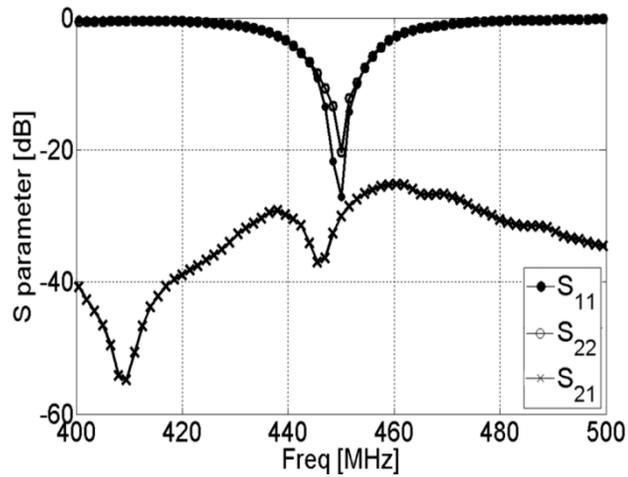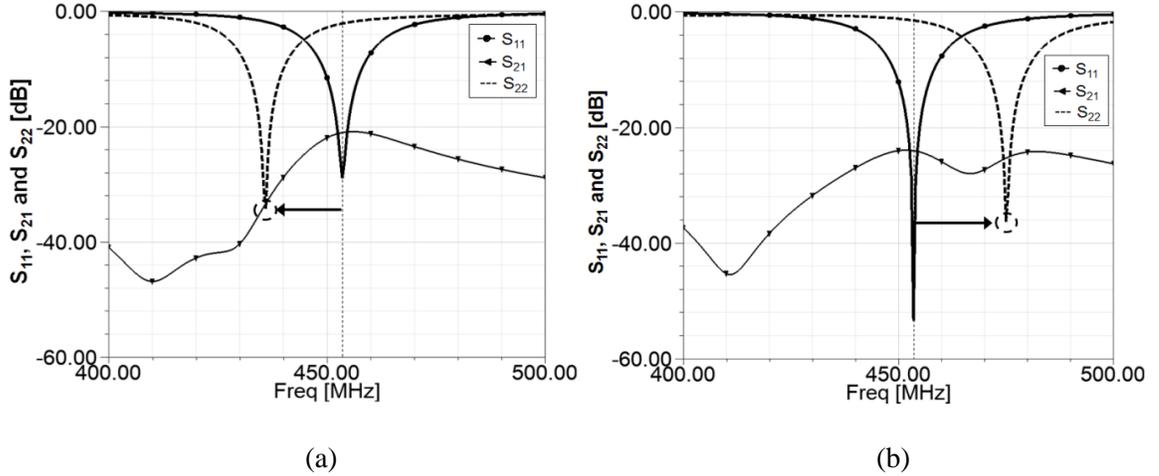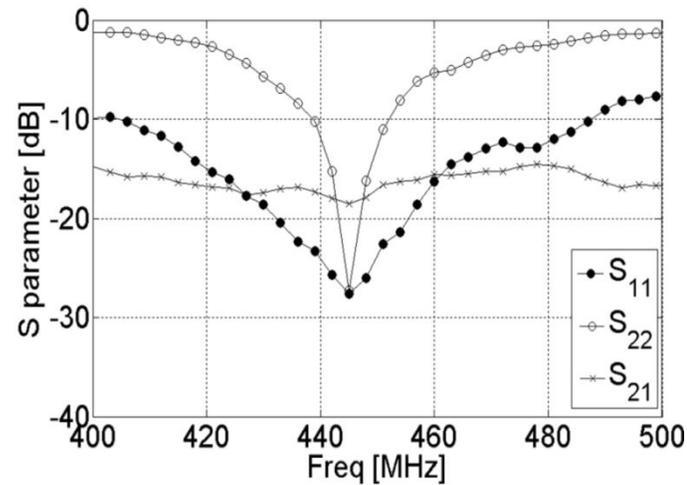Figure 5.19: Measured S_{11}, S_{21} and S_{22} of the proposed pattern diversity antenna.
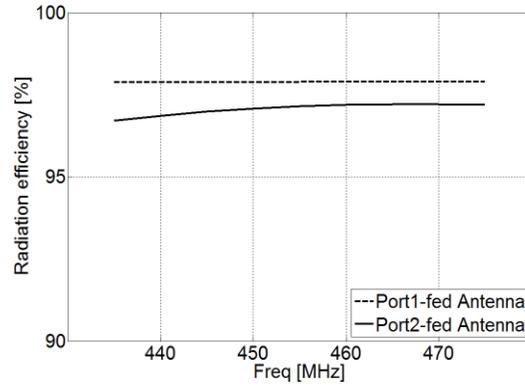
Figure 5.20: Simulated radiation efficiency of two antenna elements in the proposed pattern diversity antenna.
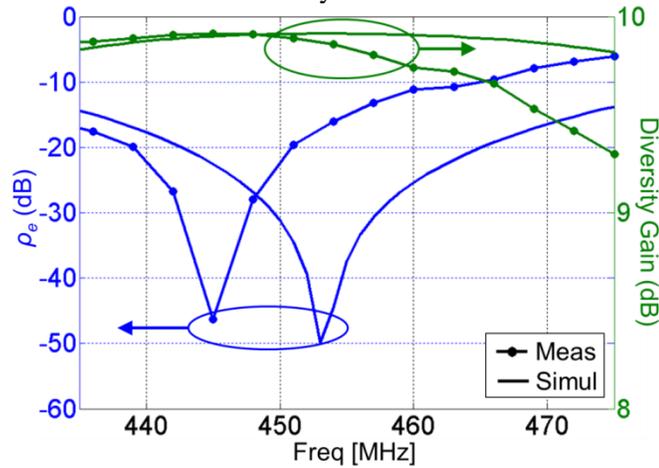
Figure 5.21: Envelop correlation (ρ_e) between radiation patterns of two antenna elements in the proposed pattern diversity antenna and diversity gain.

(a)   (b)
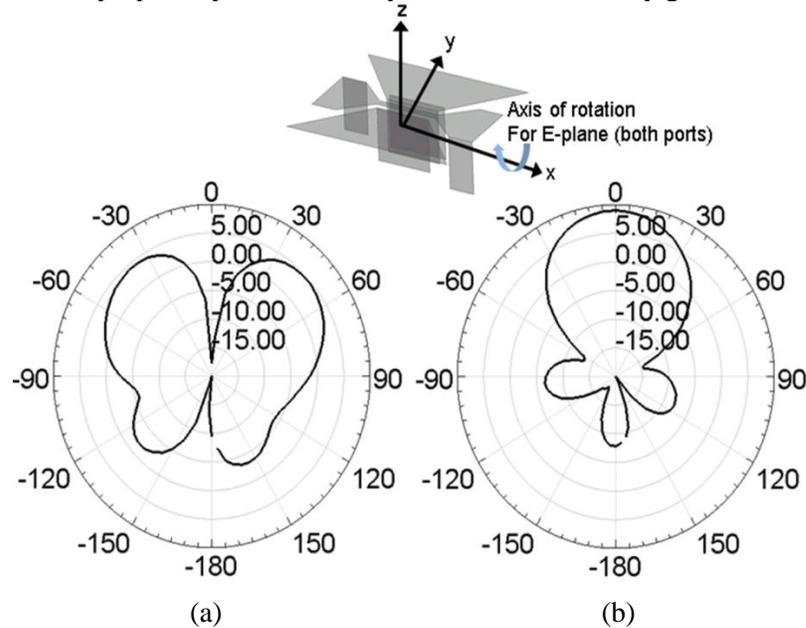
Figure 5.22: Measured radiation patterns on E-planes of the folded monopole antenna and proposed bow-tie microstrip antenna: (a) Port1: ON and Port2: OFF (50Ω terminated) and (b) Port1: OFF (50Ω terminated) and Port2: ON.

111

Chapter 6

Conclusion and Future Work

In this chapter, the contributions of this dissertation are summarized. Ideas for future work are suggested as well.

6.1 Conclusion

From the fundamental limit of antennas, applying antenna miniaturization techniques for the antennas comes at the expense of the antenna performance. This dissertation addresses the limit of the conventional approaches, and proposes new approaches to achieve the antennas with smaller form factor and better performance in terms of radiation efficiency, polarization purity, radiation pattern and bandwidth. The poor radiation characteristics of the conventional miniaturized antennas are related to the use of the conventional transmission-line-based resonant element. In order to fit the geometry of the antenna into the small area, the utilization of meandering and thin metallic traces causes poor polarization purity and the increase in ohmic and proximity losses. In addition, a practical assumption of the small antennas is to use a small ground plane to mount the antennas. Applying the conventional approaches for the antenna on the small ground plane causes the serious distortion in radiation pattern. Therefore, new antenna miniaturization techniques and topologies are developed to preserve the behavior

and radiation characteristics of originally-sized antenna. The contributions of this dissertation include:

- For short monopole antennas with the height of $\lambda/45$ and the lateral dimension of $\lambda/16$, a technique to enhance radiation efficiency and polarization purity is introduced. The technique utilizes an inductively coupled capacitively loaded structure without requiring the lossy meandered metallic traces. The performance of the proposed antenna is compared to that of an ordinary inverted F antenna and a more recent low profile vertically polarized antenna (LMMMA). It is shown that the gain of ICCLMA is 9 dB and 4 dB higher than that of the conventional inverted-F antenna and the LMMMA, respectively.

- For extremely short monopole antennas with the height of $\lambda/300$ and the lateral dimension of $\lambda/100$, techniques utilizing two in-phase radiating elements and a low-loss phase shifter are introduced. The proposed antenna architecture is composed of two in-phase radiating vertical elements connected to two inductors between which a capacitive top load is connected to achieve the desired resonant condition. The two vertical elements act effectively as a monopole having increased height. It is also shown that the gain of the antenna can be increased monotonically by increasing the quality factor (Q) of the phase shifter. High Q air-core inductors that can be accommodated in the extremely small monopole antenna are designed and incorporated in the phase shifter to achieve gain enhancement of 16.5dB.

- Techniques are proposed to realize omnidirectional radiation pattern of low profile antennas on the small ground plane. It is found that the conventional miniaturization technique causes the distortion in the radiation pattern of the antennas on the small ground plane, leading to the significant drop in signal reception at desired angle. As an approach, a balanced configuration of low profile monopole antennas is introduced. This reduces the effects of the size and shape of the ground plane on the radiation pattern and resonant frequency, similarly to dipole antennas. In addition, the importance of suppressing the radiation from the electric currents with undesired polarizations is emphasized. It is shown that the proposed antenna topology well suppresses the radiation from horizontal electric currents on the top plate of low profile monopole antennas, achieving desired omnidirectional radiation pattern and polarization purity.

- A broadbanding technique is introduced for low profile omnidirectional antennas. Design approach is based on manipulating the topologies of a low profile folded monopole antenna and capacitively coupled parasitic elements to achieve omnidirectional radiation pattern and fractional 10-dB return loss bandwidth of 43% with the dimensions of $0.2\lambda_{LF}$ X $0.2\lambda_{LF}$ X $0.06\lambda_{LF}$ where λ_{LF} is the wavelength at the lowest frequency of the operating band. Unlike inductively coupled parasitic elements, the capacitively coupled parasitic elements can be positioned in the middle of the folded monopole antenna where maximum electric field is excited. This enables the cancellation of radiated fields from electric currents in the horizontal plane of the proposed

antenna, which is essential to achieve vertically polarized omnidirectional radiation.

- A novel approach for the miniaturization of circularly polarized patch antennas is presented. This enables a size reduction of as high as 75%, compared to a conventional corner-truncated circularly polarized patch antenna. The proposed design procedure consists of a number of intermediate steps, each of which produces antenna miniaturization as well as the desired polarization and impedance matching properties. It is shown that two resonant frequencies corresponding to two near-degenerate orthogonal modes can be tuned independently to produce a dual band antenna with two orthogonal polarizations.

- A new class of microstrip antennas is introduced to design compact polarization/pattern diversity planar antennas. Although the proposed diversity antennas consists of two antenna elements with different polarizations or radiation patterns, their areas are just about 30% of the area of the conventional microstrip antenna with the dimension of $\lambda/2 \times \lambda/2$. In addition, for both types of the proposed diversity antennas, the envelop correlations between radiation patterns of the two antenna elements composing each diversity antenna are lower than -30dB over the 10-dB return loss bandwidth of the proposed microstrip antenna.

6.2 Suggestions for Future Work

6.2.1 Broadband Impedance Matching of Moderate Gain Extremely Short Antennas

In Section 2.2, it is shown that the proposed extremely small antenna with the height of $\lambda/300$ and the lateral dimension of $\lambda/100$ exhibits 16.5 dB higher gain than the conventional spiral-shape inverted F antenna. This significant gain enhancement enables the increase in the fundamental figure of merit defined by the product of antenna bandwidth and radiation efficiency. If the antenna bandwidth can be enhanced maintaining this gain enhancement, the range of the applications of the proposed antenna would be greatly extended. One approach to this goal is the utilization of a broadband impedance matching network. Fig. 6.1 shows antenna gain with and without considering impedance mismatch factor to a feed (η_{imf}). It is found that while the fundamental antenna gain (G_a) is a slow varying function of frequency, narrow impedance matching limits the actual antenna gain ($\eta_{imf} * G_a$). For example, at 25.1 MHz (just 0.5MHz far from the center frequency (25.6MHz)) the gain drop reaches 20dB. Recently, applying Non-Foster impedance matching networks for small antennas has been attempted [99], [100]. With conventional passive matching networks, the antennas can be matched over only narrow frequency bands. However, Non-Foster matching networks composed of negative capacitors and/or inductors can in principle match the antenna over wide frequency bands because Non-Foster matching networks can overcome the gain-bandwidth restrictions derived by Bode-Fano. While the use of the networks at commercial high frequencies is still problematic due to stability issue, this approach can provide better opportunities to

bandwidth enhancement of small antennas operating at lower frequencies such as HF band. Fig. 6.2 shows the extremely short monopole antenna connected in series with a negative capacitor.
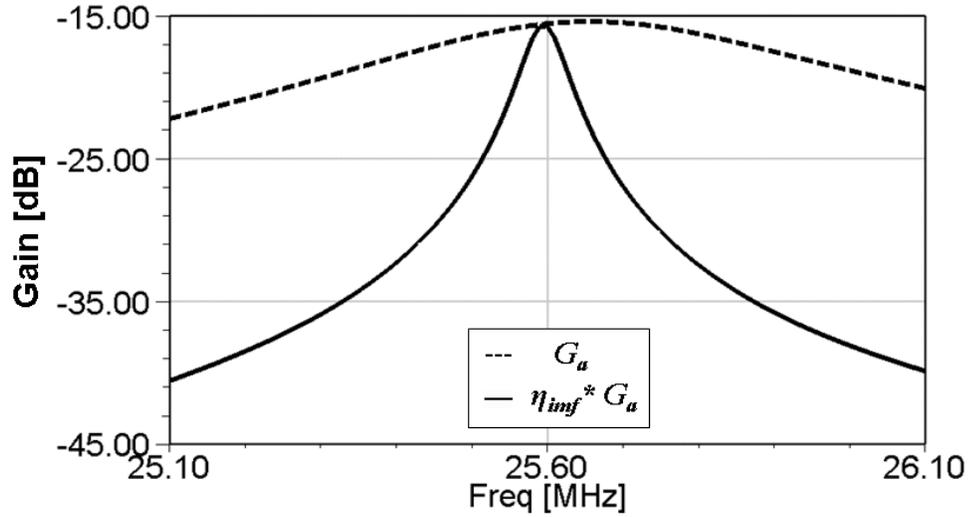
Figure 6.1: Antenna gain with and without considering impedance mismatch factor to a feed (η_{imf}).
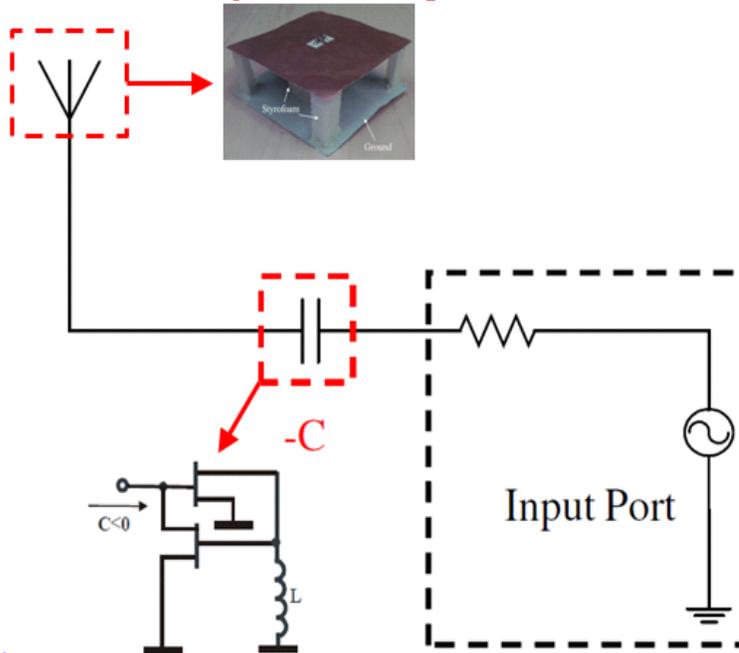
Figure 6.2: Extremely short monopole antenna connected in series with a negative capacitor.

6.2.2 Further Size Reduction and Bandwidth Enhancement of Miniaturized CP Antenna Using Reactive Impedance Surface (RIS)

In Chapter 4, for CP patch antennas, a new approach achieving a size reduction of as high as 75%, compared to a conventional corner-truncated circularly polarized patch antenna is presented while the level of size reduction of the conventional approaches is limited to about 50%. It would be interesting to combine the proposed highly miniaturized CP patch antenna with a reactive impedance surface (RIS). It is reported that the RIS can be used to improve antenna bandwidth and size reduction [101], [102]. Therefore, the investigation of the effects of the RIS on the proposed CP antenna may achieve additional size reduction and enhancement in impedance and axial ratio bandwidth. Fig 6.3 describes the proposed miniaturized CP patch antenna further reduced by being mounted on the RIS.
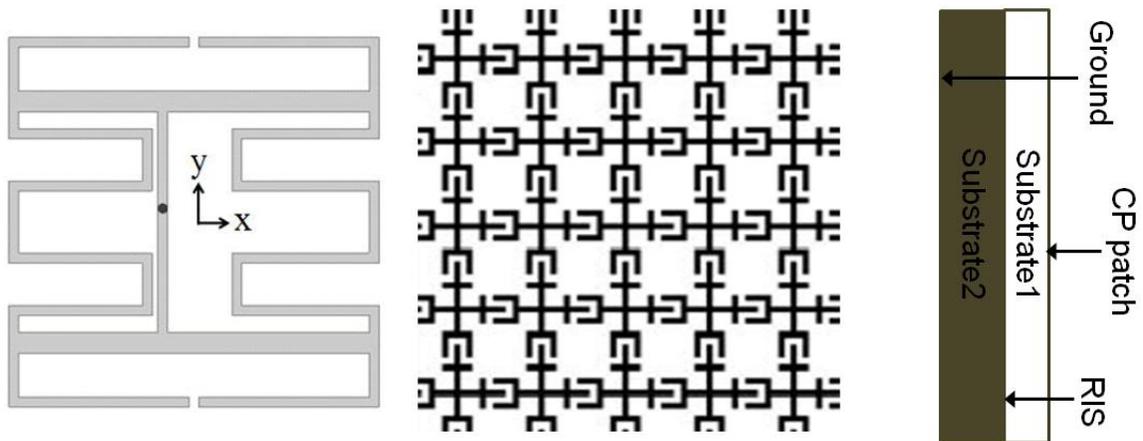
Figure 6.3: Proposed miniaturized CP patch antenna further reduced by being mounted on the RIS.

6.2.3 Compact Co-Located Three-Element Diversity Antennas

In Chapter 5, the design of compact co-located polarization and pattern diversity antennas using a new class of microstrip antennas is discussed. While the proposed diversity antennas are based on two antenna elements, the utilization of the proposed microstrip antenna topology can be extended to design compact co-located three-element diversity antennas. The basic idea is to combine the two proposed polarization and pattern diversity antennas in a new topology with the novel use of an additional feed. This approach employs the fact that the proposed microstrip antenna topology can provide two different radiation modes: 1. PIFA and 2. Patch mode. Since the two modes are degenerate (see Fig. 6.4 and 6.5), adding port2 to the other side of the inverted L element connected with port1 and tuning the antenna topology can make the two degenerate modes operate at a single frequency. Since TM_{11} and TM_{01} excited by port1 and 2 support broadside and omnidirectional radiation patterns, respectively, pattern diversity can be achieved only using a single proposed microstrip antenna. Next, similarly to the topology of the proposed polarization diversity antenna, inserting another bow-tie microstrip antenna connected with port1 into the open area in the pattern diversity antenna achieves compact co-located 3-element antenna diversity without increasing the area of the previous proposed diversity antennas. Fig. 6.5(a) shows expected topology of the 3-element diversity antenna. Also, Fig. 6.5(b) describes the expected S_{11}, S_{22} and S_{33} corresponding to port1, 2 and 3 in Fig. 6.5(a). Research about novel feed structures to lower the isolations among the three ports is being conducted. Instead of utilizing the vertical metallic plates as feeding elements, it is anticipated that realizing aperture or proximity coupled feed structure can enhance the isolations.
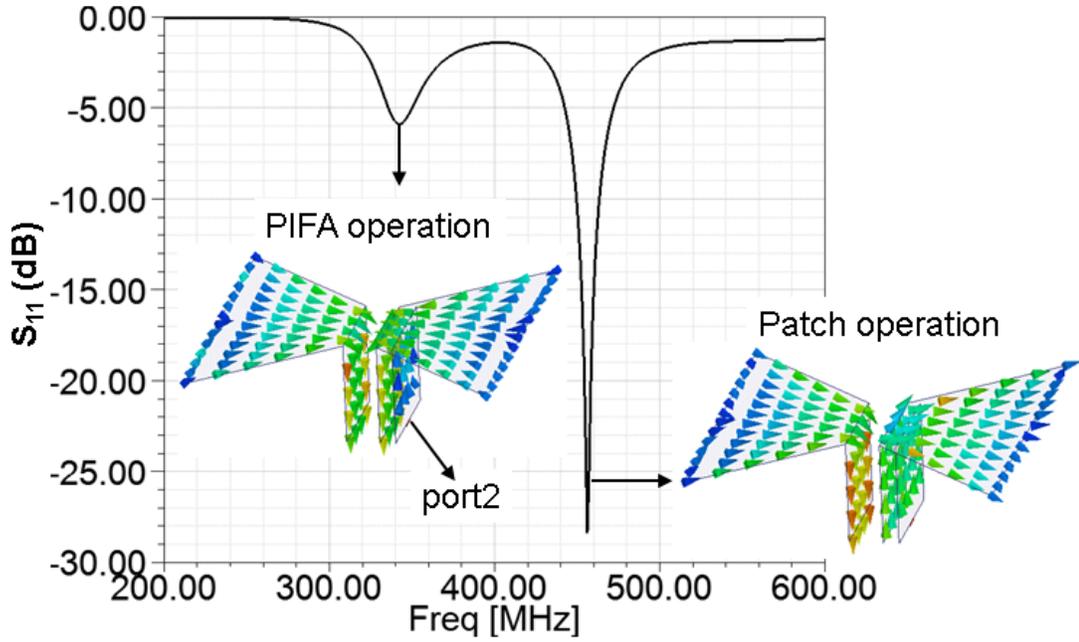
Figure 6.4: S_{11} and electric surface current distributions at two modes of the proposed microstrip antenna.

(a)   (b)
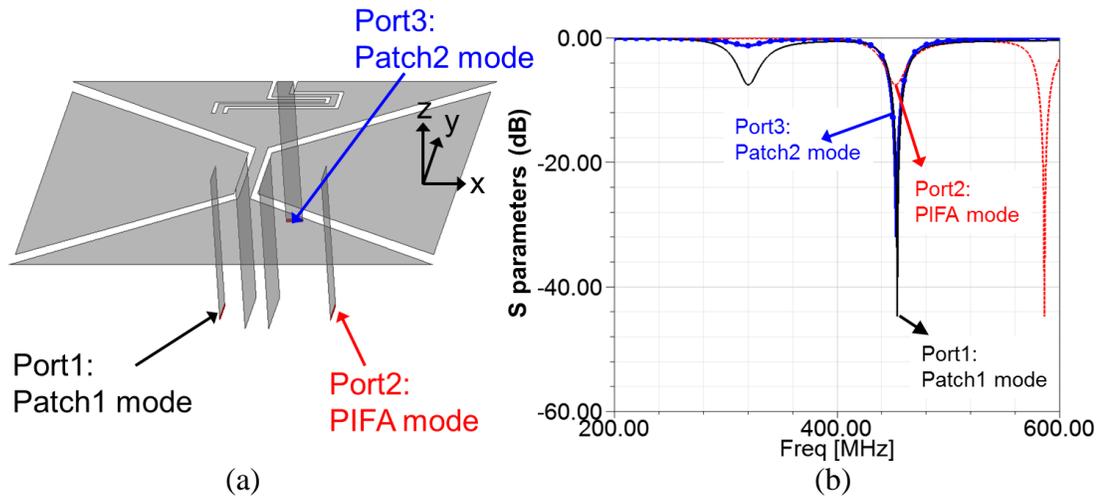
Figure 6.5: Expected (a) topology of the 3-element diversity antenna and (b) S_{11}, S_{22} and S_{33}.

APPENDICES

Appendix A

Pattern Diversity Antenna System

Pattern diversity can be achieved when radiation patterns of two diversity antennas are compared. When using two different collocated antennas with different radiation patterns, in a highly multi-path environment the signals arriving at the antenna terminals are collected from different directions and are expected to be uncorrelated.
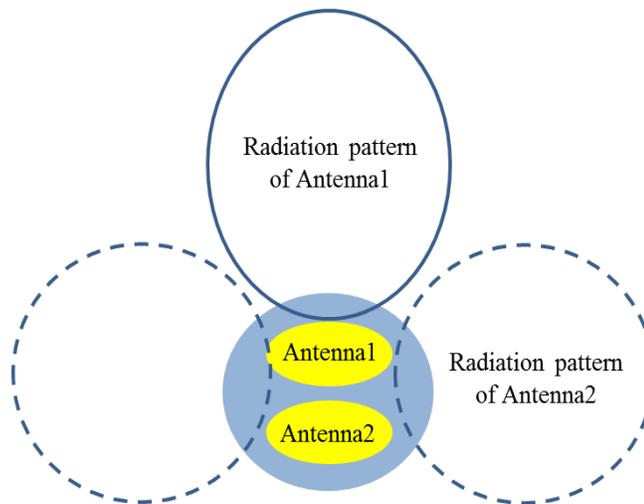
Figure A.1: Radiation pattern diversities using two antennas.

In this study, the antenna system consists of two antennas with two different radiation patterns: one antenna with omnidirectional radiation pattern in horizontal plane and the other one with a radiation pattern mainly in the broadside direction, as shown Fig. A.1. Fig. A.2 describes wave propagations of the fields radiated from such antennas in indoor environments. When this system is used in indoor environments and near ground, the signal transmitted from the antenna with broadside radiation pattern propagates bouncing between top ceilings and ground, which corresponds to a flesh-colored ray in Fig. A.2. On the other hand, the signal from the omnidirectional antenna propagates as a

surface wave near ground, as depicted as a green ray in Fig. A.2. These two totally different wave propagation mechanisms result in the decrease in correlation between the two signal received by the radiation diversity antennas, leading to increased channel capacity. For example, if the two rays are ideally uncorrelated, when one antenna at the receiver receives peak-value power, the other may be at a null signal position.
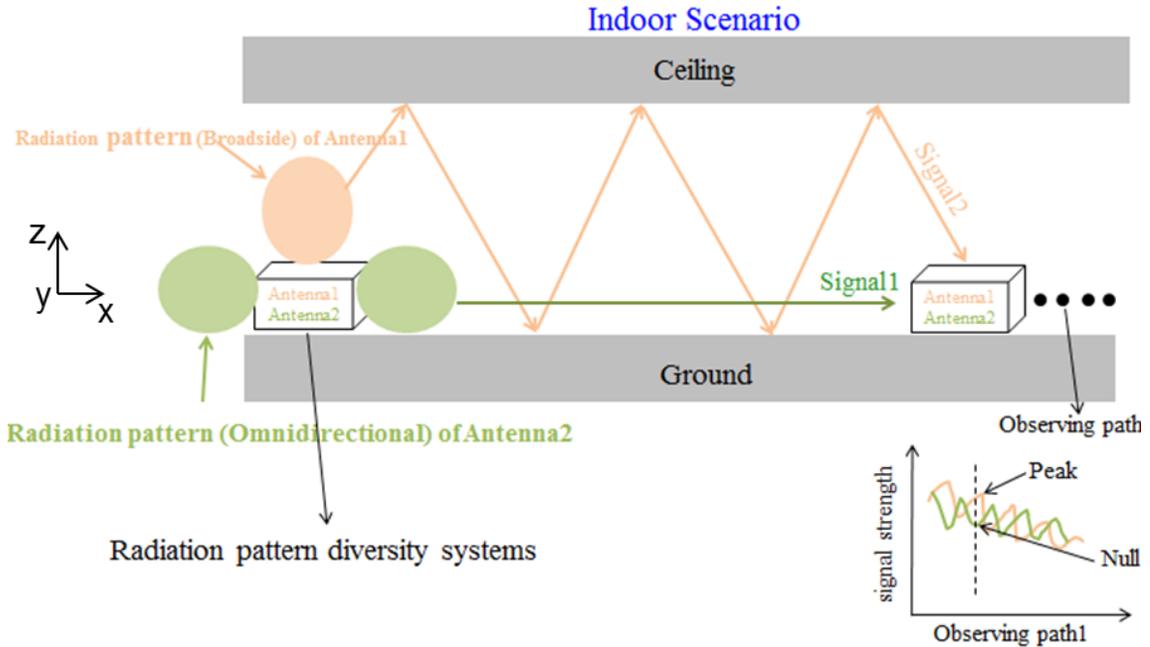
Figure A.2: Indoor scenario utilizing radiation pattern diversity antenna system.

- Design of Collocated Bow-tie Patch and λ/4 Monopole Antennas for Co-Polarized Radiation Pattern Diversity

In order to utilize the aforementioned diversity technique, a new co-polarized radiation pattern diversity antenna is designed, as shown in Fig. A.3. As an antenna with omni-directional radiation pattern, a λ/4 monopole antenna is used. As other antenna with broadside radiation pattern, a bowtie patch antenna, a miniaturized version of a λ/2 microstrip antenna, is used. In order to design the two antennas collocated in small space, the monopole antenna can be placed at the center of the bow-tie patch antenna because

the electric field is zero at the center. This results in low correlation between two different radiation patterns from the antennas. In addition, considering the difficulty of impedance matching to a feed cable due to the finite size of the ground plane in this design, the concept of the sleeve, which is a well-known technique for improving bandwidth and obtaining impedance matching, is applied. In this geometry, a short section (h_2 in Fig. A.4) of the coaxial cable protruding over the bowtie patch antenna, acts as an impedance transformer. In this study, the bow-tie patch antenna is designed on the air substrate. Since the geometry of the bowtie patch antenna is symmetric in terms of XZ and YZ planes, omnidirectional radiation pattern is obtained. Through parametric study using a full-wave simulator, Ansoft HFSS 13.0, two operating frequencies of the two antennas are merged to be same.

(a)   (b)   (c)
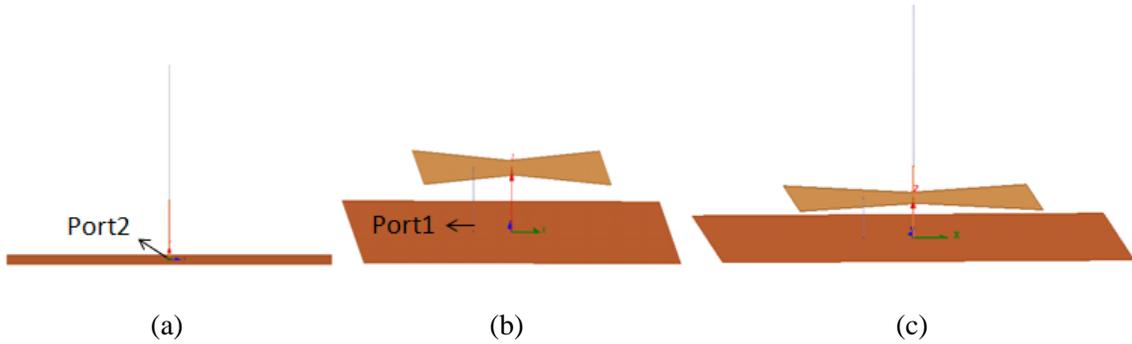
Figure A.3: (a) Quarter-wave monopole antenna, (b) bow-tie patch antenna, and (c) proposed radiation pattern diversity antenna.
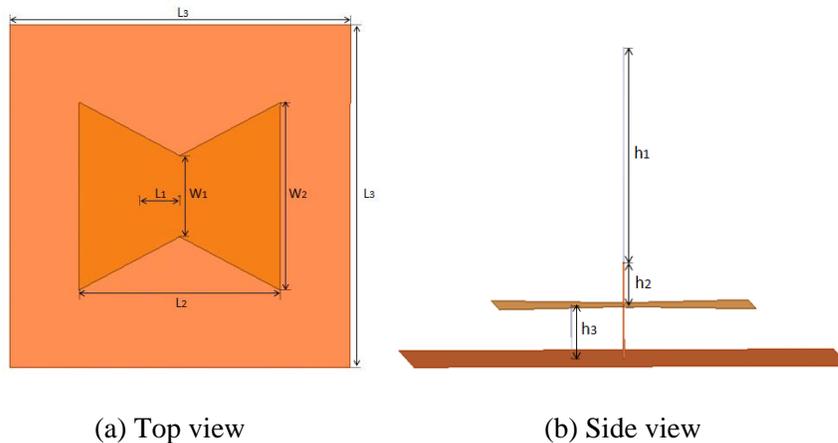
(a) Top view   (b) Side view

Figure A.4: Design parameters of the proposed radiation pattern diversity antenna.

Design parameters are shown in Fig. A.4. The values are given by $L_1 = 55$ mm, $L_2 = 272$ mm, $L_3 = 460$ mm, $W_1 = 105$ mm, $W_2 = 250$ mm, $h_1 = 155.5$ mm, $h_2 = 31.5$ mm, and $h_3 = 40$ mm. In order to consider ohmic loss, conductivity of copper is used in all metallic traces in the full-wave analysis. Fig. A.5 shows the simulated S-parameters of the antennas. Phase and amplitude information of the S-parameter are used to calculate the envelop correlation ($=\rho_e$) between the two different radiation patterns. The value of the calculated correlation is as low as 0.00016 or -37.94 dB at 395MHz. Fig. A.6 shows 3D radiation patterns of the proposed antenna at 395MHz. To derive the radiation patterns, when one antenna is fed (ON), other antenna is terminated to 50Ω. Based on the simulated design parameters, the pattern diversity antenna is fabricated and measured, as shown in Fig. A.7. As can be seen in Fig. A.8, the measured result shows a good agreement with the simulated result, and from the measured data, the value of the correlation is found to be as low as 0.0013 or -28.97 dB at 400MHz. The slight difference between simulated and measured correlation values is due to the addition of a coaxial cable into the air substrate to feed the bow-tie patch antenna, leading to the slight increase in the interaction between two feeds.
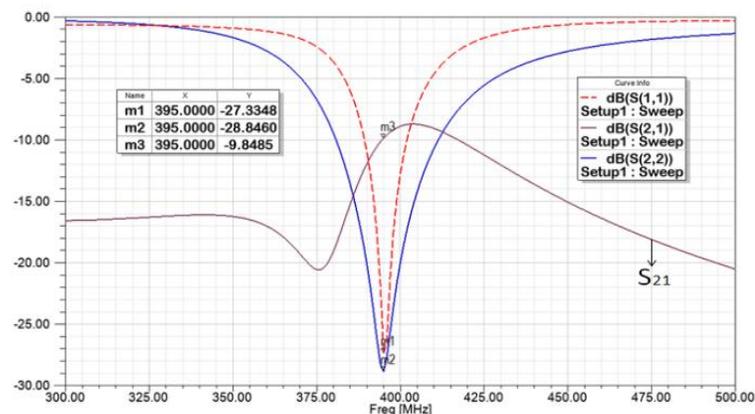
Figure A.5: Simulated S parameters of the proposed radiation pattern diversity antenna.
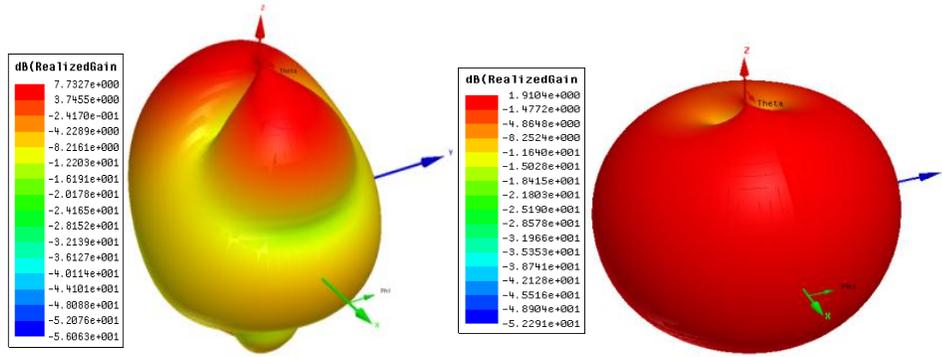
(a)   (b)

Figure A.6: 3D radiation patterns (E_θ) of the proposed radiation pattern diversity antenna: (a) when the bowtie patch antenna is 'ON' and the $\lambda/4$ monopole antenna is 'OFF' (broadside radiation pattern), and (b) when the bowtie patch antenna is 'OFF' and the $\lambda/4$ monopole antenna is 'ON' (omnidirectional radiation pattern).
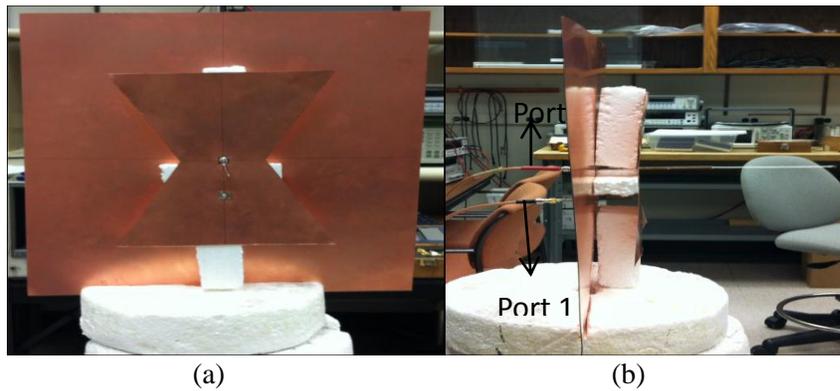
(a)   (b)

Figure A.7: (a) Top view and (b) side view of the fabricated pattern diversity antenna.
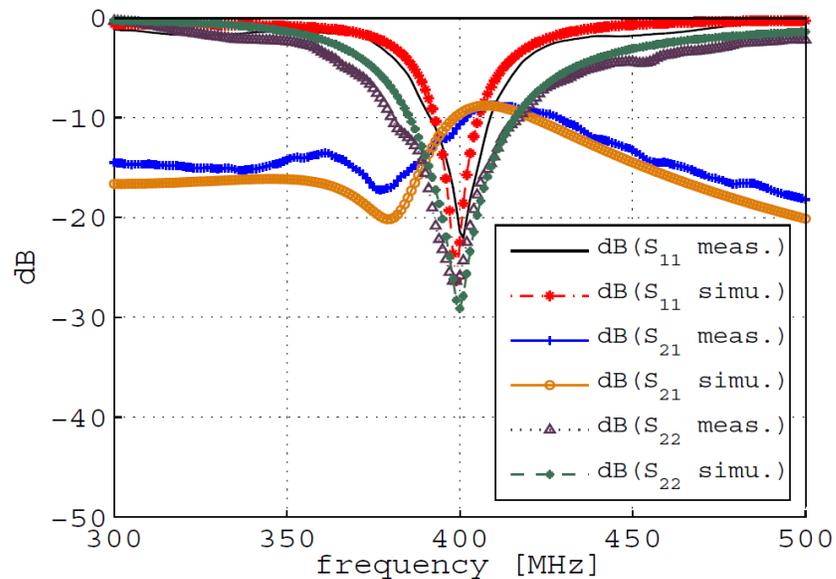
Figure A.8: Simulated and measured S parameters of the proposed pattern diversity antenna

- System Configuration

In order to investigate indoor wave propagation of radiated fields from the proposed diversity antennas, a measurement system is implemented at 400MHz. The operating frequency of 400MHz is chosen considering the allowable size of the antenna and characteristics of indoor wave propagation as a function of the operating frequency. Fig. A.9 shows schematics of a transmitter and receiver utilizing the proposed diversity antennas. When one transmitting antenna is connected to a signal generator (ON), other antenna is terminated to 50Ω (OFF). Received signals at both receiving antennas are recorded. In other words, while only one transmitting channel is 'ON', signals at both intended and unintended receiving channels are recorded. By calculating the correlation between the two signals received from two different antennas, the ability of the proposed diversity system to increase channel capacity is verified. In the receiver, the received 400MHz signals are down converted to 20MHz and the signals are sampled by a highly sensitive 16-bit A/D converter whose maximum available sampling rate is 80Mbps. With this receiver set up, the received data can be easily compared to each other and processed to calculate the correlation. Bandpass filters (BPF) are used to get rid of outer noise signals. Also low noise amplifiers (LNA) and IF amplifiers are used to satisfy the detectable sensitivity of the A/D Converters. Fig. A.10 and A.11 shows the pictures of the fabricated antennas and receiving module. In order to realize a channel established by near-ground wave propagation, the diversity antennas are positioned near the ground, about 10cm (=$0.13\lambda_0$ at 400MHz) above the ground, as shown Fig. A.11.

(a)   (b)
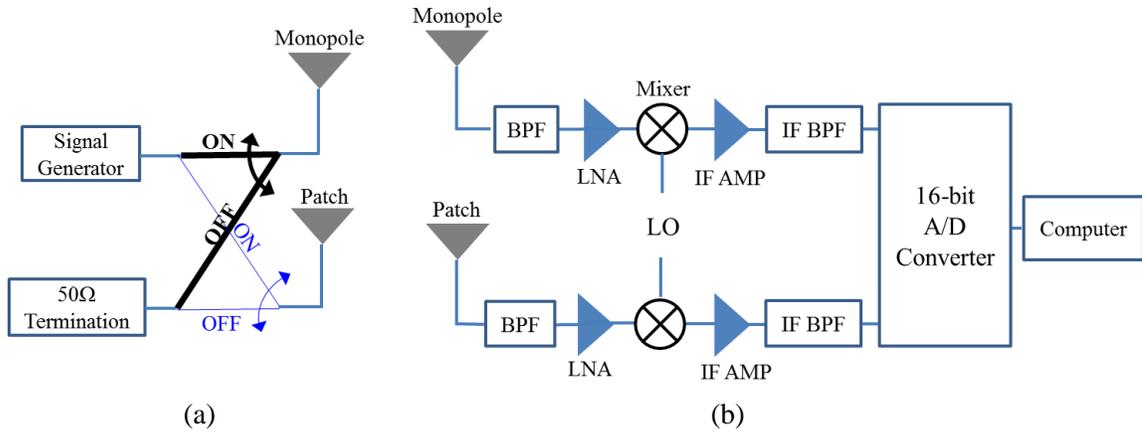
Figure A.9: Schematics of (a) the transmitter and (b) receiver utilizing the proposed diversity antennas.

(a)   (b)
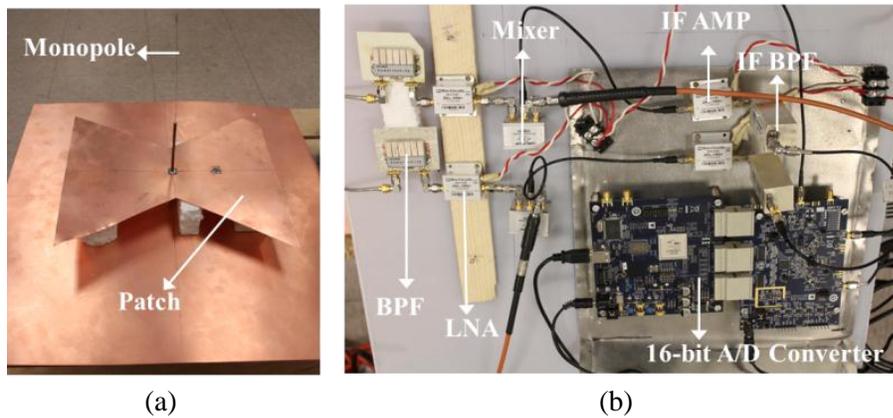
Figure A.10: (a) Fabricated diversity antennas and (b) receiving module.
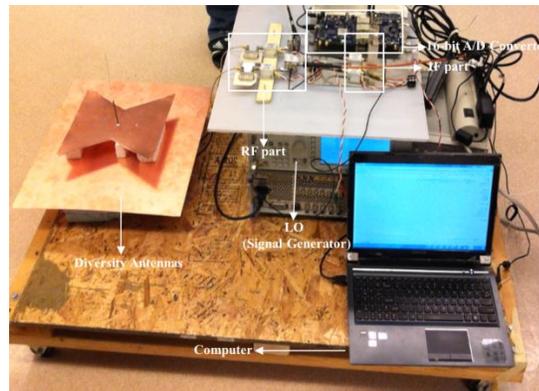
Figure A.11: Receiving system including diversity antennas and a computer.

- Measurement in Multipath-Rich Indoor Scenario

Using the measurement system discussed in the previous section, the propagation measurements are performed in a complex multi-path-rich indoor environment. Fig. A.12

128

shows the chosen measurement set up on 3rd floor in EECS building in the University of

Michigan. The measurement environment consists of a bunch of concrete walls and

wood/metallic objects. While the position of the receiver system is fixed, the transmitter

moves at intervals of 10cm along the path shown in Fig. A.12 and every step the

variations of output signals at two receiving channels are recorded. Considering the two

received signals as random variables (X and Y) in terms of the position of the transmitter,

the envelop correlation ($\rho_{envelop}$) between the two random variables can be calculated

using equation (A.1).

$$\rho_{envelop} = \frac{E[(X - E(X))(Y - E(Y))]}{\sqrt{E(X^2) - (E(X))^2}\sqrt{E(Y^2) - (E(Y))^2}} \qquad (A.1)$$

where *X* and *Y* are output signals at the two receiving channels, a function of the position
of the transmitter
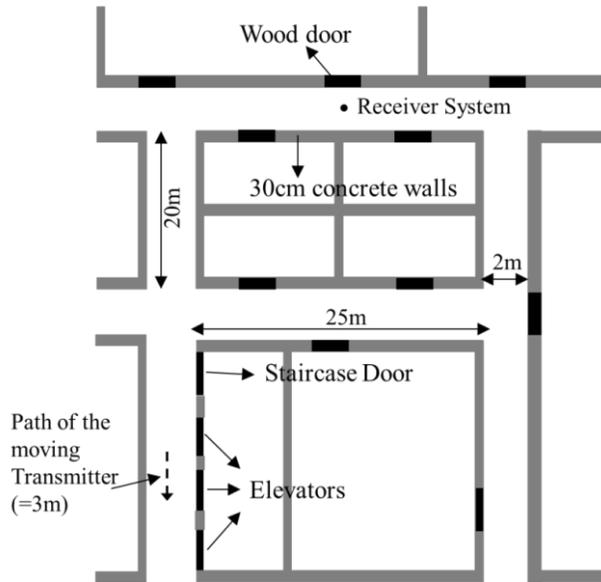
Figure A.12: Measurement set up on 3rd floor in EECS building in the University of Michigan.

Fig. A.13(a) shows the two output signals from the two receiving antennas when

monopole antenna is 'ON' (connected to a signal generator) and patch antenna is 'OFF'

(connected to a 50Ω termination), denoted by 'case1'. On the contrary to this, plots in Fig. A.13(b) correspond to the case that monopole antenna is 'OFF' and patch antennas is 'ON', denoted by 'case2'. It is observed that in the case1 where near-ground wave propagation is excited by monopole antenna with omni-directional radiation pattern, the fields radiated by the monopole antenna are well received at both receiving antennas. This is because the use of a finite ground plane makes the radiation pattern of the patch antenna broader, eliminating a desired radiation null at θ=90°. On the other hand, in the case2 where the propagation rays bouncing between top ceilings and ground are dominantly excited by patch antenna, the monopole antenna have a relatively poor signal reception at θ=0°, while the patch antenna well receives the transmitted signal. This is why the envelop correlation in case2 is much lower than the envelop correlation in case1. The envelop correlations derived by case1 and case2 are   0.3985   and   0.0953.   They both are less than 0.5, which is a maximum limit for diversity systems. Measurements results validate the feasibility of using the proposed diversity system in multipath-rich indoor environments.

(a)   (b)
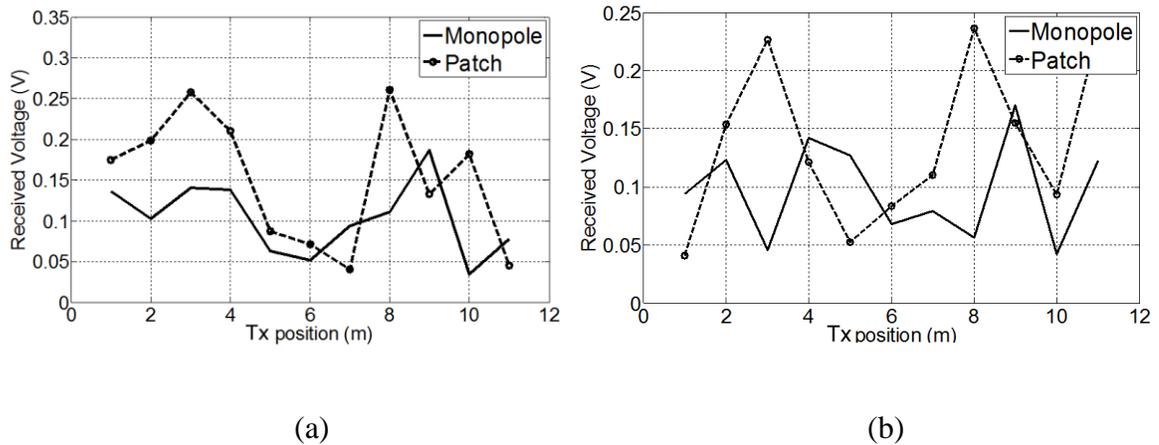
Figure A.13: Two output signals from the two receiving antennas (a) when monopole antenna is 'ON' and patch antenna is 'OFF' and (b) when monopole antenna is 'OFF' and patch antenna is 'ON'.

BIBLIOGRAPHY

[1] G.Weinberger, "The new millennium: Wireless technologies for a truly mobile society," in *Int. Solid-State Circuits Conf. Tech. Dig.*, Feb. 2000, pp. 20–24.

[2] R. Harrison, "A Software-Defined Platform for Current and Future Communications Systems," *Instrumentation Newsletter*, Q1 2006.

[3] Maxim, "Tracking Advances in VCO Technology," *APPLICATION NOTE 1768*, Dec. 2002.

[4] *http://www.antenna-theory.com*

[5] W. Hong and K. Sarabandi, "Design of low-profile omnidirectional antenna for ground sensor networks," in *Proc. IEEE Antennas Propag. Soc. Int. Symp.*, Jun. 2007, pp. 6007–6010.

[6] A. Alomainy, Y. Hao, and F. Pasveer, "Numerical and experimental evaluation of a compact sensor antenna for healthcare devices," Biomedical Circuits and Systems, *IEEE Transactions on*, vol. 1, no. 4, pp. 242–249, Dec. 2007.

[7] E. A. Johannessen, L. Wang, C. Wyse, D. R. S. Cumming, and J. M. Cooper, "Biocompatibility of a lab-on-a-pill sensor in artificial gastrointestinal environments," *IEEE Trans. Biomed. Eng.*, vol. 53, no. 11, pp. 2333–2340, Nov. 2006.

[8] D. Liao and K. Sarabandi, "Terminal-to-terminal hybrid full-wave simulation of low-profile, electrically-small, near-ground antennas," *IEEE Trans. Antennas Propag.*, vol. 56, no. 3, pp. 806–814, Mar. 2008.

[9] D. Liao and K. Sarabandi, "Optimization of low-profile antennas for applications in unattended ground sensor networks," *IEEE Trans. Antennas Propag.*, vol. 53, no. 11, pp. 3747–3756, Nov. 2005.

[10] Sarabandi, K., and M. Casciato, "Efficient Calculation of the Fields of a Dipole Radiating Above an Impedance Surface," *IEEE Transactions on Antennas and Propagation*, vol. 50, no. 9, pp. 1222-1235, September 2002.

[11] B. Y. Toh, R. Cahill, and V. F. Fusco, "Understanding and measuring circular polarization," *IEEE Trans. Education*, vol. 46, pp. 313, Aug. 2003.

[12] G. J. Foschini and M. J. Gans, "On limits of wireless communications in a fading environment when using multiple antennas," *Wireless Pers. Commun.*, vol. 6, pp.311-33S, 1998.

[13] R. G. Vaughan and J. B. Andersen, "Antenna diversity in mobile communications," *IEEE Trans. Veh. Technol.*, vol. VT-36, no. 4, pp. 147–172, Nov. 1987.

[14] P. Mattheijssen, M. Herben, G. Dolmans, and L. Leyten, "Antenna pattern diversity versus space diversity for use at handhelds," *IEEE Trans. Veh. Technol.*, vol. 53, no. 4, pp. 1035–1042, Jul. 2004.

[15] T. Taga and K. Tsunoda, "Analysis of a planar inverted-F antenna by spatial network method," *IEICE*, B-2, vol. J74-B-2, no. 10, pp. 538–545, Oct. 1991.

[16] S. Sekine, T. Ito, N. Odachi, Y. Murakami, and H. Shoki, "Design method for a broadband inverted-F antenna by parallel resonance mode," *IEICE*, B, vol. J86-B, no. 9, pp. 1806–1815, Sep. 2003.

[17] J. Oh and K. Sarabandi, "Low Profile, Miniaturized, Inductively Coupled Capacitively Loaded Monopole Antenna," *IEEE Transactions on Antennas and Propagation*, vol. 60, no. 3, pp. 1206–1213, Mar. 2012.

[18] J. McLean, H. Foltz, and G. Crook, "Broadband, robust, low profile monopole incorporating top loading, dielectric loading, and a distributed capacitive feed mechanism," in *Proc. IEEE Int. Symp. Antennas Propag.*, Jul. 11–16, 1999, vol. 3, pp. 1562–1565.

[19]   S. Tokumaru, "Multiplates: Low profile antennas," in *IEEE Int. Symp. Antennas Propag.*, Oct. 1976, vol. 14, pp. 379–382.

[20]   N. Herscovivi and E. Dziadek, "Omnidirectional antennas for wireless communication," in *Proc. IEEE Int. Symp. Antennas Propag.*, Jul. 11–16, 1999, vol. 1, pp. 556–559.

[21]   T. Noro and Y. Kazama, "Low profile and wide bandwidth characteristics of top loaded monopole antenna with shorting post," in *Proc. IEEE Int. Workshop on Antenna Technol. Small Antennas and Novel Metamater.*, Mar. 6–8, 2006, pp. 108–111.

[22]   C. Delaveaud, P. Levegue, and B. Jecko, "Small-sized low-profile antenna to replace monopole antennas," *Electron. Lett.*, vol. 34, pp. 716–717, Apr. 1998.

[23]   G. Goubau, "Multielement monopole antennas," in *Proc. Workshop on Electrically Small Antennas ECOM*, Ft., Monmouth, NJ, May 1976, pp. 63–67.

[24]   H. Iwasaki, "A circularly polarized small-size microstrip antenna with a cross slot," *IEEE Trans. Antennas and Propag.*, vol. 44, pp. 1399-1401, Oct. 1996.

[25]   W.S. Chen, C. K. Wu, and K. L. Wong, "Compact circularly polarized microstrip antenna with bent slots," *Electron. Lett.*, vol. 34, pp. 1278-1279, Jun. 25, 1998.

[26]   Jensen, M.A. and Rahmat-Samii, Y. "Performance analysis of antennas for hand-held transceivers using FDTD" *IEEE Trans. on Antennas and Propagation*, vol. 42, issue 8, pp. 1106 - 1113, Aug. 1994.

[27]   C. R. Rowell and R. D. Murch, "A compact PIFA suitable for dual frequency 900/1800 MHz operation," *IEEE Trans. Antennas Propagat.*, vol. 46, pp. 596–598, Apr. 1998.

[28]   M. G. Douglas, M. Okoniewski, and M. A. Stuchly, "A planar diversity antenna for hand-held PCS devices," *IEEE Trans. Veh. Technol.*, vol. 47, pp. 747–754, Aug. 1998.

[29]   Jungsuek Oh, and Kamal Sarabandi, "A Topology-Based Miniaturization of Circularly Polarized Patch Antenna," *IEEE Transactions on Antennas and Propagation*, submitted for publication (October 2011).

[30]   Jungsuek Oh, Michael Thiel, and Kamal Sarabandi, "Wave Propagation Management in Indoor Environments Using Micro-Radio Repeater Systems," *IEEE Antennas and Propagation Magazine*, accepted for publication.

[31]   Fikadu T Dagefu, Jungsuek Oh, and Kamal Sarabandi, "A Sub-wavelength RF Source Tracking System for GPS-denied Environments," *IEEE Transactions on Antennas and Propagation*, submitted for publication (March 2012).

[32]   Jungsuek Oh, Jihun Choi, Fikadu T Dagefu, and Kamal Sarabandi, "Extremely Small Two-Element Monopole Antenna for HF Band Applications," *IEEE Transactions on Antennas and Propagation*, accepted for publication.

[33]   Jungsuek Oh and Kamal Sarabandi, "Low Profile Vertically Polarized Omnidirectional Wideband Antenna with Capacitively Coupled Parasitic Elements," *IEEE Transactions on Antennas and Propagation*, submitted for publication (Aug 2012).

[34]   Jungsuek Oh and Kamal Sarabandi, "Compact Co-Located Polarization/Pattern Diversity Antennas Using a New Class of Microstrip Antennas," *IEEE Transactions on Antennas and Propagation*, in preparation.

[35]   Fikadu T Dagefu, Jungsuek Oh, Jihun Choi and Kamal Sarabandi, "Measurements and Physics-based Analysis of Co-located Antenna Pattern Diversity System," *IEEE Transactions on Antennas and Propagation*, in preparation.

[36]   Jungsuek Oh, Kyusang Lee, Kamal Sarabandi and Stephen R. Forrest, "Structurally Embedded Antennas in Thin-Film Solar Cells," *Applied Physics Letters*, in preparation.

[37] W. B. Hong and K. Sarabandi, "Low-profile, multi-element, miniaturized monopole antenna," *IEEE Trans. Antennas Propag.*, vol. 57, no. 1, pp. 72-80, Jan. 2009.

[38] N. Behdad and K. Sarabandi, "Bandwidth enhancement and further size reduction of a class of miniaturized slot antennas," *IEEE Trans. Antennas Propag.*, vol. 52, pp. 1928–1935, Jan. 2004.

[39] W. Hong, N. Behdad, and K. Sarabandi, "Size reduction of cavity backed slot antennas," *IEEE Trans. Antennas Propag.*, vol. 54, pp. 1461–1466, 2006.

[40] C. R. Rowell and R. D. Murch, "A capacitively loaded PIFA for compact mobile telephone handsets," *IEEE Trans. Antennas Propag.*, vol. 45, pp. 837–842, May 1997.

[41] R. L. Li, G. DeJean, M. M. Tentzeris, and J. Laskar, "Development and analysis of a folded shorted-patch antenna with reduced size," *IEEE Trans. Antennas Propag.*, vol. 52, pp. 555–562, Feb. 2004.

[42] C. Y. Chiu, K. M. Shum, and C. H. Chan, "A tunable via-patch loaded PIFA with size reduction," *IEEE Trans. Antennas Propag.*, vol. 55, no. 1, pp. 65–71, Jan. 2007.

[43] A. S. Meier and Summers, "Measured impedance of vertical antennas and effects of finite ground planes," *Proc. IEEE*, vol. 37, pp. 609–616, 1969.

[44] K. H. Awadalla and Maclean, "Input impedance of a monopole antenna at the center of a finite ground plane," *IEEE Trans. Antennas Propag.*, vol. AP-26, pp. 244–248, 1978.

[45] Weiner, "Monopole element at the center of a circular ground plane whose radius is small or comparable to a wavelength," *IEEE Trans. Antennas Propag.*, vol. AP-35, pp. 488–495, 1987.

[46]   Bhattacharyya, "Effects of ground plane and dielectric truncations on the efficiency of a printed structure," *IEEE Trans. Antennas Propag.*, vol. 39, pp. 303–308, 1991.

[47]   M. C. Huynh and W. Stutzman, "Ground plane effects on the planar inverted-F antenna (PIFA) performance," *IEE Proc. Microwave Antennas Propag.*, vol. 150, no. 4, pp. 209–213, Aug. 2003.

[48]   P. L. Werner, and D. H. Werner, "Design Synthesis of Miniature Multi-band Monopole Antennas with Application to Ground-based and Vehicular Communication Systems," *IEEE Antennas and Wireless Propagation Letters*, vol. 4, pp. 104-106, 2005.

[49]   J. Baker, H. S. Youn, N. Celik, and M. F. Iskander, "Low-profile multifrequency HF antenna design for coastal radar applications," *IEEE Antennas and Wireless Propagation Letters*, vol. 9, pp. 1119–1122, 2010.

[50]   P.L. Chi, R. Waterhouse, and T. Itoh, "Antenna miniaturization using slow wave enhancement factor from loaded transmission line models," *IEEE Transactions on Antennas and Propagation*, vol. 59, pp. 48-57, Jan. 2011.

[51]   F.T. Dagefu, J. Oh, and K. Sarabandi, "A Sub-wavelength RF Source Tracking System for GPS-denied Environments," submitted to *IEEE Transactions on Antennas and Propagation*.

[52]   Qi Luo, J. R. Pereira, and H.M. Salgado, "Compact Printed Monopole Antenna with Chip Inductor for WLAN," *IEEE Antennas and Wireless Propagation Letters*, vol. 10, pp. 880–883, 2011.

[53]   K. Wong and S. Chen, "Printed single-strip monopole using a chip inductor for penta-band WWAN operation in the mobile phone," *IEEE Transactions on Antennas and Propagation*, vol. 58, no. 3, pp. 1011–1014, Mar. 2010.

[54] T. Kang and K. Wong, "Chip-inductor-embedded small-size printed strip monopole for WWAN operation in the mobile phone," *Microwave and Optical Technology Letter*, vol. 51, no. 4, pp. 996–971, Apr. 2009.

[55] J. Oh and K. Sarabandi, "A low-profile omnidirectional planar antenna with vertical polarization employing two in-phase elements," in *Proc. General Assembly and Scientific Symposium*, 2011 XXXth URSI, Aug. 13–20, 2011, pp. 1–4.

[56] http://www.coilcraft.com/

[57] Y.-J. Kim and M. G. Allen, "Surface micromachined solenoid inductors for high frequency applications," *IEEE Trans. Comp. Packag. Manufact. Technol.*, vol. 21, pp. 26–33, Jan. 1998.

[58] C. R. Sullivan, L. Weidong, S. Prabhakaran, and L. Shanshan, "Design and fabrication of low-loss toroidal air-core inductors," in *Proc. Power Electron. Spec. Conf. 2007*, pp. 1754–1759.

[59] S. C. Tang, S. Y. R. Hui, and H. Chung, "Coreless planar printed-circuitboard (PCB) transformers—A fundamental concept for   signal and energy transfer," *IEEE Trans. Power Electron.*, vol. 15, no. 5, pp. 931–941, Sep. 2000.

[60] S. Y. R. Hui, S. C. Tang, and H. Chung, "Some electromagnetic aspects of coreless PCB transformers," *IEEE Trans. Power Electron.*, vol. 15, no. 4, pp. 805–810, Jul. 2000.

[61] S. C. Tang, S. Y. R. Hui, and H. Chung, "Characterization of coreless printed circuit board (PCB) transformers," *IEEE Trans. Power Electron.*, vol. 15, no. 6, pp. 1275–1282, Nov. 2000.

[62] P. Dowell, "Effects of eddy currents in transformer windings," *IEE Proc.*, vol. 113, pp. 1387-1394, Aug. 1966.

[63]   Corum K. L. and Corum J. F., "RF coils, helical resonators and voltage magnification by coherent spatial modes," *Microwave Review*, IEEE, vol. 7, no. 2, pp. 36-45, Sep. 2001.

[64]   Knight David W., G3YNH, "Inductors and transformers," From Transmitter to Antenna, *http://www.g3ynh.info/zdocs/magnetics/ part_1.html*

[65]   Medhurst R. G., "H.F. resistance and self-capacitance of single-layer solenoids," *Wireless Engineer*, pp. 35-43, Feb. 1947 & pp. 80-92, Mar. 1947.

[66]   L. J. Chu, "Physical limitations on omni-directional antennas," *J. Appl. Phys.*, vol. 19, pp. 1163-1175, Dec. 1948.

[67]   F. R. Hsiao and K. L.Wong, "Omnidirectional planar folded dipole antenna," *IEEE Trans. Antennas Propag.*, vol. 52, no. 7, pp. 1898–1902, Jul. 2004.

[68]   S. Palud, F. Colombel, M. Himdi, and C. Le Meins, "Wideband omnidirectional and compact antenna for VHF/UHF band," *IEEE Antennas Wireless Propag. Lett.*, vol. 10, pp. 3–6, 2011.

[69]   P.C. Bybi, G. Augustin, B. Jitha, C.K. Anandan, K. Vasudevan, and P. Mohanan, "A quasi-omnidirectional antenna for modern wireless communication gadgets," *IEEE Antennas Wireless Propag Lett.*, 7 (2008), 505–508.

[70]   K. L. Wong, S. W. Su, and C. L. Tang, "Broadband omnidirectional metal-plate monopole antenna," *IEEE Trans. Antennas Propag.*, vol. 53, no. 1, pp. 581–583, Jan. 2005.

[71]   Xing Chen, Kama Huang, and Xiao-Bang Xu "A novel planar slot array antenna with omni directional pattern," *IEEE Trans on Antennas and Propagation*, Vo. 59, No. 12, December 2011 ,pp4853-4857

[72]   H. Nakano, R. Suzuki, and J. Yamauchi, "Low-profile inverted-f antenna with parasitic elements on an infinite ground plane," *IEE Proc. Microw. Antennas Propag.*, vol. 145, no. 4, pp. 321–325, Aug. 1998.

[73]   K. Oh and K. Hirasawa, "A Dual-band inverted-L-folded-antenna with a parasitic wire," in *Proc. IEEE Antennas Propag. Int. Symp.*, Monterey, Jun. 2004, pp. 3131–3134.

[74]   Z. Jianwu, Z. Yangyang, and G. Feng, "A Novel Folded Inverted-F Antenna with Parasitic Stub for TD-SCDMA Systems," in *Proc. IEEE International Workshop on Antenna Technology*, 2009, pp. 1-4.

[75]   K. B. Kim, H. K. Ryu, and J. M. Woo, "Compact wideband folded monopole antenna coupled with parasitic inverted-L element for laptop computer applications," *IET Electron. Lett.*, vol. 47, no. 5, pp. 301–303, Mar. 2011.

[76]   M. Olmos, H. D. Hristov, and R. Feick, "Inverted-F antennas wideband match performance," *Electron. Lett.*, vol. 38, no. 16, pp. 845–847, Aug. 2002.

[77]   K. L. Wong and Y.F. Lin, "Circularly-polarised microstrip antenna with tuning stub," *Electron. Lett.*, vol. 34, No. 9, pp. 831-832, Apr. 30, 1998.

[78]   K. L. Wong and M.H. Chen, "Small slot-coupled circularly-polarised microstrip antenna with modified cross-slot and bent tuning-stub," *Electron. Lett.*, vol. 34, No. 16, pp. 1542-1543, Aug. 6, 1998.

[79]   D. M. Pozar and S. M. Duffy, "A dual-band circularly polarized aperture coupled stacked microstrip antenna for global positioning satellite," *IEEE Trans. Antennas and Propag.*, vol. 45, pp. 1618-1625, Nov. 1997.

[80]   W. S. Chen, C. K. Wu, and K. L. Wong, "Novel Compact Circularly Polarized Square Microstrip Antenna," *IEEE Trans. Antennas and Propag.*, vol. 49, pp. 340-342, Mar. 2001.

[81]   I. Nystrom and D. Karlsson, "Reduction of back radiation and cross-coupling in dual polarized aperture patch antennas," in *IEEE Antennas Propagat. Soc. Int. Symp. Dig.*, pp. 2222-2225, 1997.

[82]   T. Svantesson, "Correlation and channel capacity of MIMO systems employing multimode antennas," *IEEE Trans. Veh. Technol.*, vol. 51, no. 6, pp. 1304–1312, Nov. 2002.

[83]   P. S. Kildal and K. Rosengren, "Correlation and capacity of MIMO systems and mutual coupling, radiation efficiency, and diversity gain of their antennas: Simulations and measurements in a reverberation chamber," *IEEE Commun. Mag.*, vol. 42, no. 12, pp. 104–112, Dec. 2004.

[84]   I. J. Bahl and P. Bhartia, Microstrip Antennas. Norwood, MA: *Artech House*, 1980.

[85]   D. T. Notis, P. C. Liakou, and D. P. Chrissoulidis, "Dual polarized microstrip patch antenna, reduced in size by use of peripheral slits," in *Proc. Europ. Conf. on Wireless Technol.*, Amsterdam, 2004, pp. 125–128.

[86]   Gosalia, K., and Lazz, G. "Reduced size, dual polarized microstrip patch antenna for wireless communications," *IEEE Trans. Antennas Propag.*, vol. 51, no. 9, pp. 2182–2186, 2003.

[87]   Hu, S., J. Pang, and J. Qiu, "A compact polarization diversity MIMO microstrip patch antenna array with dual slant polarizations," *IEEE International Symposium on Antennas and Prop.*, 2009.

[88]   H. T. Chattha, Yi Huang, Stephen J.Boyes, and Xu Zhu "Polarization and Pattern Diversity-Based Dual-Feed Planar Inverted-F Antenna," *IEEE Trans. Antennas Propag.*, vol. 60, no. 3, pp. 1532–1539, Mar. 2012.

[89]   K. Wei, Z. Zhang, W. Chen, and Z. Feng, "A novel hybrid-fed patch antenna with pattern diversity," *IEEE Antennas Wireless Propag. Lett.*, vol. 9, pp. 562–565, 2010.

[90]   Zhang Z J, Li Y, Wei K P, et al. "Three designs of polarization diversity antenna for WLAN application," Proceedings of *2011 International Workshop on Antenna*

Technology (iWAT'11), Mar. 2011, Hong Kong, China. Piscataway, NJ, USA: IEEE, 2011.

[91]   S. Blanch, J. Romeu, and I. Cotbella, "Exact representation of antenna system diversity performance from input parameter description," *Electron. Lett.*, vol. 39, no. 9, pp. 705–707, May. 2003.

[92]   M. Sonkki, E. Antonino-Daviu, M. Ferrando-Bataller, and E. T. Salonen, "Planar wideband polarization diversity antenna for mobile terminals," *IEEE Antennas Wireless Propag. Lett.*, vol. 10, pp. 939–942, 2011.

[93]   P. Hallbjörner, "The significance of radiation efficiencies when using S-parameters to calculate the received signal correlation from two antennas," *IEEE AntennasWireless Propag. Lett.*, vol. 4, pp. 97–99, 2005.

[94]   M. Schwartz,W. R. Bennett, and S. Stein, *Communication Systems and Techniques*. New York: IEEE Press, 1996.

[95]   J. Oh and K. Sarabandi, "Low Profile Vertically Polarized Omnidirectional Wideband Antenna with Capacitively Coupled Parasitic Elements," submitted to *IEEE Transactions on Antennas and Propagation,* 2012.

[96]   H. Wong, K. L. Lau, and K. M. Luk, "Design of dual-polarized L-probe patch antenna arrays with high isolation," *IEEE Trans. Antennas Propag.*, vol. 52, no. 1, pp. 45–52, Jan. 2004.

[97]   S. Gao and A. Sambell, "Dual-polarized broad-band patch antennas fed by proximity coupling," *IEEE Trans. Antennas Propag.*, vol. 53, no. 1, pp. 526–531, Jan. 2005.

[98]   K. L. Wong and T. W. Chiou, "Broad-band dual-polarized patch antennas fed by capacitively coupled feed and slot-coupled feed," *IEEE Trans. Antennas Propag.*, vol. 50, no. 3, pp. 346–351, Mar. 2002.

[99] S. E. Sussman-Fort and R. M.Rudish, "Non-Foster impedance matching of a lossy, electrically-small antenna over an extended frequency range," *the Antenna Applicat. Symp.*, Allerton Park, IL, Sep. 18-20, 2007.

[100] ──, "Non-Foster Impedance Matching of Electrically-Small Antennas," *IEEE Trans. Antennas Propagat.*, vol.57, no.8, pp.2230-2241, Aug. 2009.

[101] H. Mosallaei and K. Sarabandi, "Antenna miniaturization and bandwidth enhancement using a reactive impedance substrate," *IEEE Trans. Antennas Propag.*, vol. 52, no. 9, pp. 2403–2414, Sep. 2004.

[102] K. Sarabandi, A. Buerkle, and H. Mosallaei, "Compact wideband UHF patch antenna on a reactive impedance substrate," *Antennas and Wireless Propagation Letters*, IEEE, vol. 5, no. 1, pp. 503–506, Dec. 2006.